



# **Developing a Reliability Model for an 88 kV XLPE Cable Termination**

**MSc Engineering**

*Author*

**Samantha Chimunda**

*Submitted to*

School of Electrical and Information Engineering, Faculty of Engineering and the Built  
Environment, University of the Witwatersrand, Johannesburg, South Africa

August 2019

## **Declaration**

I declare that this dissertation is my own unaided work. It is submitted for a Master of Science degree in Electrical Engineering to the University of the Witwatersrand, Johannesburg. It has not been submitted to any other university.

**Signature:**

## **Abstract**

Whereas there are life models for cable systems, the focus has been on cables and not on accessories. Literature shows that cable accessories are the problematic area in cable systems. There is therefore a need to develop cable accessory reliability models which can be used for informed asset management decision. This research work has conceived a reliability model for cable terminations using a case study municipal substation which has been experiencing failure of 88 kV XLPE power cable terminations. In the literature, there is an electrothermal model developed for cable systems. In the present work the existing model was adopted and extended. This study involved identifying the modes of degradation by forensic investigation of the failed terminations. For each mode of degradation, a corresponding mathematical model of the stress life factor was developed. Using the Weakest Link Principle, the product of reliabilities due to each degradation mechanism computes the overall reliability of the termination system. The results indicate that electrothermal stress hardly reduces the reliability of the termination from the time of installation to 40 years in service. However, thermomechanical stress causes a reliability of less than 10% after 18 years and galvanic degradation reduces the termination reliability to less than 10% after 24 years in service. Each new cable termination design should have a corresponding reliability model. The latter entails conducting laboratory aging tests which give the parameters required in developing the stress life factors. For existing terminations, root-cause analysis of failure can lead to determination of the stress factor parameters. The model developed in the present research work can be used in real-time asset management decisions by processing the real time operating conditions.

## **Acknowledgments**

The author would like to thank Professor Cuthbert Nyamupangedengu and Patrick O'Holloran for their guidance in this research work. The author wishes to acknowledge the High Voltage Research group at University of the Witwatersrand for funding this research. Gratitude is also extended to Hylton Dettmer for his mentorship in Elspec Sapphire software as well as Givemore Chitungo for his technical support. The debt of gratitude goes to Emmanuel Kasese for the continued support and always believing in me.

## Table of Contents

1. INTRODUCTION .....	8
1.1 Routine Based Maintenance .....	8
1.2 Diagnostics Driven Maintenance .....	9
1.3 Trend Based Maintenance .....	10
1.4 Smart Maintenance .....	10
1.5 The Problem Statement .....	11
1.6 The Research Question .....	11
1.7 Research Approach .....	12
1.8 Summary and Conclusion .....	13
2. LITERATURE REVIEW OF POWER CABLE SYSTEM RELIABILITY MODELS..	14
2.1 The Mazzanti and Mazinotto HVDC Cable System Reliability Model .....	14
2.2 The Weakest Link Principle (WLP) .....	16
2.3 The Inverse Power Model .....	17
2.4 Arrhenius Law .....	17
2.5 The Transient Electro-Thermal Model .....	17
2.6 The Resultant Electrothermal Model .....	18
2.7 Summary and Conclusion .....	20
3. THE CASE STUDY OF 88 kV XLPE CABLE TERMINATIONS .....	21
3.1 The Case Study Cable System Outline .....	21
3.2 The Case Study Data .....	24
3.3 Forensically Identified Degradation Mechanisms .....	28
3.3.1 Thermomechanic Degradation .....	28
3.3.2 Galvanic Corrosion .....	31
3.3.3 Electrothermal Degradation .....	34
3.4 Summary and Conclusion .....	36
4. DEVELOPING THE RELIABILITY MODEL .....	37
4.1 Statistical Distribution Analysis of the Termination Failure Data .....	38
4.2 The Electrical Degradation .....	42
4.2.1 The Steady State Electric Stress Factor ( <i>asse</i> ) .....	43
4.2.2 The Impulse Electric Stress Factor ( <i>atmp</i> ) .....	46
4.2.3 Electric stress factor $\alpha(E, E_i)$ .....	47

4.2.4	Effect of System Irregularities on the Electrical Life of the Termination .....	49
4.3	The Thermal Degradation Mode .....	53
4.3.1	The Eyring Model .....	54
4.3.2	The Miners Law .....	55
4.3.3	Transient Temperatures: Cigre Two Loop Network and Fourier Heat Equation ..	55
4.3.4	Thermal stress factor $\alpha(t, T)$ .....	58
4.4	The Electrothermal Reliability $R(E, T)$ .....	60
4.5	Thermomechanic Fatigue and Fracture Mechanism Model.....	61
4.5.1	The Coffin-Manson Model for Fatigue Degradation.....	61
4.5.2	The Landzberg and Norris Model.....	62
4.5.3	The Thermomechanic fatigue stress life factor, $\alpha(N)$ .....	63
4.5.4	The Resultant Thermomechanic fatigue Reliability, $R(N)$ .....	64
4.6	The Galvanic Corrosion Degradation Model .....	66
4.6.1	The corrosion stress life factor, $\alpha(C)$ .....	68
4.6.2	The Corrosion Reliability, $R(C)$ .....	70
4.7	Summary and Conclusion .....	72
5.	THE OVERALL RELIABILITY MODEL FOR THE TERMINATION .....	73
5.1	The Generic Model Philosophy.....	77
5.2	Summary Conclusion .....	78
6.	CONCLUSION .....	79
6.1	Thermomechanic Reliability .....	79
6.2	Corrosion Reliability .....	80
6.3	Electrothermal Reliability .....	80
6.4	Conclusion Summary .....	80
	REFERENCES .....	82
A.	APPENDIX .....	90
A.1	Electric transients .....	90
A.2	Electric Field Simulations .....	91
A.3	Thermal Simulations .....	92
A.4	Supplementary Data .....	92
B	Author's Journal Publication .....	95

## List of Figures

Figure 1.1 Combining statistical methods and degradation models to obtain the reliability model .....	12
Figure 2.1. Reliability with time at different electric stresses for an HVDC cable system by Mazinotto and Mazzanti -[11] (Used here with permission from Mazzanti).....	18
Figure 2.2. Reliability at different cable lengths (Mazinotto and Mazzanti) [2] (Used here with permission from Mazzanti).....	19
Figure 2.3. Reliability at different electric -field stresses for different number of cable system accessories [2] (Used here with permission from Mazzanti) .....	19
Figure 3.1. An 88 kV Out-door sealing end in a metropolitan municipal substation.....	21
Figure 3.2 Single line drawing of system in which the cable exists .....	23
Figure 3.3 Load cycle profile ( winter month).....	25
Figure 3.4 Lightning strokes location 2 km radius around case study substation [49].....	26
Figure 3.5 Transients captured by the data logging system [40] .....	27
Figure 3.6 Fatigue fracture caused by thermal-mechanic stresses on copper bell housing to copper braid S7 wiped joint.....	29
Figure 3.7 (a) Cross-sectional view showing the tin annealed wire that attaches the copper braid to the aluminium foil sheath (b) Evidence of crevice corrosion at contact point between the foil sheath and copper braid.....	29
Figure 3.8 Forensic evidence showing the degradation of the termination initiated by thermo-mechanic fatigue.....	30
Figure 3.9 Cross sectional view of an 88 kV XLPE cable termination [25] (Courtesy of Patrick O'Holloran) .....	31
Figure 3.10. Damaged putty due to fault current surge .....	32
Figure 3.11. Evidence of galvanic corrosion. (a) Tinned Copper braid fastened to the copper bell housing with annealed copper wire and wiped with S7 solder. (b) Tinned copper braid fastened to CSA and Aluminium foil with tin annealed copper wire.....	32
Figure 3.12. Corrosion electron flow at CSA and copper braid joint .....	33
Figure 3.13 Electrothermal failure in case study cable terminations (a) Thermal failure at CSA end, evidence of melted LDPE jacket. (b) Thermal fault within compression ring. (c) Corrosion of aluminium foil sheath, erosion and thermal failure of semiconductor.....	34
Figure 3.14 Different current paths. Under normal and faulty metallic earth connection [34], Obtained from Patrick O'Hollaran .....	34

Figure 3.15 Fault current path (red dotted line) when the copper braid is compromised Fault current and charging current path when copper braid is functional (green solid line).....	35
Figure 4.1. Bath tub curve that is used to categorize causes of failure using the failure rate [14] .....	39
Figure 4.2. Weibull probability distribution of case study 88 kV cable terminations time-to-failure.....	41
Figure 4.3. Statistical distribution of RMS voltage over one year (Data logged by online monitoring system) .....	43
Figure 4.4. Electric field distribution inside the cable termination at maximum peak steady state voltage 73.6 kV.....	45
Figure 4.5. Recorded switching transient .....	47
Figure 4.6. Effect of varying switching electric field strength and impulse count on reliability for terminations in the case study substation after 29 years in operation. ....	49
Figure 4.7. Lightning surge at the termination. ....	50
Figure 4.8. Electric field distribution in the termination during lightning impulse in the absence of grounded surge arrester .....	50
Figure 4.9. Electric field distribution in the termination during lightning impulse in the presence of grounded surge arrester .....	51
Figure 4.10. Maximum recorded ground-to-earth fault current.....	52
Figure 4.11. Phase-to-ground fault voltage.....	52
Figure 4.12. Sheath voltage at maximum fault current (a) Sheath voltage when there is single point bonding (SVL is functional and copper braid is grounded at termination end). (b) Sheath voltage when termination end is not grounded and SVL is not functional .....	53
Figure 4.13. Average daily winter temperatures.....	56
Figure 4.14. Typical daily seasonal load cycle extracted from one year's operation data .....	56
Figure 4.15. Temperature changes with worst case load current profile trend.....	57
Figure 4.16. Temperature inside the termination at earth fault current .....	59
Figure 4.17. (a) Existing electrothermal reliability ( $R_{sys}$ ) model for an HVDC 150 m cable system without joints (reproduced with permission from Mazzanti [1]) (b) Steady state electrothermal reliability of the case study cable .....	60
Figure 4.18. Thermo-mechanic fatigue factor at changing thermal cycles and fixed temperature .....	65
Figure 4.19. Thermo-mechanic fatigue factor at changing temperature range and fixed thermal cycle frequency.....	65

Figure 4.20. V-pH diagram of Aluminium and copper at 25 °C. Adopted from [80] .....	68
Figure 4.21. Reliability under corrosion at different humidity's and corrosion activation energy .....	71
Figure 5.1. Weibull Cumulative probability of failure with time at 29 years in operation due to all degradation mechanisms.....	74
Figure 5.2. Overall reliability after 29 years in operation.....	75
Figure 5.3. Effect of Sn60Pb40 solder and absence of galvanic corrosion on reliability of the termination.....	76
Figure A.1. A simplified simulation circuit of switching surge in ATPDraw.....	90
Figure A.2. Transmission line parameters .....	91
Figure A.3. JMarti 2 km transmission line parameter values ATPDraw.....	91
Figure A.4. Temperature from conductor (363.15 K) to wiped joint .....	92

## **Abbreviations**

**CSA** Corrugated Seamless Aluminium

**GIS** Gas Insulated Switch Gear

**HFPD** High frequency partial discharge

**HVDC** High Voltage Direct Current

**IPL** Inverse Power Law

**RCM** Reliability Centered Principles

**SVL** Sheath Voltage Limiter

**SiR** Silicon Rubber

**WLP** Weakest Link Principle

**LDPE** Low Density Polyethylene

## Authors Publications

<b>Title</b>	<b>Publisher</b>	<b>Co-Author</b>	<b>Status</b>
A Reliability Assessment Model for an Outdoor 88kV XLPE Cable Termination	Elsevier Electric Power Systems Research Journal	C. Nyamupangedengu	Accepted for Publication (See Appendix B)
A Mathematical Reliability Model for an 88 kV XLPE Cable Termination	South African Universities Power Engineering Conference (SAUPEC2018)	C. Nyamupangedengu	Published
Early Detection of Impending Failure in HV Cable Terminations - An Intelligent Asset Management Necessity	Association of Municipal Electricity Utilities (AMEU convention 2019)	P. O'Holloran and C. Nyamupangedengu	Accepted for Publication

# 1. INTRODUCTION

To facilitate the transmission and distribution of electricity, robust overhead lines and underground cable systems are required. In urban areas, underground cable systems are necessary for the transmission and distribution of electricity due to space limitations. It is therefore important that underground power cables do not prematurely fail. Most cable systems are designed to last at least 40 years, however, terminations and joints are the vulnerable areas of premature failure. This is because cable accessories are assemblies of different materials that are susceptible to failure due to their complexity and presence of discontinuities which lead to easy exposure to impurities during manufacturing or installation [1]. Therefore, the remaining life of a cable accessory is a function of the remaining life of its subcomponents and also influenced by operating conditions.

While there are life models for cable systems derived from historical performance records which are supported and standardised through accelerated aging tests, to the author's knowledge, based on literature research, there exists no reliability model for cable accessories alone. The presence of more terminations than joints in substations warrants the need to develop life models for cable terminations to increase substation reliability.

The maintenance engineer for substations is tasked to make asset management decisions to ensure a continuous supply of electricity, safety of substation on-site personal and minimize the cost of electricity distribution. Maintenance philosophies have evolved from time-based schedules to the use of historical trends combined with online diagnostics (condition-based maintenance). A review of literature in the evolution of maintenance philosophies is presented in the next subsections.

## 1.1 Routine Based Maintenance

The development of polyethylene in 1941 [2] resulted in the use of extruded power cables. Extruded cables were assumed to be more reliable and expected to last a design life span of at least 40 years. During the 1960's when extruded cables had been widely adopted for underground urban distribution, their limitations were soon realized as cables were reported to fail prematurely [2]. The drawbacks resulted in research work to improve extruded cable systems and power utilities began recording failure rates.

Failure rates of cable systems were computed per annum or as a function of distance, depicting old and new cables in the same measure [3],[2]. Routine substation maintenance was conducted offline at specific intervals which became economically challenging and impractical as electricity demand grew and the use of electricity in mass production and key industries required a continuously reliable supply. Electricity production and supply shifted to become a business-driven mostly deregulated industry where the transmission and distribution of electricity needed to be achieved at the lowest cost while ensuring there were minimal power supply interruptions. These developments propelled research into online diagnostics to assess the condition of cable systems without interrupting supply. Maintenance decisions became more informed by data obtained from condition assessment tests. In the next section condition assessment tests in cable systems are presented.

## **1.2 Diagnostics Driven Maintenance**

The introduction of partial discharge testing techniques in standards such as IEC 60270 [4] provided a way of monitoring the integrity of cable systems. However partial discharge testing was only initially conducted offline. Subsequently, the introduction of online PD diagnosis such as according to standard IEC 62478 provided more information that has enabled proactive maintenance. Moreover the adoption of reliability centered principles (RCM) [5] subsequently reduced annual failure rates and cost of distribution and transmission.

Advances in the understanding of partial discharge diagnosis technology [6] in determining the location or nature of a defect provided more information that influenced the decisions taken by the maintenance engineer. Despite advancement in PD diagnosis technology it cannot be used to precisely predict the remaining life of equipment.

Partial discharge testing can show the presence of a defect within the cable system but cannot give a long-term projection on the reliability as a function of the operating parameters and site conditions. Considering the limitations with cable system diagnostics, maintenance engineers also rely on the knowledge of cable life and historical trends obtained from laboratory tests. Trend based maintenance is presented in the next section.

### 1.3 Trend Based Maintenance

Utility cable systems' acceptable failure rates were statistically derived from laboratory tests and standardized in IEC 60071 [7]. They were pegged to an acceptable failure rate of 0.001/year to 0.004/year depending on the distribution, magnitude and duration of over voltages as well as the frequency of maintenance [7]. In IEC 60071 [7] the risk of failure under impulse voltages is statistically quantified as shown in *Equation 1.1*.

$$R = \int_0^{\infty} f(U) \times P(U) dU \quad (1.1)$$

Where  $f(U)$  is the probability density of over-voltage and  $P(U)$  is the probability of flash over under an impulse magnitude  $U$ .

It is not adequate to depend on trends alone for maintenance decisions due to the stochastic causes of failure. To acquire a more accurate projection of failure, a deterministic model that uses operating conditions should be supplemented to existing failure trends and combined with the outcomes of condition assessment tests. This results in a smart maintenance philosophy which is presented in the next section.

### 1.4 Smart Maintenance

As the grid becomes more complex, and the increasing need to make more informed decisions on which designs are suitable for specific environments and load profiles, an agile solution is required to influence maintenance decisions. The introduction of online data logging systems in power utilities [8] and smart instrumentation allow the combined use of real time trend and condition based maintenance. The IEC 61850 standard [9] provides an overview of network protocols and instrumentation that can be used to achieve real time monitoring of substations.

Although installed instrumentation can provide operating parameters which give the maintenance engineer an idea of the magnitude of stresses in the terminations, it does not give a deterministic projection of remaining life. In the literature, remaining life models for cable systems have been developed by mathematically modelling the physio-chemical modes of failure, where the mathematical models comprise of the operating parameters and material specific parameters.

In the present work a smart solution for informed asset management is presented by using the outcome of a case study. In the next section the problem and research questions are presented.

## **1.5 The Problem Statement**

In the literature there exists a reliability model for cable systems, however there is no reliability model for cable accessories. The reliability of cable accessories in substations is critical as substation failure results in widespread electricity supply interruption. In a substation, there are more terminations than joints, therefore there is a need for a model that can be used for risk evaluation of termination failure.

Why is there no reliability model for cable accessories? It is due to the absence of accessory operating parameters exacerbated by accessory complexity. The complexity of a cable accessory results in various possible modes of failure that may occur in synergy, continuously or intermittently. The research question is presented in the next subsection.

## **1.6 The Research Question**

***What generic reliability model for cable terminations can be devised and that is adaptable to specific designs and site-specific conditions?***

Most of these failure modes cannot be identified by online condition monitoring methods. If all the constituent modes of failure are identified, what analytical deterministic model can be developed based on the scientific physics of failure of each degradation mechanism? Which operating parameters accelerate failure and which system irregularities introduce high stresses in cable terminations? How can the degradation-based models be used to identify the most prevalent failure mechanisms, and how can these models be used to make design recommendations? The methodology adopted in conducting this research work is presented in the next subsection.

## 1.7 Research Approach

The approach entails adopting the existing cable system reliability model which includes combining a statistical distribution of time-to failure with a deterministic analytical models of failure mechanisms [10], as illustrated in *Figure 1.1*.

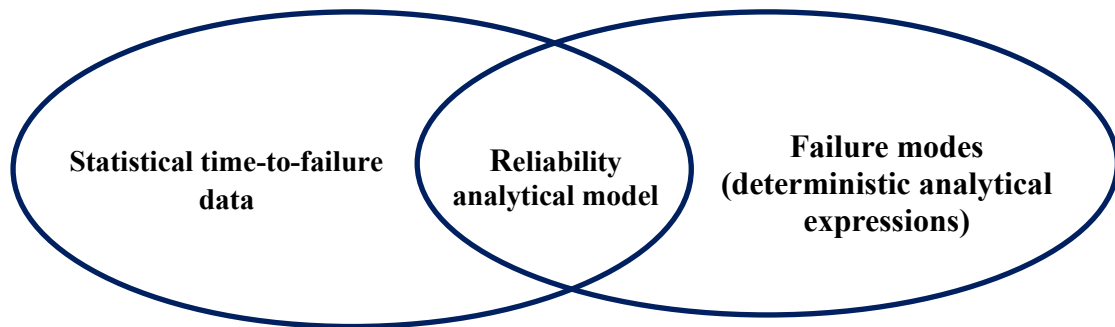


*Figure 1.1 Combining statistical methods and degradation models to obtain the reliability model*

The research methodology is summarized as follows;

- Conduct a literature review on existing reliability models.
- Forensically identify and model the failure modes in the case study cable terminations
- Collect annual recorded site weather conditions.
- Collect maintenance dates and note surrounding infrastructural changes in the vicinity of the cable terminations.
- Obtain the time-to failure data of the cable terminations in the case study substation.
- Fit the time to failure data to a suitable statistical distribution that computes the probability of failure.
- Construct the aggregate reliability model using statistical time-to-failure data, operating parameters and the physics of failure modes.
- Validate the model through comparisons with existing models, parametric method and its sensitivity to system irregularities, such as a faulty SVL and a non-grounded station surge arrester affect the reliability of terminations.
- Generalize the model for adaptability to different designs

## **1.8 Summary and Conclusion**

By using a case study and the premise of an existing electro-thermal reliability model for cable systems, the present research seeks to address the knowledge gap in modelling the remaining life of cable accessories. The research approach and methodology were presented. The existing reliability model that is adopted in developing the reliability model for cable terminations is presented in the next section.

## 2. LITERATURE REVIEW OF POWER CABLE SYSTEM RELIABILITY MODELS

---

An existing electro-thermal reliability model in the literature is reviewed. The model is for a DC cable system. The model is based on statistical time-to-failure data and electro-thermal physical degradation mechanisms. In the model an increase in the number of accessories and an increase in cable length cause reduce cable system reliability. The model is sensitive to parameter changes and it is limited by the assumption that cable systems have only two degradation mechanisms that are, electric and thermal degradation. The model, however, provides a basis for further development into incorporating other degradation mechanisms which is the objective of the present research work.

---

### 2.1 The Mazzanti and Mazinotto HVDC Cable System Reliability Model

A reliability model for high voltage direct current (HVDC) cable system has been developed by Mazinotto and Marzzanti [1]. This model was based on the combined thermo-electric models of accelerated aging tests by various researches such as Dimitri et al [11]. In this model electric and thermal stresses occur in synergy [11]–[16]. The model used the highest operating steady state temperature and electric field stresses. Variants of this model that include transient temperature changes due to cyclic loading have been proposed by Mazinotto and Mazzanti [1]. The Mazzanti and Mazinotto's electro-thermal model was developed by obtaining statistical time to failure data and fitting it onto a Weibull distribution. The Weibull distribution computes the cumulative probability of failure as shown in *Equation 2.1*.

$$P_w(t, \alpha_{ET}) = 1 - \exp[-(t/\alpha \cdot \alpha_{ET})^\beta] \quad (2.1)$$

Where  $P_w(t, \alpha_{ET})$  is the cumulative probability of failure with time,  $\alpha$  is the 63.2<sup>th</sup> percentile time of failure (shape parameter) that is a function of the electrothermal physical failure mechanism represented by the stress life factor  $\alpha_{ET}$  and  $\beta$  is the shape parameter that is used to deduce the possible cause of failure.

The electric and thermal degradation processes were modelled using the IPM (inverse power model) and Arrhenius Law respectively [11]. *Equation 2.2* shows how the reliability is then computed using the cumulative probability of failure.

$$R_{ET}(t) = 1 - P_w(t, \alpha_{ET}) \quad (2.2)$$

Where  $R_{ET}(t)$  is the life fraction left due to electro-thermal degradation after operation time  $t$  and  $P_w(t, \alpha_{ET})$  is the cumulative probability of failure with time due to electro-thermal degradation.

The overall reliability of the system was then obtained by applying the WLP (weakest link principle). Mazinotto and Mazzanti's reliability model is given in *Equation 2.3*. It is essentially the product of cable reliability, joint reliability and termination reliability.

$$R = R_c \cdot R_{joi} \cdot R_{term} \quad (2.3)$$

An enlargement law is then used to apply the model to different cable system geometries [1], as shown in *Equation 2.4*.

$$R = R_c \cdot \left( \frac{N_v}{k_{P,E}} \right)^{n\beta_c} \cdot R_{joi} \cdot R_{term} \quad (2.4)$$

Where  $N_v$  is a constant that accounts for cable geometry differences,  $k_{P,E}$  is a constant which is a function of ratio of probabilities of failure under different electric stresses and the scale parameter,  $n$  is the endurance coefficient and  $\beta_c$  is the shape parameter of the cable. The detailed model is shown in *Equation 2.5*.

$$\begin{aligned} R &= \left[ \exp\left(-\frac{t}{\alpha \cdot \exp\left[\frac{-\Delta W}{k_B} \left(\frac{1}{T_{c0}} - \frac{1}{T_c}\right)\right]}\right)^{\beta_c} \cdot \left(\frac{N_v}{k_{P,E}} \cdot \frac{E_c}{E_{0c}}\right)^{n\beta_c} \right] && \text{Cable Reliability} \\ &\times N_{joi} \left[ \exp\left(-\frac{t}{\alpha \cdot \exp\left[\frac{-\Delta W}{k_B} \left(\frac{1}{T_{0joi}} - \frac{1}{T_{joi}}\right)\right]}\right)^{\beta_{joi}} \cdot \left(\frac{E_{joi}}{E_{0joi}}\right)^{n\beta_{joi}} \right] && \text{Joint Reliability} \\ &\times N_{ter} \left[ \exp\left(-\frac{t}{\alpha \cdot \exp\left[\frac{-\Delta W}{k_B} \left(\frac{1}{T_{0ter}} - \frac{1}{T_{ter}}\right)\right]}\right)^{\beta_{ter}} \cdot \left(\frac{E_{ter}}{E_{0ter}}\right)^{n\beta_{ter}} \right] && \text{Termination Reliability} \end{aligned} \quad (2.5)$$

Where:

- $R$  is the reliability of the cable system
- $t$  is time
- $\alpha$  is the 63.2th percentile time of failure
- $\Delta W$  is the activation energy
- $k_B$  is Boltzmann's constant
- $E_c, E_{joi}, E_{ter}$  are the maximum electric field stresses
- $E_{oc}, E_{ojoi}, E_{oter}$  are the maximum design electric field stress for the cable joint and termination
- $\beta_c, \beta_{joi}, \beta_{ter}$  are the shape parameters of the cable, joint and termination respectively.
- $n$  is the voltage endurance coefficient
- $N_{joi}, N_{ter}$  is the number of joints and the number of terminations respectively.
- $K_{P,E}$  a constant which is function of the ratio of probabilities of failure under different electric field stresses and the scale parameter.
- $N_v$  a constant that accounts for cable geometry differences.

The use of the product mathematical operator in computing the reliability of the cable system is based on the Weakest Link Principle which is explained in the next subsection.

## 2.2 The Weakest Link Principle (WLP)

The WLP principle states that the overall reliability is dependent on the most prevalent degradation mechanism in the system. Thus, the product of reliabilities under each mechanism quantifies the overall reliability as shown in *Equation 2.6*.

$$R(t) = \prod_{i=1}^N R_i(t) \quad (2.6)$$

Where  $R(t)$  is the reliability with time, and  $R_i(t)$  is the reliability of the  $i^{th}$  subcomponent in a system.

A cable termination is a system of various components such that the reliability of the system is a function of its subcomponents. The WLP is suitable for application in the context of the presence of competing degradation mechanisms ensuring that the most prevalent degradation mechanism sets the upper limit of reliability.

### 2.3 The Inverse Power Model

Typically, electric life under the influence of electrical stresses is modeled using the IPL (inverse power law) [10]. The electric life is a function of the ratio of maximum applied electric field stress to the designed maximum electric field and insulation voltage endurance coefficient as shown in *Equation 2.7*.

$$\alpha(E) = \left(\frac{E}{E_o}\right)^{-n} \quad (2.7)$$

Where  $\alpha_t(E)$  is the electric life due to steady state electric stress,  $E$  is the maximum electric stress  $E_o$  is the maximum designed electric field stress and  $n$  is the voltage endurance coefficient [1],[12]. In the existing electro-thermal model, the effect of impulse stresses was not considered. However, in the present case study impulse electric stresses are considered.

### 2.4 Arrhenius Law

The relationship between product life and temperature is modelled by Svante Arrhenius reaction equation, which is derived from the fundamental observation that failure occurs when a critical amount of reaction or diffusion has been reached [10]. *Equation 2.8* shows the Arrhenius life relationship model.

$$\alpha(T) = \alpha \cdot \exp\left(-\frac{\Delta W}{k_B}(1/T_0 - 1/T)\right) \quad (2.8)$$

Where  $\alpha(T)$  is the thermal life,  $\alpha$  is the 63.2<sup>th</sup> percentile time of failure that depends on material and design stress,  $\Delta W$  activation energy of the dominant insulation thermal degradation process.  $k_B$  is the Boltzmann constant  $T_0$  is the reference design temperature and  $T$  is an operation temperature in Kelvins.

### 2.5 The Transient Electro-Thermal Model

A refined version of the electro-thermal model includes thermal transients caused by load cycle variation. Thermal fluctuations within the cable are simulated using the CIGRE two loop transient network of a cable [11] under load cycle variation. The cumulative damage caused by thermal transient was evaluated by using Miners law [10] [12] as shown in *Equation 2.9*.

$$\alpha_{i,T} = \int_0^{\Delta t_i} \frac{dt}{\alpha[T_i(t)]} \quad (2.9)$$

## 2.6 The Resultant Electrothermal Model

The existing electro-thermal model estimates the reliability of a cable system with time under steady state synergistic electro-thermal insulation aging processes. A parametric approach was adopted to evaluate the model, where the electric field stresses, number of joints and cable lengths were varied [1]. The out-come of the parametric analysis showed the validity of the weakest link principle, where the presence of more accessories in the system reduced the overall reliability of the cable system as shown in *Figure 2.1* and *Figure 2.2*.

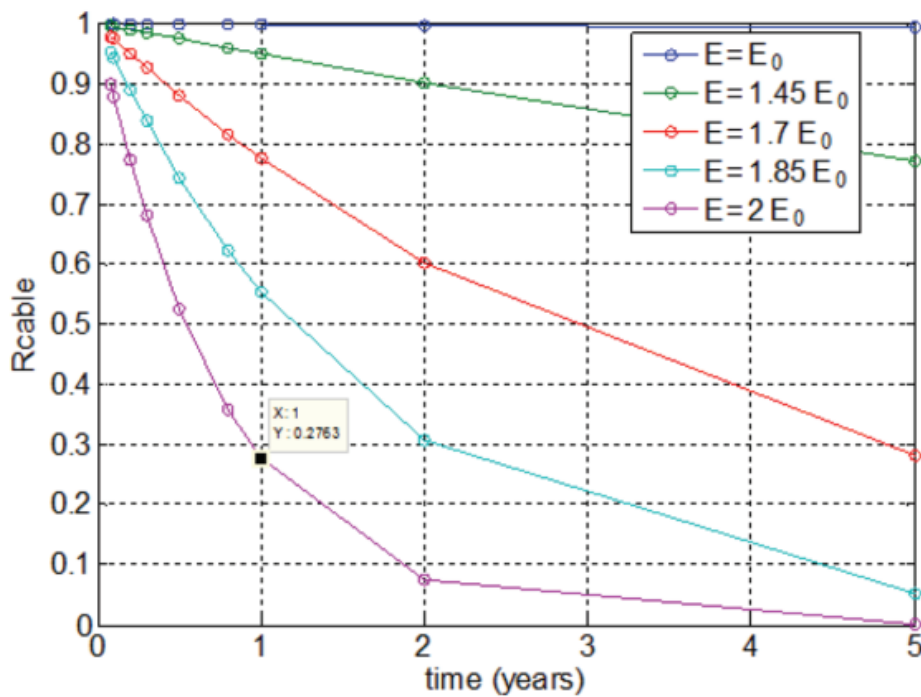


*Figure 2.1. Reliability with time at different electric stresses for an HVDC cable system by Mazinotto and Mazzanti -[11] (Used here with permission from Mazzanti)*

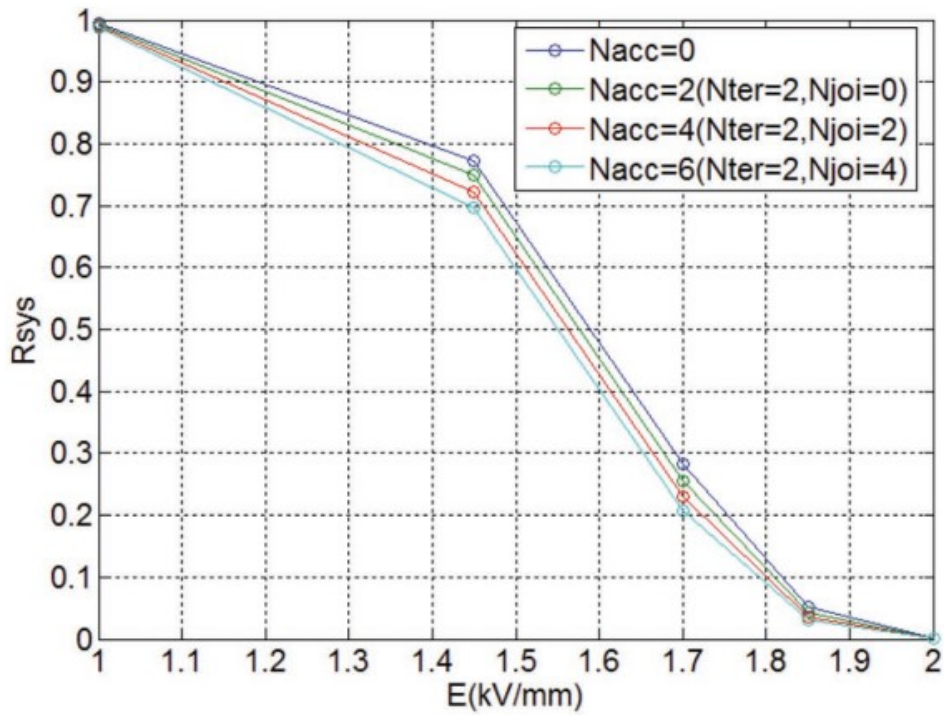


Figure 2.2. Reliability at different electric field stresses for different number of cable system accessories [2] (Used here with permission from Mazzanti)

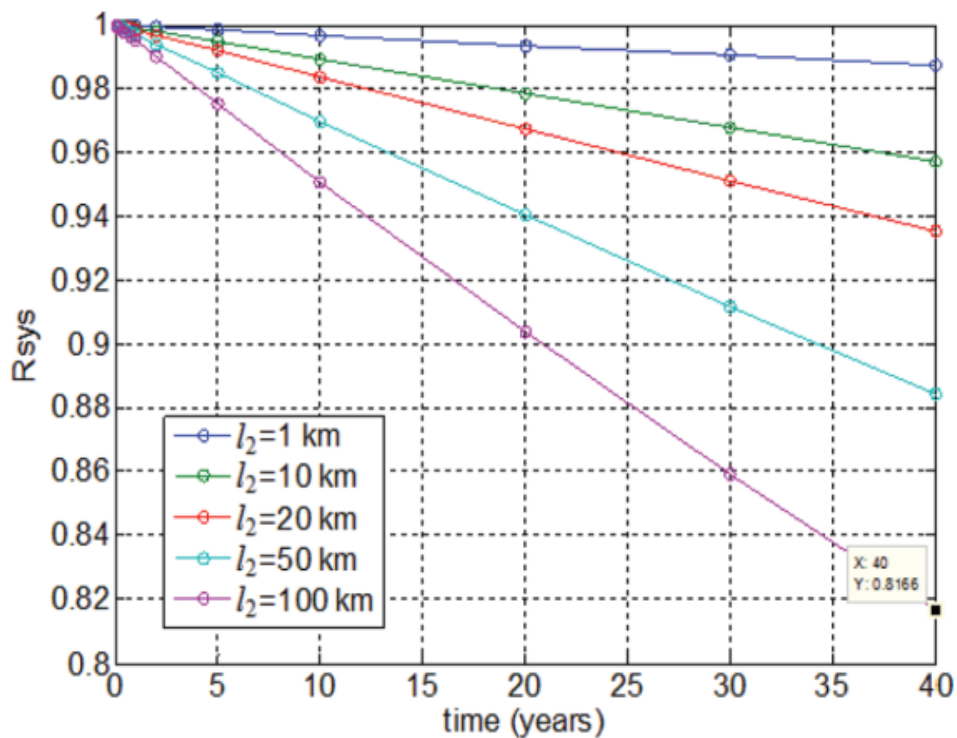


Figure 2.3. Reliability at different cable lengths (Mazinotto and Mazzanti) [2] (Used here with permission from Mazzanti)

The assumptions made in the existing electro-thermal model are listed below;

- Electro-thermal aging phenomenology is the most prevalent form of degradation in cable systems.
- The XLPE insulation part of the cable has the weakest thermal properties in the cable system
- Immediately after installation, the system is 100 % reliable if there are no defects introduced during manufacturing and installation.
- Mechanical failure mechanisms and transient electric stresses are negligible

Considering the above listed assumptions, there exists a knowledge gap in not only refining the existing model but extending it to include other possible degradation mechanisms, particularly for cable accessories. Firstly, given that the existing model was developed for an HVDC cable system, the possibility of adopting it to an AC cable system needs to be investigated. Secondly, the existing model considers termination and joints as comprising of the same material structure as the main cable and that the only predominant degradation mechanism is electro-thermal.

## **2.7 Summary and Conclusion**

The existing electro-thermal cable system reliability model assesses the reliability of a cable system with increase in cable accessories and cable section lengths. It proves that the increase of joints and terminations reduces system reliability in accordance with the WLP. The electro-thermal model presented above shows the existence of a knowledge gap, where the existing model may be tested on cable accessories as well as extended to include other degradation mechanisms. The case study of 88 kV XLPE cable terminations that are used to develop the reliability model is presented in the next chapter.

### 3. THE CASE STUDY OF 88 kV XLPE CABLE TERMINATIONS

---

A metropolitan municipal substation that has experienced prevalent failure of cable terminations is selected for this research. The cable system in which the terminations are installed, system irregularities and the forensically identified degradation mechanisms are presented.

---

#### 3.1 The Case Study Cable System Outline

An example of the 88 kV XLPE power cable terminations studied in the present work is shown in *Figure 3.1*. Twelve terminations (all in one substation) were investigated. Each termination has a metal oxide surge arrester connected in parallel at the out-door end of the cable link. Two terminations are connected in parallel per phase for the required current capacity in each link. The in-door end terminates into SF<sub>6</sub> gas insulated indoor switch gear. The cables are single core aluminum CSA (Corrugated Seamless Aluminum) cable designed for 76/132 kV but operating at 50.8/88 kV, *Table 3.1* presents more details of the cable specifications.

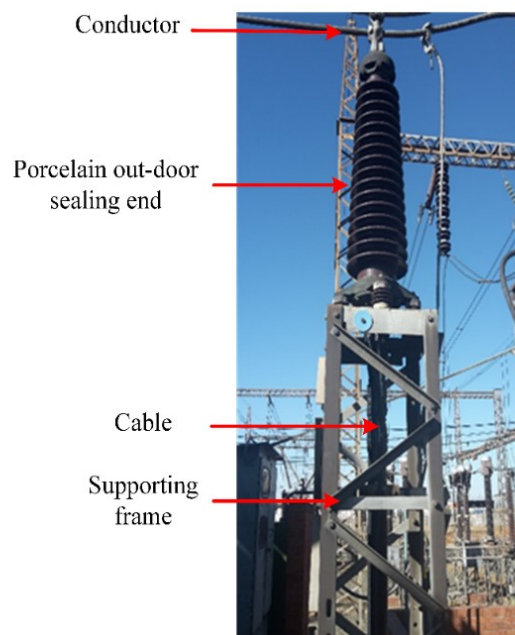
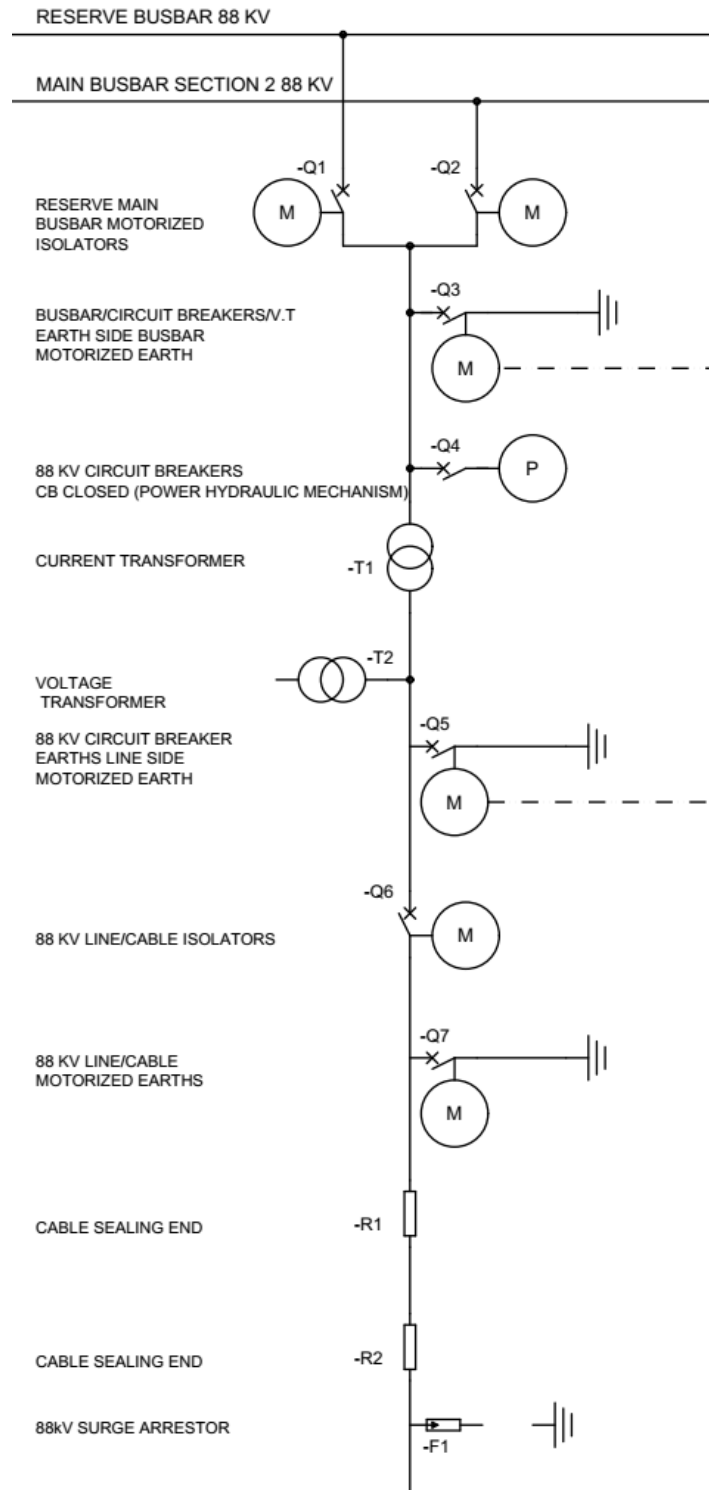


*Figure 3.1. An 88 kV Out-door sealing end in a metropolitan municipal substation*

Table 3.1 Case study cable specifications

<b>CABLE SPECIFICATIONS</b>	
Voltage Rating	76/132 kV but (operated at 88 kV)
Material	XLPE insulation CSA protective sheath Water blocking LDPE polyethylene jacket Aluminium conductor
Conductor Size	1000 mm <sup>2</sup>
Conductor Diameter	38.3 mm <sup>2</sup>
Diameter over s/c conductor screen	42.3 mm <sup>2</sup>
Diameter over XLPE insulation	75.4 mm <sup>2</sup>
Diameter over s/c core screen	77.9 mm <sup>2</sup>
Diameter over CSA sheath	98.0 mm <sup>2</sup>
Final diameter of cable	111.2 mm <sup>2</sup>
Reactance	Trefoil = 0.1268 Ω/km, Flat = 0.1848 Ω/km
Impedence	Trefoil = 0.1330 Ω/km, Flat = 0.1890 Ω/km
Sheath standing voltage	Trefoil = 43.7 Ω/km, Flat = 84.4 Ω/km,
Maximum electric stress at conductor screen	6.8 kV/mm (at nominal operating phase voltage)
Minimum electric stress at insulation screen	4.0 kV/mm (at nominal operating phase voltage)
DC resistance at 20 °C	0.0291 Ω/km
AC resistance at 90 °C	Trefoil = 0.0403 Ω/km, Flat = 0.0396 Ω/km
Earthing	Single point bonding
Length	100 m

The cable link is single point bonded at the outdoor termination end and there is an SVL Sheath voltage limiter at the indoor GIS (Gas Insulated Switch Gear) end. The substation system in which a termination exists is shown schematically in *Figure 3.2*. The substation is supplied by a power station located 15.44 km away and it feeds another substation that is 2 km away.



This diagram does not indicate the normal status  
i.e open or closed of any switching device

Figure 3.2 Single line drawing of system in which the cable exists

### 3.2 The Case Study Data

At the case study substation there is a data logging system (PQSCADA) [18], which records parameters such as voltage, current and zero sequence impedance every 1.54 milliseconds for every feeder. One year's data of operation was available at the time the reliability studies commenced. A tabulated description of the data used for this research work is presented in *Table 3.2*

*Table 3.2 Description of collected case study operating data*

<b>One year's operating data (Processed using PQSCADA Sapphire™software)</b>	
<b>Data Type</b>	<b>Data Description</b>
Summary report	Minimum, maximum and average of each recorded parameter
Cyclic histogram	Overlaid voltage waveforms showing deviation from expected ideal waveform
Energy	Consumption and production of active, reactive and apparent energy for selected time period
Statistics	Range and cumulative distribution of parameters
Event	System events in a given time range e.g flickering swelling, interruptions and rapid voltage changes.
Spectrum	Parameter harmonics and amplitudes
Raw data	Parameters in a given time range presented in a table or trend chart

In the data, the load cycle profile with the highest average current was selected and used in modelling the thermal degradation. *Figure 3.3* shows the load cycle profile in the month of June.

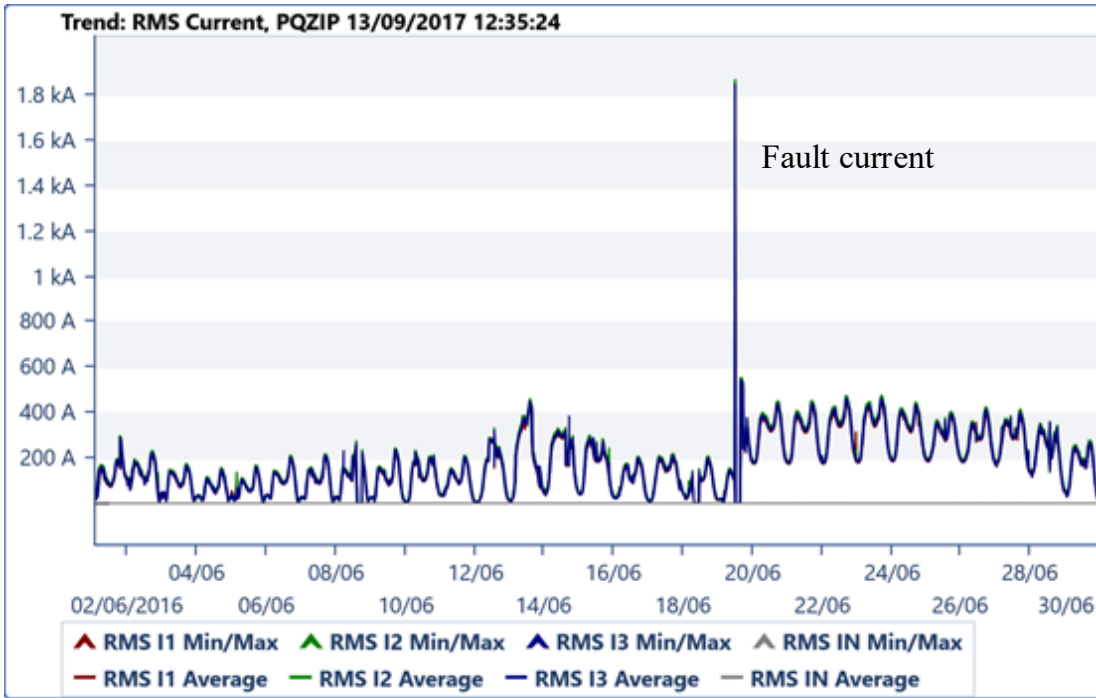


Figure 3.3 Load cycle profile ( winter month)

Lightning sensing instrumentation systems installed at the substation of interest and within its vicinity record the lightning strokes termination location and count. MapInfo™ [19] software is used to process the measured stroke count, current levels and the nature of the polarity of lightning (positive/negative). Lightning strike data within a 2 km radius of the case study substation was collected and is presented in *Table 4* and a visual map as given in *Figure 3.4*. An annual average lightning flash density flashes/km<sup>2</sup>/year of 7-10 was recorded in the vicinity of the substation, however no lightning voltage surges were identified in the online system monitoring data base.

If a lightning stroke terminates along the line, the possible peak current along the line is half of the maximum current recorded by the lightning detection system (See *Table 3.3*). The peak induced stress is a function of the impulse magnitude, impulse rise time, distance at which the surge is induced and the characteristic impedance of the system components. Using the peak

possible current of 87.75 kA and the characteristic impedances of the line, an induced voltage of 13.6 MV occurs if the lightning surge terminates within 2 km of the case study substation.

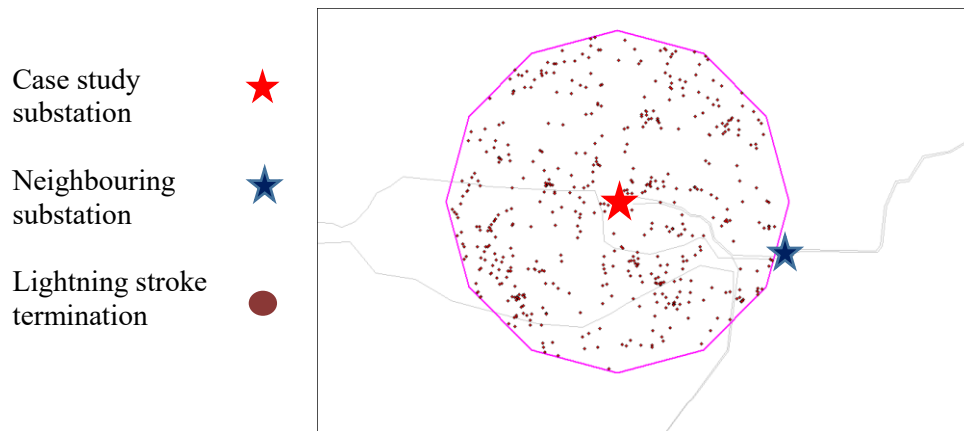
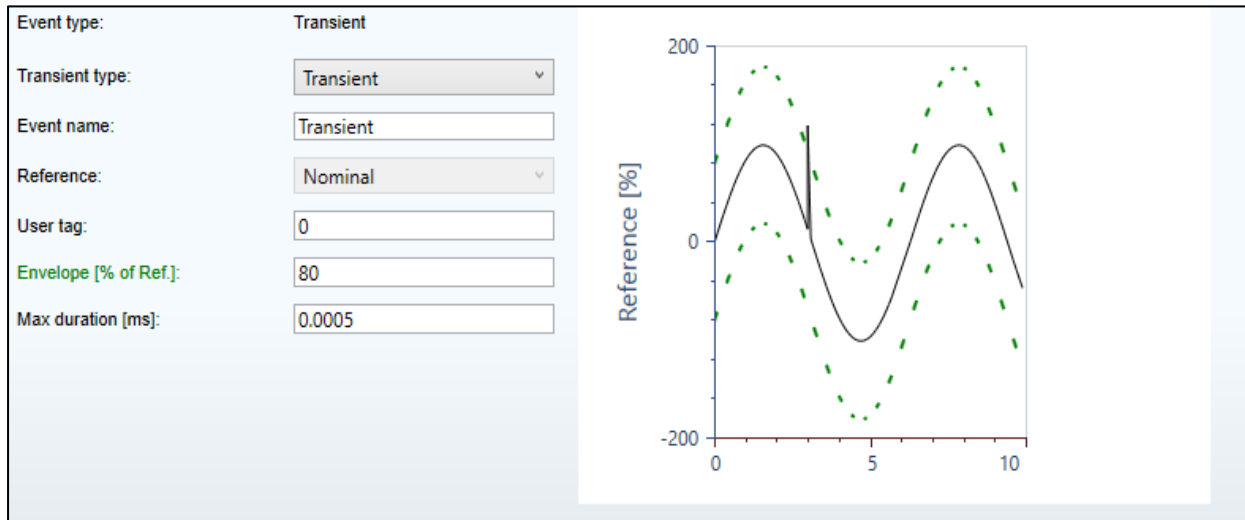


Figure 3.4 Lightning strokes location 2 km radius around case study substation [49]

Table 3.3. MapInfo Lightning strokes data in the vicinity of the case study substation

Lightning stroke counts	497
Negative counts	473
Positive counts	24
% Positive	4.8
density	41.4
Minimum current (kA)	5.1
Maximum current (kA)	175.6
Average current (kA)	17.9
Exp. factor	743.1
Negative minimum (kA)	5.1
Negative maximum (kA)	175.6
Negative mean (kA)	17.5
Positive min (kA)	10.5
Positive max (kA)	67.4
Positive mean (kA)	26.1

In the case study at hand, in one year's data, no lighting impulses were recorded but switching transients within a 1.5 millisecond resolution were detected. A typical switching transient record is presented in *Figure 3.5*.



*Figure 3.5 Transients captured by the data logging system [40]*

The terminations reliability studies commenced after the terminations had been in operation for 29 years. There were system irregularities worth taking note of in the study. The identified system irregularities include;

- There were no ground connections on all the surge arrestors at the substation due to prevalent copper theft. Information on the total time in which the terminations operated without a grounded surge arrestor was not available. The surge counter installed on the terminations had an impulse count of 21, but without any other reference data the count was meaningless (Some surge arrestors are installed onsite with a few test impulses conducted in the laboratory) .
- The SVLs (sheath voltage limiters) were permanently in a failed state, in any case the copper connections to ground were also missing. The forensically identified degradation mechanisms found in the cable terminations at the municipal substation are presented in the next section.

In the next subsections a qualitative presentation of the forensically identified degradation mechanisms is given.

### 3.3 Forensically Identified Degradation Mechanisms

From the post-mortem analysis, the prevalent degradation mechanisms of the terminations were as follows;

- Thermoelectric insulation aging
- Thermomechanic fatigue
- Galvanic corrosion

The forensic evidence shows that the degradation mechanisms occur synergistically but there exists a set of series of sequential events that occur concurrently. From the time of installation, the termination components are subjected to continuous electric and thermal stresses leading towards cyclic thermo-mechanic fatigue. Galvanic corrosion is initiated when there is moisture ingress into the termination. The scrapping investigations also show that thermomechanic fatigue compromises the termination by allowing moisture ingress which leads to galvanic corrosion. Subsequently, accelerated localized thermoelectric degradation occurs resulting in complete failure [20]. The thermomechanic evidence of failure is presented in the next section.

#### 3.3.1 Thermomechanic Degradation

Forensic evidence shows that two metallic interfaces in the cable termination fail due to thermal mechanic fatigue [20]. These metals are;

- S7 Solder that wipes the tinned copper braid to the copper bell housing
- Aluminium foil sheath where the tinned copper braid is fastened to the aluminium foil sheath using a tin annealed copper wire.

A crack was found on the S7 (PbSn35) solder that wipes the tinned copper braid to the copper bell housing as shown in the image of *Figure 3.6*. Failure of the copper braid-to-copper bell housing S7 wiped joint may be caused by shearing forces or contraction and expansion due to prolonged thermal fluctuations. Possible joint embrittlement due to the formation of intermetallic compound growth at the S7 and copper interface is dependent on temperature and pressure. However, significant intermetallic compound growth can only occur when the joint

temperature exceeds 250 °C for an extended time period [21]. Due to low operating temperatures of up to 90 °C in the case at hand, intermetallic compound growth is discarded.

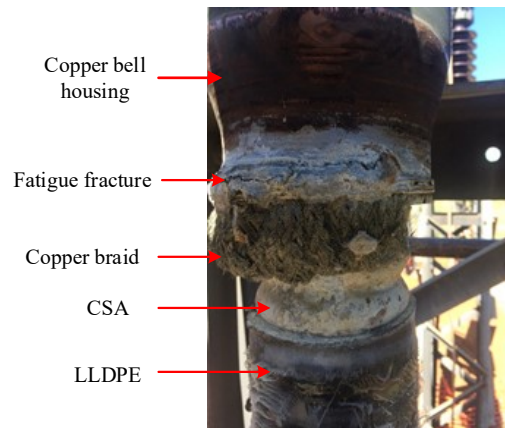


Figure 3.6 Fatigue fracture caused by thermal-mechanic stresses on copper bell housing to copper braid S7 wiped joint.

Another metallic interface that is subjected to mechanic strain is the tin annealed copper wire which fastens the copper braid onto the aluminium foil sheath [20] as shown in Figure 3.7.

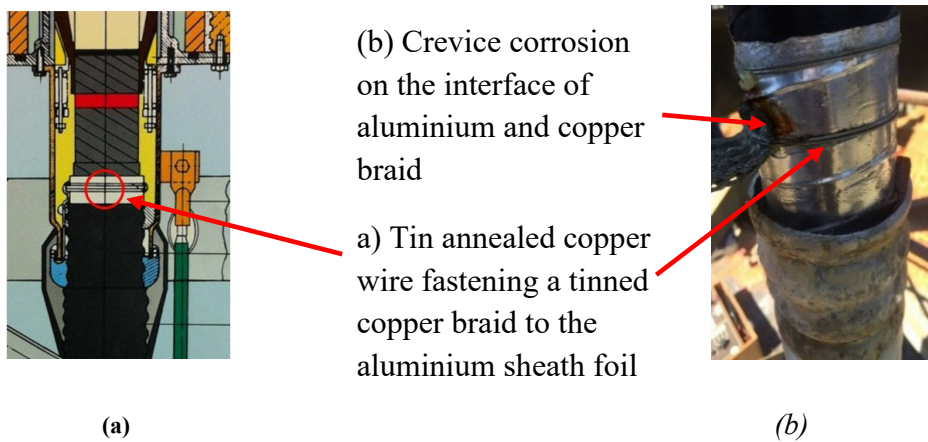
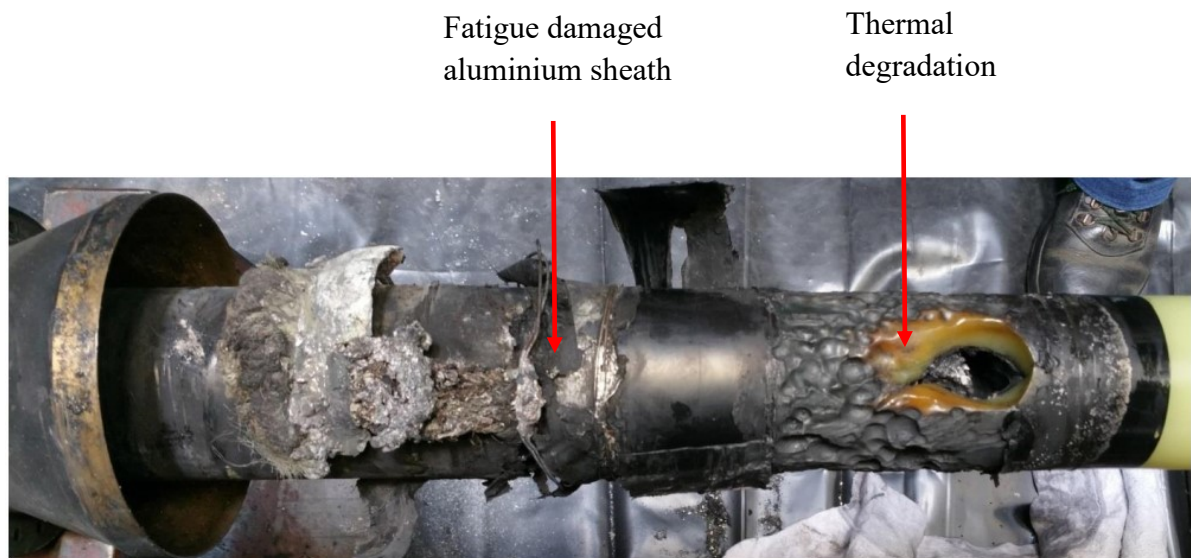


Figure 3.7 (a) Cross-sectional view showing the tin annealed wire that attaches the copper braid to the aluminium foil sheath (b) Evidence of crevice corrosion at contact point between the foil sheath and copper braid. (Courtesy of Patrick O'Holloran)

There are differences in the coefficient of thermal expansion between the foil sheath and tin annealed copper wire. Due to the small cross-sectional area of the aluminium foil sheath coupled with the force exerted onto it by the tin annealed copper wire, there is considerable cyclic

shifting of the sheath. The mechanical property differences of the aluminium sheath foil and copper braid are presented in *Appendix A.4*.

Each fault current surge accelerates the erosion of the semi conductive layer and induces forces that further strain the foil sheath at the point where the tin annealed wire fastens the copper braid. The aluminium foil sheath is spliced around the tin annealed wire introducing sharp points where localised corona occurs. *Figure 3.8* shows a spliced aluminium foil sheath end and accelerated thermal degradation at the semi-conductor end where a double layer of semi-conductive tape exists.



*Figure 3.8 Forensic evidence showing the degradation of the termination initiated by thermo-mechanic fatigue*

A cross-sectional view of the lower section of the cable termination is shown in *Figure 3.9*. The circled areas show metallic wiped connections that are vulnerable to thermal-mechanic fatigue and corrosion. These metallic connections include; tinned copper braid wiped with S7(PbSn35) solder to a copper bell housing and tin annealed copper wire that fastens the tinned copper braid onto aluminium foil sheath.

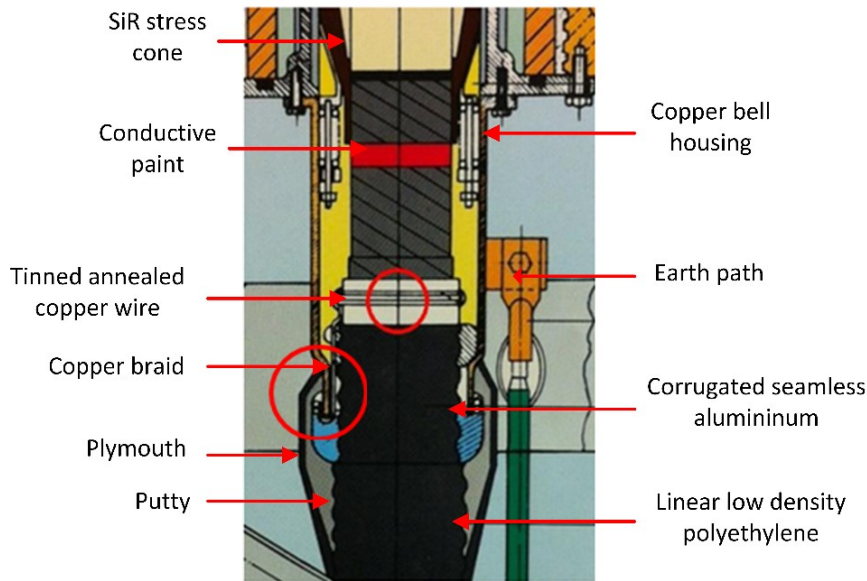


Figure 3.9 Cross sectional view of an 88 kV XLPE cable termination [25] (Courtesy of Patrick O'Holloran)

Ductor tests conducted on failed terminations showed a resistance of up to  $50 \text{ m}\Omega$  between the copper bell housing and the CSA instead of a maximum of  $30 \text{ }\mu\Omega$  [20], while HFPD (High Frequency Partial Discharge) tests were reported to show a sudden surge of partial discharge intensity particularly after a high-level fault current event as recorded through the online monitoring system. Some terminations were reported to have shown advanced thermal degradation when opened during post failure analysis. It is therefore evident that the loss of the critical fault current path introduces high stresses in the termination system.

### 3.3.2 Galvanic Corrosion

Forensic evidence shows galvanic corrosion by-products on the interface of the copper braid with CSA interface. This is initiated by moisture ingress which is permitted due to the following sequential failures;

1. Continuous expansion and contraction at the contact point where the heat shrink tube end is glued to the copper bell housing, results in a small opening. The subsequent layers of red sealant tape and plyjack tape are subjected to expansion and contraction that slowly loosens the taping [20].

2. Underneath the plyjack tape, the putty is slowly weakened by temperature variations creating micro-cracks that allow moisture ingress as shown in *Figure 3.10*. The shape of the copper bell housing allows water to be funnelled through the cracked material layers.



*Figure 3.10. Damaged putty due to fault current surge. (Courtesy of Patrick O'Holloran)*

3. Thermal mechanic fatigue fracture of the S7 solder that wipes the copper braid onto the copper bell housing creates an opening allowing galvanic corrosion where the copper braid is fastened to the CSA [20].

Evidence of corrosion exists in the form of galvanic corrosion by-products at the wiped joint between CSA and tin-plated copper braid as shown in *Figure 3.11*. This joint is wiped with Pb90 Sn10 solder.

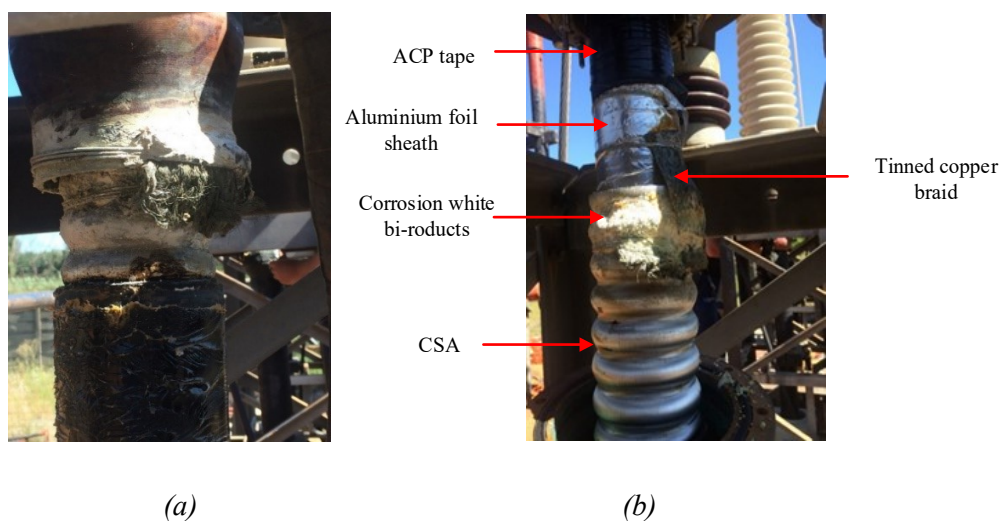


*Figure 3.11. Evidence of galvanic corrosion. (a) Tinned Copper braid fastened to the copper bell housing with annealed copper wire and wiped with S7 solder. (b) Tinned copper braid fastened to CSA and Aluminium foil with tin annealed copper wire.*

The physical position of the metals (aluminium and copper) relative to each other and the direction of moisture ingress creates a highly active galvanic cell. The tinned copper braid (cathodic) is placed above the CSA (anodic) and the moisture flows from the tinned copper braid to the CSA. This results in weak copper salts dropping onto the aluminium, thus drastically reducing the aluminium with time. If the aluminium is placed above the copper then the corrosion rate is much slower, as the natural flow of water opposes that of the electrical connection between copper and aluminium. The rate of corrosion is also a function of the nature of applied voltage. In an AC system the alternating flow of current results in a cyclic corrosion where in one half cycle corrosion is aided and in the other it is impeded. This allows the continuation of corrosion even when buffer corrosion by-products (e.g  $\text{Al}(\text{OH})_3$  [22]) cover the anode (CSA) which reverses the cell potential. The presence of 90/10 Sn/Pb (90% of tin and 10% lead) solder that joins the tinned copper braid and CSA slows down the corrosion process as there is a smaller difference in electron affinity between copper and Sn/Pb. Aluminium's position in the electrochemical series is modified by the oxide layer that naturally forms on its surface [23]. It is this layer that protects the sheath and CSA from further corrosion. However, the presence of weak acid or alkaline solutions result in a discontinuity of the oxide and tin layers.

The influence of aluminium oxide layer's high electrical resistance when immersed in weak neutral electrolytes will concentrate current in some areas in the termination structure resulting in pitting thus exposing it to galvanic corrosion [23]. The tin plating on the copper braid also provides temporary corrosion protection. The main direction of electron flow during galvanic corrosion at the tinned copper braid and CSA joint is illustrated in *Figure 3.12*.

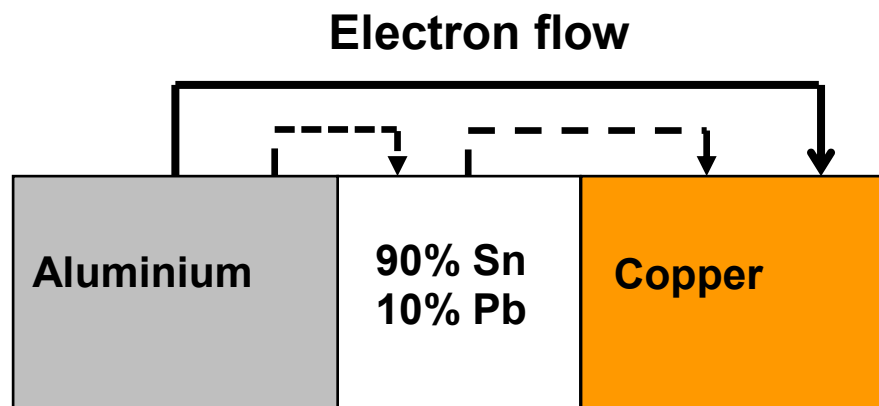


*Figure 3.12. Corrosion electron flow at CSA and copper braid joint*

Evidence of electrothermal degradation is presented in the next subsection.

### 3.3.3 Electrothermal Degradation

The completely failed cable terminations show evidence of accelerated thermal and electric degradation occurring in the vicinity of the sheath end. This evidence is shown in *Figure 3.13*.

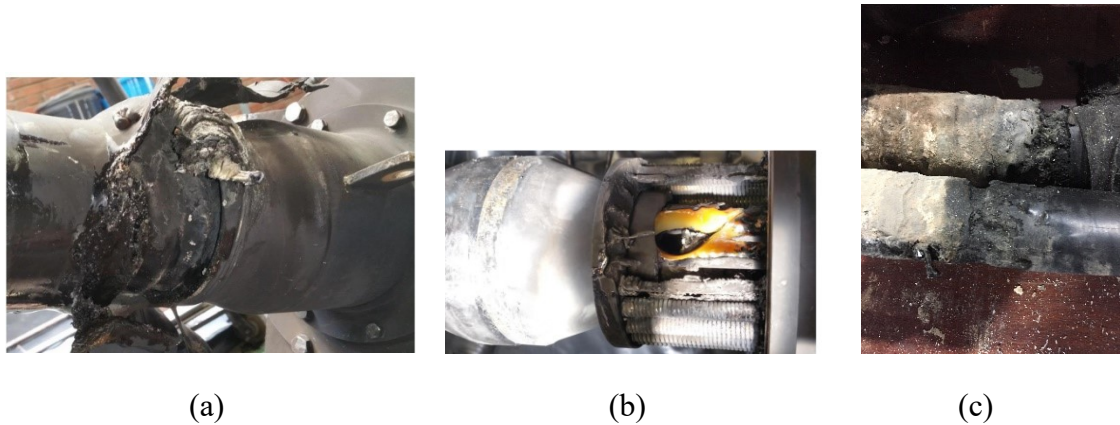


*Figure 3.13 Electrothermal failure in case study cable terminations (a) Thermal failure at CSA end, evidence of melted LDPE jacket. (b) Thermal fault within compression ring. (c) Corrosion of aluminium foil sheath, erosion and thermal failure of semiconductor. (Courtesy of Patrick O'Holloran)*

Thermal failure is caused by prolonged high currents while semi-conductor erosion is caused by transient surges in the cable system. The formation of the crack on the S7 solder as presented in Section 3.3.1 disrupts the fault current path resulting in the formation of an alternative fault current path as shown in *Figure 3.14*.

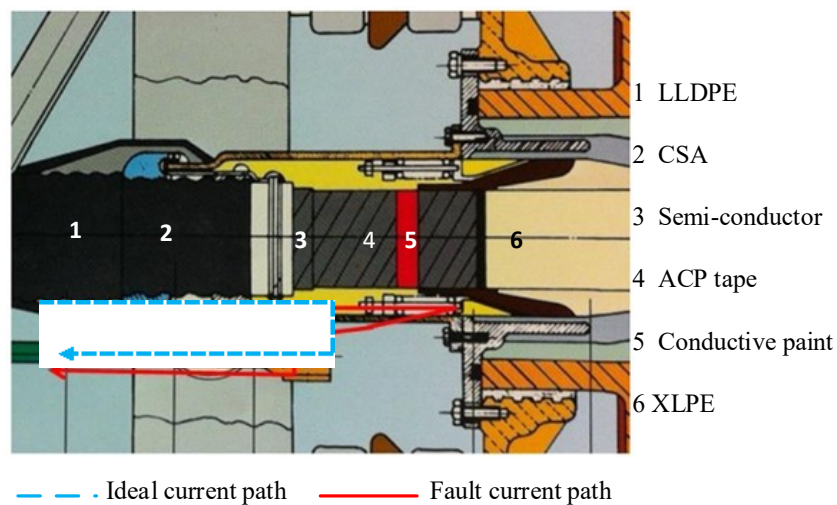


*Figure 3.14 Different current paths. Under normal and faulty metallic earth connection [20], Courtesy of Patrick O'Halloran*

An equivalent circuit of the termination is in *Figure 3.15* showing the current path under normal conditions and the current path when the wiped metallic joint has failed.

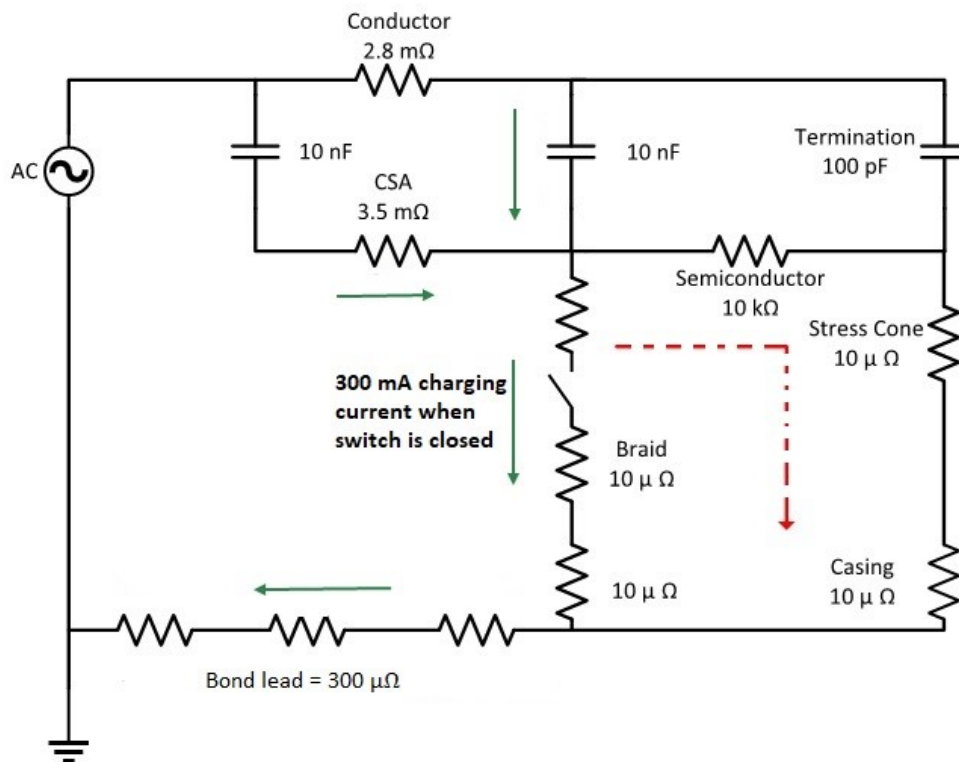


*Figure 3.15* Fault current path (red dotted line) when the copper braid is compromised Fault current and charging current path when copper braid is functional (green solid line)

When the earth connection is compromised the current flows across the semi-conductor towards the compression to the ground connection of the copper bell housing resulting in excess heat generation which thermally stresses and erodes the semi-conductor and XLPE insulation [20]. Under normal operating conditions a charging current of 300 mA results in up to 1 kW of energy generated across a 10 kΩ semi-conductor [20]. A maximum measured ground-to earth fault current of 9 kA within 300 ms can result in up to 800 kW of energy across a 10 kΩ semi-conductor equivalent resistance. This excess heat causes accelerated thermal degradation of the semi-conductor and insulation, as well as higher thermo-mechanic stress cycles. Therefore, an alternative fault current results in an increased rate of thermal degradation in the cable termination.

### **3.4 Summary and Conclusion**

Forensic evidence shows the existence of electro-thermal, corrosion and thermo-mechanic fatigue degradation mechanisms in the case study cable terminations. There are system irregularities that include, absence of a ground connected surge arrester and SVL. There is an opportunity of formulating a reliability model whose constituents are the various degradation modes presented in this chapter. The reliability model for the cable termination is developed in the next chapter.

## 4. DEVELOPING THE RELIABILITY MODEL

---

In this chapter the reliability model is developed by fitting the statistical time-to-failure data to a Weibull distribution and mathematically modelling the forensically identified degradation mechanisms. A detailed outline that includes literature reviews and computation of life stress factors and the reliability results for each degradation mechanism is presented.

---

A few assumptions are made based on the evidence obtained at the case study substation. The main assumptions made for this reliability model are listed below. Other assumptions pertaining to a specific stress classification will be given within the respective section.

- At time  $t = 0$ , the probability of failure is at zero assuming there are no manufacturing defects or installation errors (mechanical laying strain, contamination, splices, voids) in the cable termination. This assumption is made as the cable terminations have been functional beyond half their designed life-time.
- It is assumed that failure of the critical components within the termination will result in the failure of the entire termination. This assumption is made based on the forensic investigation conducted on failed cable terminations, which shows that loss of the ground-link results in increased thermal and electric stress distribution at sheath end and stress cone vicinities which results in accelerated degradation. If the sheath end or stress control mechanism fails, the ground-link is exposed to more thermal fluctuations thus accelerating the metallic fatigue and corrosion processes. The reliability is therefore dependent on the first component to fail within the termination in accordance with the weakest link principle [10].
- The same operational time data is used for all failure mechanisms.
- The life-time or reliability of the cable termination is always a positive value.

Following the listed steps undertaken in the study presented in Section 1.7 the reliability model is developed starting with the statistical time to failure data presented in the next subsection.

## 4.1 Statistical Distribution Analysis of the Termination Failure Data

The failure data of cable terminations in the case study is analyzed using a statistical distribution. The most suitable distribution analysis tool is selected based on the best fit criterion. Other researchers in life modelling of cable systems have used data censorship [24]. The concept of censorship is applied when the data sample includes failed and non-failed samples [24] and this is usually the case for observations made over an extended period. In the present work the Weibull distribution analysis technique was used to fit time-to-failure right censored data. The Whites method was adopted to take into account the small sample size as per recommendations in the standard IEC6253 [25] on statistical analysis of high voltage electric systems in [26],[25]. The Weibull distribution quantifies the probability of failure with time given the existing time-to-failure data as shown in *Equation 4.1* [10].

$$P_w(t) = 1 - \exp[-(t/\alpha)^\beta] \quad (4.1)$$

Where  $\alpha$  is the 63.2<sup>th</sup> percentile time of failure (shape parameter) that is a function of the physical failure mechanisms. The scale parameter  $\alpha$  is a measure of the probability of failure with time based on the degradation mechanisms. A lower scale parameter means more terminations fail during early life while a higher scale parameter means a much more normal distribution of failure [27]. The shape parameter  $\beta$  represents the shape of the distribution which is used to categorize the overall possible cause of failure.

The categories of failure include, early life failure, random failure and aging related failures as depicted by the bath tub curve [10] as shown in *Figure 4.1*. When  $\beta < 1$  the reliability increases with time and this characterizes premature early life failure. When  $\beta = 1$  the failure rate remains constant with time. When  $\beta > 1$ , the failure rate increases with time [27]. The slope  $\beta$  of the distribution can be obtained using *Equation 4.2*.

$$\beta = \frac{1.340}{\log_{10}(t_{90}/t_{10})} \quad (4.2)$$

Where  $t_{90}$  is the time where there is 90 % probability of failure and  $t_{10}$  is the time where there is 10 % probability of failure [36].

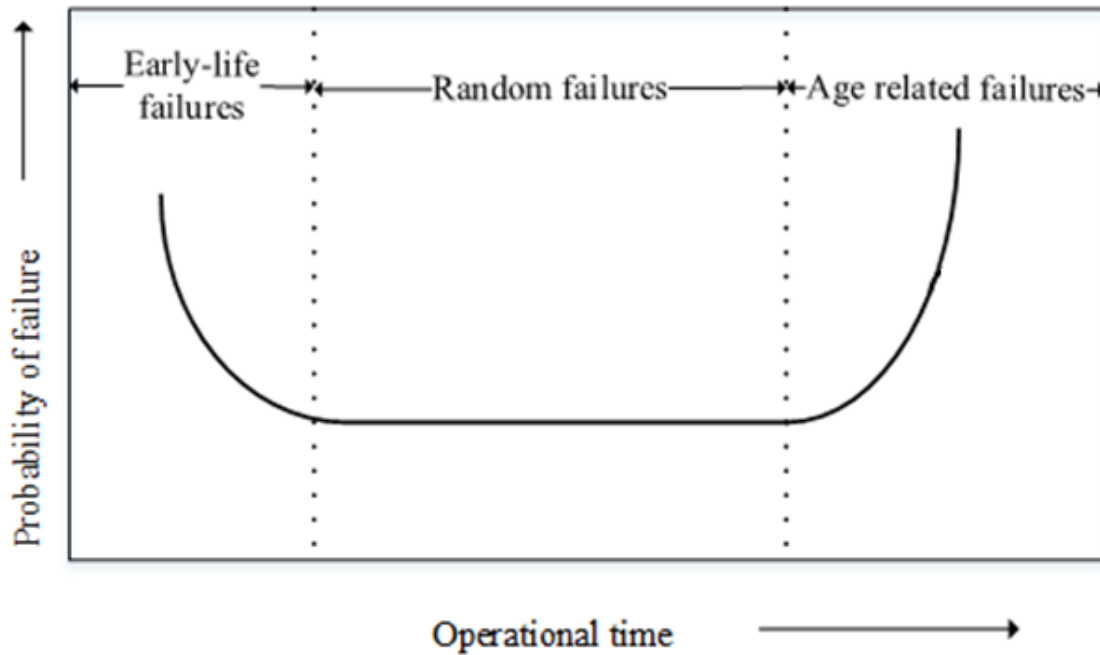


Figure 4.1. Bath tub curve that is used to categorize causes of failure using the failure rate [14]

Early life failure is caused by defects introduced during installation or manufacturing. Random failures occur due to the occurrence of surges caused by sudden load changes and lightning strikes, while age related failure is caused by operating conditions and natural wear and tear. In-service aging phenomenology is the most common cause of accessory failure.

At the time of study nine of twelve terminations had failed while the others were still operational. Failure occurs when;

- There is complete termination failure.
- Ductor measured resistance exceeds  $30 \mu\Omega$  at the CSA and copper bell housing interface [20].

Table 4.1 shows how the data was processed to get the cumulative probability of failure using the two parameter Weibull distribution function.

Table 4.1. Weibull distribution of right censored time of termination failure data by Whites method. \*p denotes that it is still operational\*

Time of failure (years)	$I(i) = I(i - 1) + \frac{n + 1 - I(i - 1)}{n + 2 - C_i}$	$P_w(i, n) = \frac{I(i) - 0.44}{n + 0.25} \times 100$
15	0.9	3.9
22.4	1.9	11.6
22.4	2.8	19.1
24.6	3.7	26.7
24.7	4.6	34.3
26.2	5.6	41.9
27.4	6.5	49.5
28.9	7.4	57.0
28.9	8.4	64.6
29 p	9.1	70.9
29 p	9.8	76.2
29 p	10.3	80.6

Where  $n$  is the number of samples,  $i$  is the rank from  $i = 0$  to  $i = n$  and  $C_i$  is the total number of failed terminations when the  $i^{th}$  breakdown occurs [34]. The 63.2<sup>th</sup> time of failure occurs in the 28<sup>th</sup> year in operation. The data set size is on the lower end but sufficient enough to meet the minimum size requirement as recommended in IEC 62539 [23] [27]. Nevertheless, in order to improve on accuracy, the data is censored. The stochastic nature of this distribution is evident in that a line of best fit is required to fit the probability of time-to-failure. A larger sample size with fewer terminations remaining in operation would give a distribution with a smaller error margin. *Figure 4.2* shows the Weibull cumulative probability obtained from the case study of termination time-to-failure and *Table 4.2* shows the Weibull parameters.

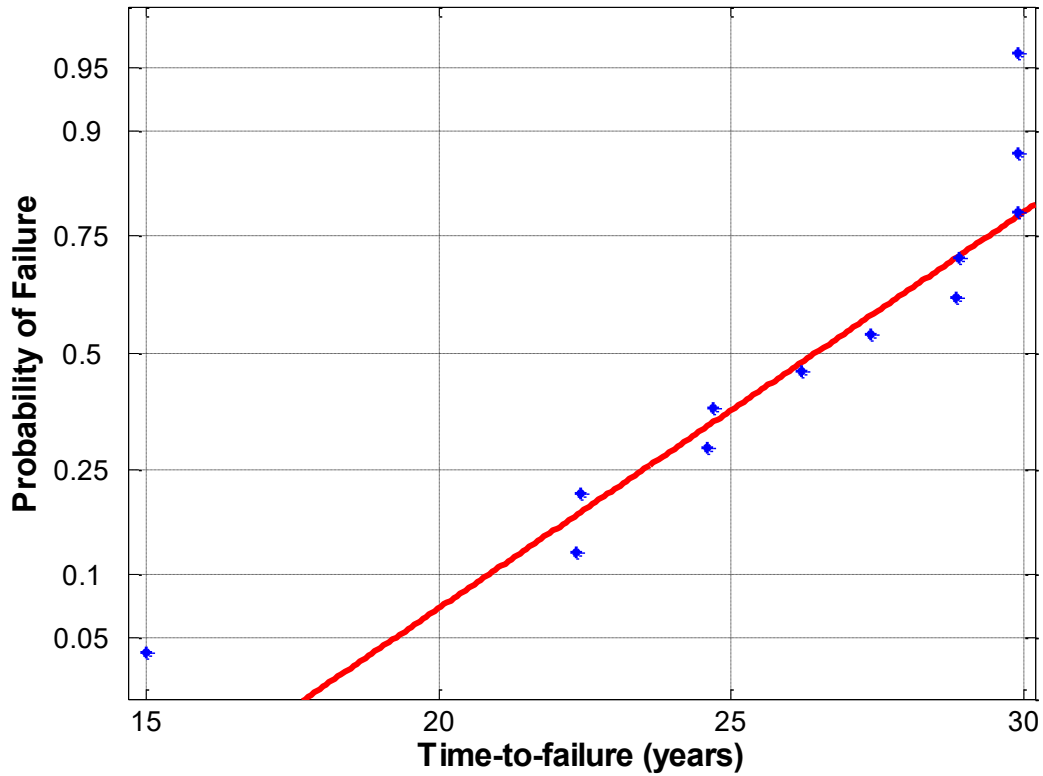


Figure 4.2. Weibull probability distribution of case study 88 kV cable terminations time-to-failure

Table 4.2. Weibull distribution probability parameters

Parameters	Value
Scale parameter: $\alpha$	29.9 years
Shape parameter: $\beta$	5.0
Sample number: $n$	12.0

The reliability  $P_{w2}(t, \alpha_x)$ , due to each mode of degradation is represented analytically by modifying Equation 4.1 through incorporating the life factor  $\alpha_x$  given in Equation 4.3.

$$P_{w2}(t, \alpha_x) = 1 - \exp\left[-(t/(\alpha_x \alpha))^\beta\right] \quad (4.3)$$

Where  $\alpha_x$  is the life-factor due to stress  $x$ . In this case study  $x$  either thermo-electric stress, thermo-mechanic stress and corrosion stress. In the next sections each mode of degradation is analyzed explaining how the corresponding life factor  $\alpha_x$  is determined and the resultant reliability.

## 4.2 The Electrical Degradation

Bahder et al [28] model electrical degradation of insulation based on the permeability of polymers. The small air pockets within an insulation gradually expand under alternating electric fields over the life-time of the insulation. Due to their minute size, there is no detectable partial discharge activity that occurs, however if the size of the air pocket is increased to a sizeable void, accelerated and measurable partial discharge activity will occur [29]. A partial discharge is initiated when the applied voltage exceeds the critical threshold voltage at which an electron is accelerated and bombards other molecules, thus creating more electrons. Sustained discharges are facilitated by the accumulation of space charge within the void, which slowly erodes the insulation by creating a channel until a complete bridge between electrodes is made. *Equation 4.5* shows the time to breakdown as a function of electric field by Bahder et al [28].

$$t_b = \frac{1}{f b_1 \{ [\exp(b_2(E - E_{th})) - 1] \exp(b_3 E_b) + b_4 \}} \quad (4.5)$$

Where  $t_b$  is the time to breakdown at stress  $E_b$ . Constants  $b_1$ ,  $b_2$ ,  $b_3$  and  $b_4$  characterise the critical crater depth.  $E_{th}$  is the threshold electric field stress.

The rate of insulation degradation is a function of the applied voltage (frequency and magnitude) [29]. This characteristic was confirmed by the increase in insulation dissipation factor with applied voltage frequency [30]. Furthermore results obtained by Cavallini et al [31] show that square unipolar and bipolar stresses drastically reduce the endurance level of insulation. It is therefore important to consider the maximum electric field intensity and its duration in evaluating the electric life of a cable termination. Furthermore, this justifies the need to include transient electric stresses into the existing electro-thermal reliability model as Bahder et al [32] highlight the inverse relationship between frequency of applied stress and time to breakdown. Impulse stresses therefore substantially affect the life of insulation. A measure of the rate of life lost by electric degradation is represented by the electric stress life factor.

An important characteristic parameter in evaluating the electric stress life of cable systems is the electric threshold strength of the insulation. Cacciari et al [33] define the electric threshold as a limit of degradation, where mathematically if a stress below the threshold is applied the insulation has an infinite life because the aging process is infinitesimally small. Manufacturers

of cables usually give a maximum electric field stress which is below the threshold electric stress of the main insulation to ensure that the cable lives beyond its designed life span. The Inverse Power Law presented in *Section 2.3*, includes the maximum design electric field stress which gives the threshold of the degradation process. The steady state stress factor is presented in the following section.

#### 4.2.1 The Steady State Electric Stress Factor ( $\alpha_{sse}$ )

Under steady state operating conditions, the peak voltage induces the highest electric field stress in the termination. Cavallini et al [31] have shown that the peak voltage is the prevailing factor in the aging phenomena of XLPE insulation. *Figure 4.3* shows the statistical distribution of the RMS voltage during one year of operation obtained from the online data logging system at the substation under study [34].

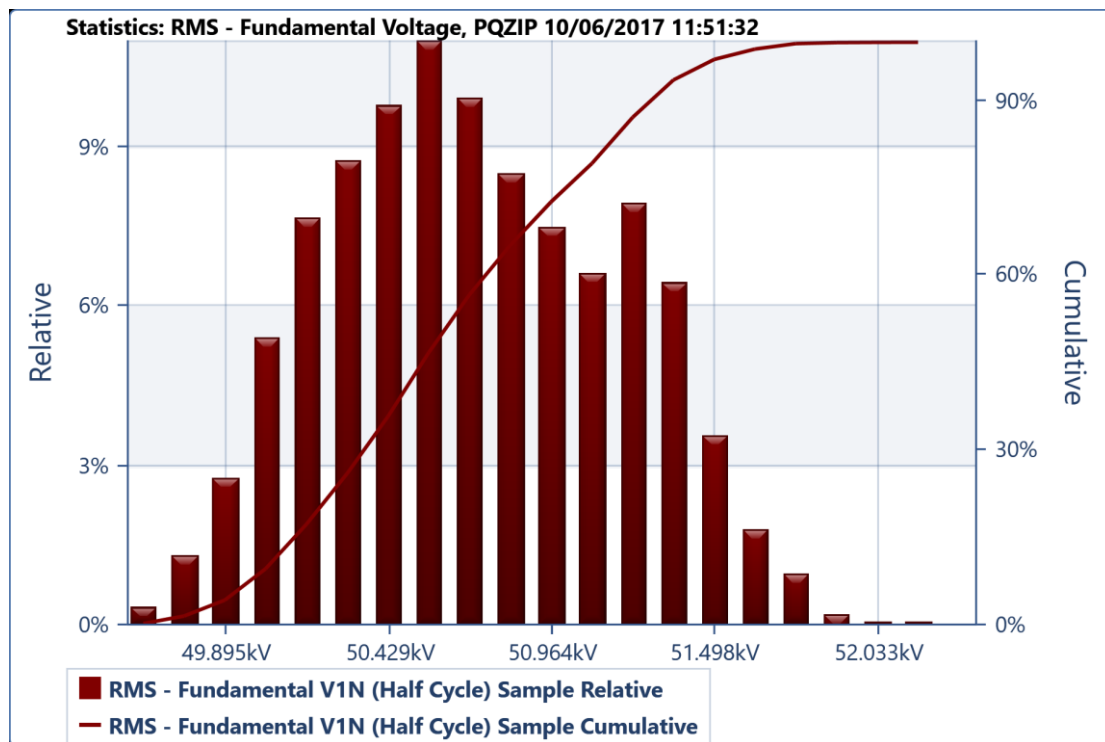


Figure 4.3. Statistical distribution of RMS voltage over one year (Data logged by online monitoring system)

Although the maximum peak voltage of 73.6 kV only occurs for 10 % of the time, it is selected for use in this case study as the worst-case estimate since it induces the highest steady state

stress. In the literature the electric voltage endurance coefficient ( $n_e$ ) of XLPE is reported as ranging from 9 to 20 [35]. However, in the present case study the mode value of the voltage endurance coefficient of 10 [35] is used.

The voltage endurance coefficient is a parameter of the material property which is obtained from experimental tests where the time it takes for insulation to break down is plotted against the applied electric field stress [36]. The inverse gradient of applied stress versus time to failure gives the endurance coefficient of an electric insulation. Simoni [37] modelled the endurance coefficient as a parameter that is dependent on the synergistic effects of sustained thermal and electrical stress as shown in *Equation 4.6* below.

$$n = n_e - s \cdot (1/T_o - 1/T) \quad (4.6)$$

Where  $n_e$  is the electric voltage endurance of XLPE,  $s$  is the synergism factor,  $T_o$  is the maximum design temperature of 90 °C and  $T$  is the maximum insulation temperature. The endurance coefficient in DC systems tends to vary more than that in AC cable systems [35].

Due to a small difference between the maximum design operating temperature of XLPE ( $T_o = 90$  °C) and the actual maximum XLPE temperature ( $T = 90.74$  °C), the synergistic steady state voltage endurance coefficient ( $n$ ) computed using *Equation 4.6*, is approximately equal to the electric voltage endurance coefficient ( $n_e$ ).

A FEMM simulation in *Figure 4.4* shows the peak steady state electric stress in the termination at maximum peak operating voltage. The location of high electric field stress is at the semiconductor to insulation interface located below the sheath end level. A peak voltage of 73.6 kV induces a stress of  $E = 5.4$  kV/mm. This stress value is below the design stress of  $E_o = 6.8$  kV/mm, therefore the stress factor due to steady state electric stress is 11.0. A steady state electric stress factor greater than one means there is a more than 100 % likelihood of the cable termination exceeding the design life of 40 years if electric stress is the only degrading stress.

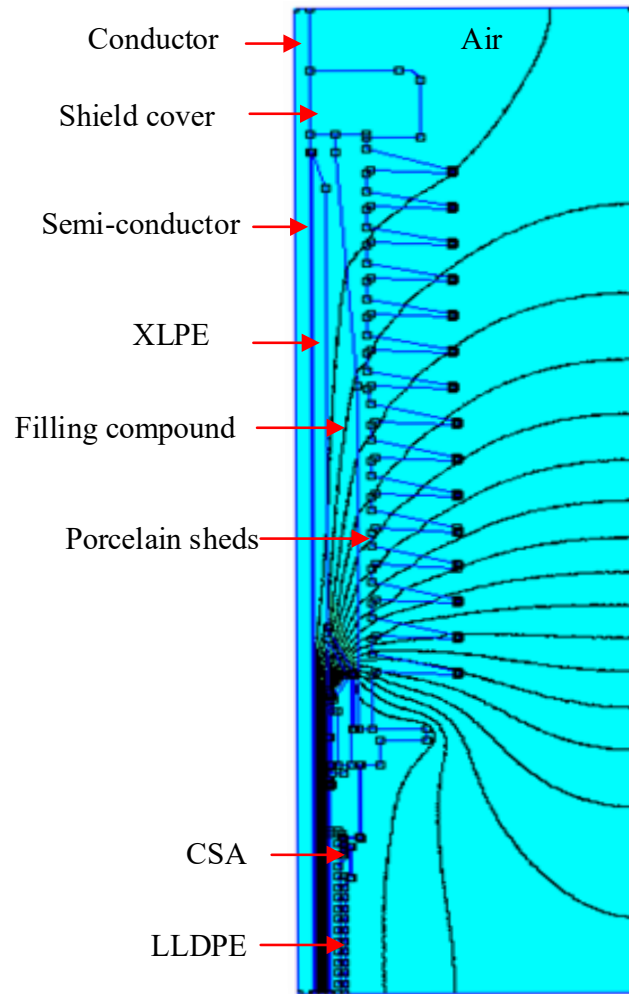


Figure 4.4. Electric field distribution inside the cable termination at maximum peak steady state voltage 73.6 kV.

The steady state electric stress factor is computed using the inverse power law as shown in Equation 4.7.

$$\text{Existing model: } \alpha_{sse} = \left( \frac{E}{E_0} \right)^{-n_e} \quad (4.7)$$

In the power cable system, both transient and steady state electric stresses are experienced. Similar to the steady state electric stress factor, there has to be a corresponding impulse electric stress factor. The existing electric stress model by Mazzanti can therefore be modified to include the effect of impulse stresses as demonstrated by Montanari et al [38] and is explained in more detail in the next chapter.

## 4.2.2 The Impulse Electric Stress Factor ( $\alpha_{imp}$ )

Montanari et al [38] demonstrated how the effect of impulse stresses can be included in the prediction of remaining life. In the model by Montanari et al the Inverse Power Law was adopted where the ratio of the peak impulse stress to the design Basic Insulation Level (BIL) stress of the cable system as well as the frequency (occurrences) of the impulses, determine the impulse electric stress factor.

The recorded peak and mode switching transient of 90 kV (shown in *Figure 4.3*) is used to compute the electric impulse stress factor, which is as an extension to the parameters used in the existing model. Under impulse stress it is expected that the endurance capability of the XLPE insulation is much lower [39] [40]. Furthermore the endurance of cable accessories is expected to be much lower than that of the cable itself [1]. In this case study the impulse endurance coefficient of 7 is used which is obtained from an existing reliability model in the literature [1]. *Equation 4.8* is used to compute the impulse electric stress factor.

$$\text{Extension to existing model: } \alpha_{sse} = \left( \frac{E_i}{E_{i0}} \right)^{-n_i} \cdot \frac{f_0}{f} \quad (4.8)$$

Where  $E_i$  is the maximum impulse electric field stress due to peak switching voltage,  $E_{i0}$  is the BIL (Basic Insulation Level) impulse stress factor obtained from the BIL voltage of 325 kV for a 88 kV system [7] and  $n_i$  is the impulse voltage endurance coefficient. The peak switching voltage recorded by the online data logging system is 90 kV as shown in *Figure 4.5*.

With the knowledge of both steady state and impulse electric stress factors, the overall electric stress factor can be determined as presented in the next section.

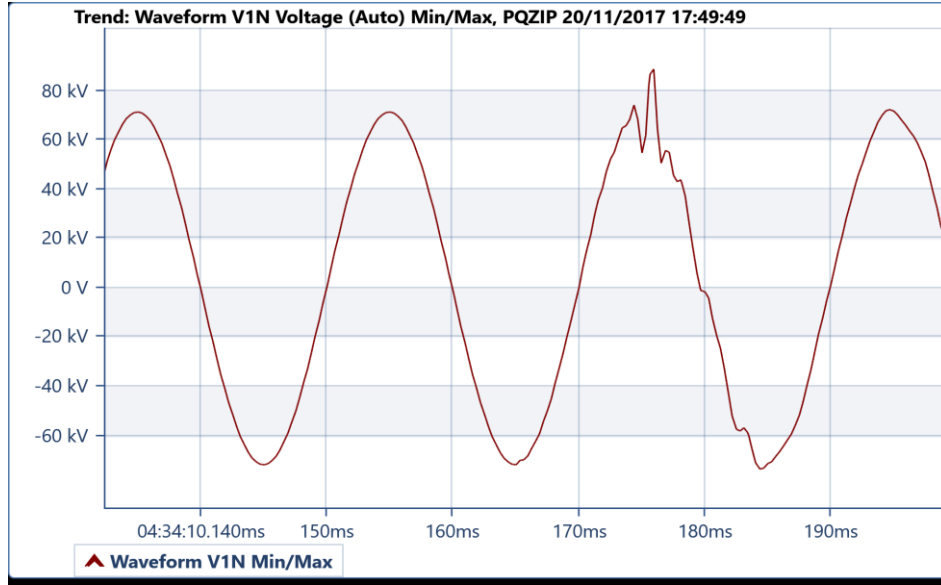


Figure 4.5. Recorded switching transient

### 4.2.3 Electric stress factor $\alpha(E, E_i)$

The overall electric stress is a combination of steady state electric stress and impulse electric stress as expressed in *Equation 4.9*.

$$\alpha(E, E_i) = \alpha_{sse} \cdot \alpha_{imp} \quad (4.9)$$

Where  $\alpha(E, E_i)$  is the 63.2<sup>th</sup> percentile probability of failure due to maximum continuous power frequency electric stress and impulse electric stress,  $\alpha_{sse}$  is the steady state electric stress factor and  $\alpha_{imp}$  is the impulse electric stress factor. By substituting the various constituent components of  $\alpha_{sse}$  and  $\alpha_{imp}$  the stress factor expression changes to that in *Equation 4.10*.

$$\alpha(E, E_i) = \left[ \left( \frac{E}{E_o} \right)^{-n_e} \cdot \left( \frac{E_i}{E_{io}} \right)^{-n_i} \cdot \frac{f_0}{f_i} \right] \quad (4.10)$$

Where  $\alpha_t(E, E_i)$  is the electric stress factor. The maximum impulse stress  $E_i$ , maximum continuous design electric field stress is  $E_o$ ,  $E_{io}$  is the design impulse electric field stress obtained from the BIL,  $f_0$  is the 50 Hz power frequency,  $f$  is the number of switching events per period,  $n_e$  is the voltage endurance due to the synergy of both electric and thermal stress in XLPE insulation.

The resultant parameters used in computing the electric stress factor are listed in *Table 4.3*. In the last row of the table the resultant stress factor value of  $2.23 \times 10^{11}$  is presented.

Table 4.3. Electric stress model life parameters

Description	Symbol	Value
Maximum continuous stress (Obtained through FEMM simulations at maximum operating peak voltage)	$E$	5.35 kV/mm
Design stress (76/132 kV XLPE Al core CSA cable)	$E_o$	6.8 kV/mm
Maximum impulse stress (Switching impulse stress at maximum switching voltage as recorded by data logging system (See figure 4) *switching has been used because there were no direct lightning strikes observed in one year's operating data*)	$E_i$	6.85 kV/mm
BIL stress ( Derived from the BIL of 325 kV for 88 kV system [41],[42])	$E_{io}$	24.73 kV/mm
Impulse voltage endurance coefficient [1], [12]	$n_i$	7
Steady state voltage endurance coefficient [1], [38] ,[35]	$n$	10
Power frequency	$f_o$	50 Hz
Frequency of impulses (impulse count obtained from the data measurement system)	$f_i$	$2.13 \times 10^{-5}$ Hz
<b>Electric stress life factor (obtained using Equation 4.10)</b>	<b><math>\alpha(E,E_i)</math></b>	<b><math>2.23 \times 10^{11}</math></b>

At a steady state operating voltage without any lightning impulses and only up to 56 switching incidents per month the electric stress alone is not adequate to introduce considerable life reduction with time. *Figure 14* shows that the average reliability under switching transient only reaches the 50 % mark when the magnitude of the induced stress is 105.5 kV/mm. In GIS substations, VFT (Very Fast Transients) that are caused by the switchgear operations may introduce high resultant stress conditions especially due to the travelling wave voltage reflection phenomena [43]. In this regard the effect of high electric field stresses on the reliability of the cable terminations is presented in *Figure 4.6*.

As reported earlier in section 3.2 there was no evidence of lightning impulses recorded by the online data logging system. The likelihood however of a lightning strike in the lifetime of the terminations cannot be dismissed, particularly in the absence of the ground connection on the

surge arrestors. Furthermore VFT (Very Fast Transients) during switching may result in a much higher switching electric field stress and therefore the intermittent presence of SVL at the GIS

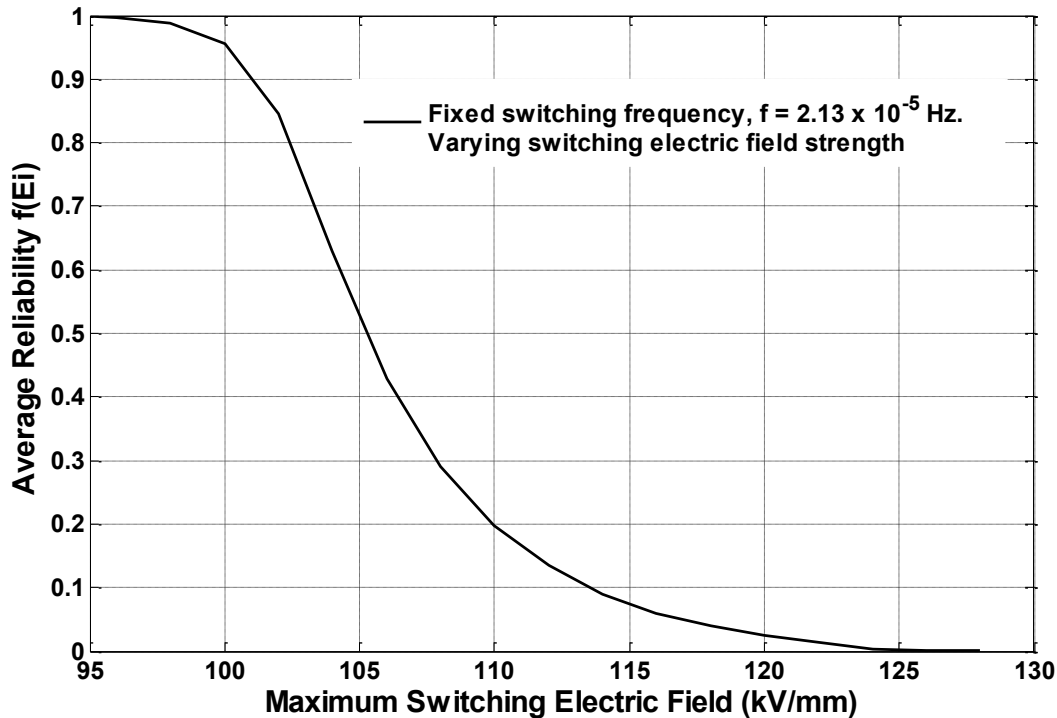


Figure 4.6. Effect of varying switching electric field strength and impulse count on reliability for terminations in the case study substation after 29 years in operation.

can result in higher induced sheath voltage. The effect of such system irregularities is discussed in the next section.

#### 4.2.4 Effect of System Irregularities on the Electrical Life of the Termination

In the literature there is evidence that a high number of lightning impulses and switching voltages on cable terminations will result in a drastic reduction of the insulation condition [30], [44]. In the case study, the absence of a ground connection on the line arrestors increases the risk of exposing the terminations to accelerated aging under impulse stresses. The effects of lightning impulses in the absence of a grounded line arrester therefore are necessary to investigate.

ATPDraw™ is used to calculate the surge voltage at the termination due to lightning terminating within 2 km of the case study substation (See *Appendix A.1*). In the absence of a grounded station surge arrester a 13.6 MV peak surge will induce an electric field of up to 1035

kV/mm as shown by the FEMM results in *Figure 4.8* while the presence of surge arrester results in a induced peak electric stress of 24.9 kV/mm. It is therefore likely that if a lightning strike occurs in the absence of a ground connection on the surge arrestors the terminations will fail. The simulated lightning surge is shown in *Figure 4.7*.

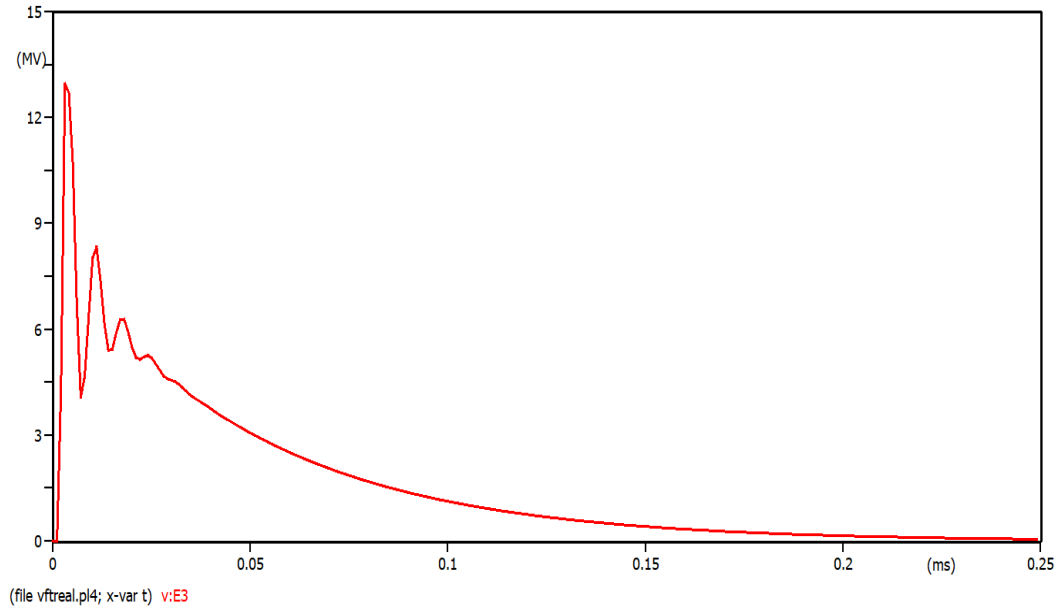


*Figure 4.7. Lightning surge at the termination.*

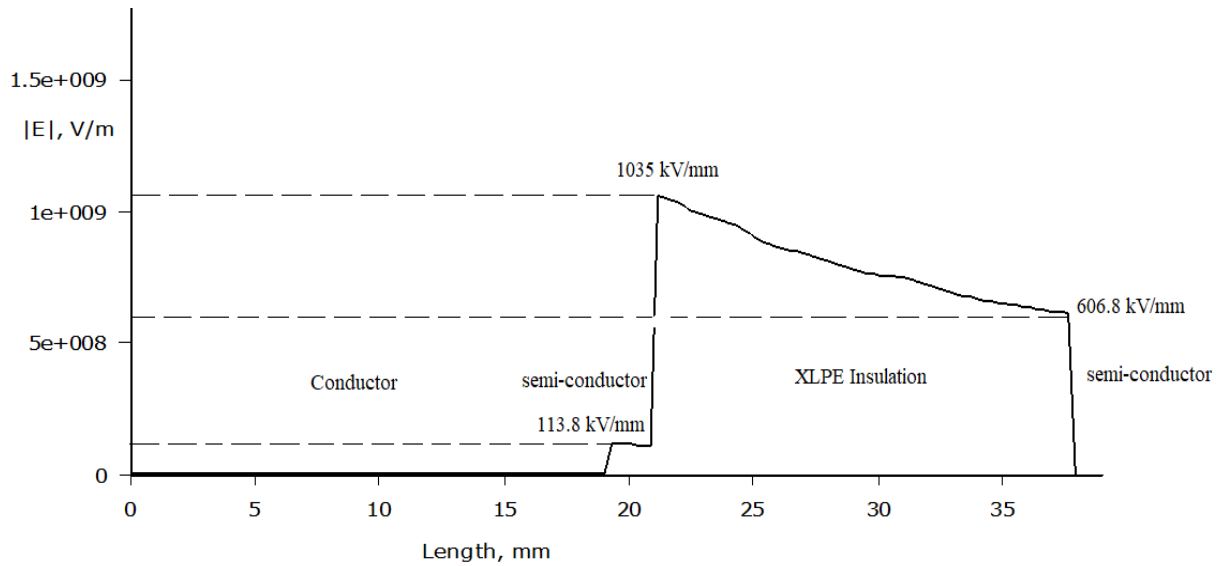


*Figure 4.8 Electric field distribution in the termination during lightning impulse in the absence of grounded surge arrester*

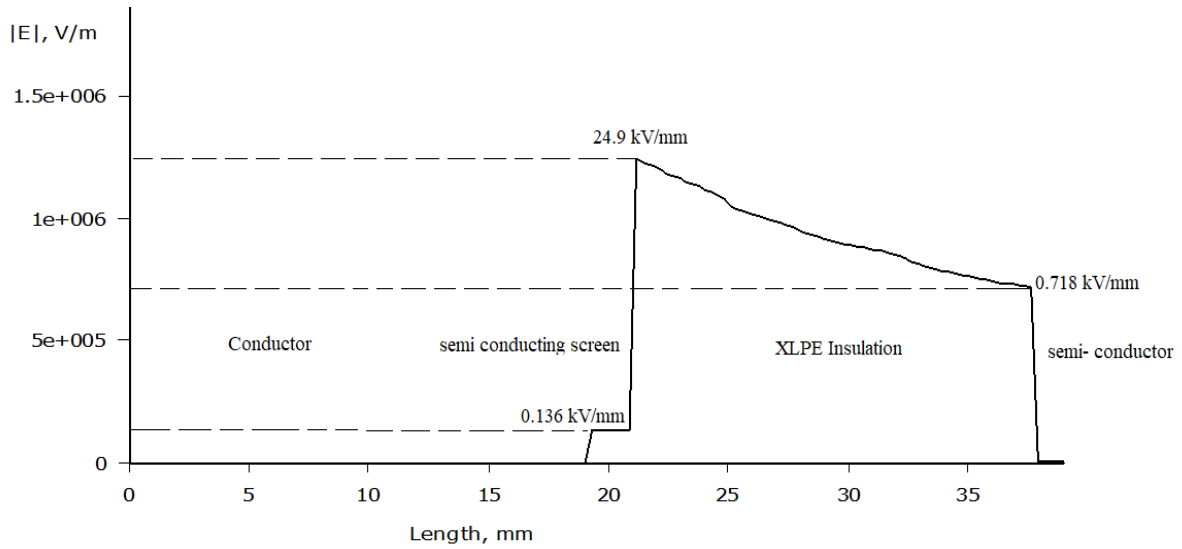


Figure 4.9. Electric field distribution in the termination during lightning impulse in the presence of grounded surge arrester

The presence of overhead lines with shield conductors in the substation protect the cable terminations from direct lightning strikes. Substation lightning self-protection occurs when the number of lines connected to the substation exceeds the fundamental requirement stated in the Insulation Co-ordination Standard IEC 60071-2 [41] shown in Equation 4.11.

$$n \geq 4[(U_{50}^-/U)] - 1 \quad (4.11)$$

Where  $n$  is the number of overhead lines,  $U_{50}^-$  is the 50% lightning impulse flashover voltage of the line insulation and  $U$  is the maximum lightning overvoltage amplitude caused by reflecting voltage waveforms. When the lightning strike point along the line exceeds a distance computed in Equation 4.12, there is substantial corona damping on the line such that the surge steepness and magnitude are reduced [75].

$$X_p \geq 4(T/K_{co}U) \quad (4.12)$$

Where  $X_p$  is the strike point limit distance from the substation,  $T$  is the time travelled to the limit distance and  $K_{co}$  is the corona damping constant of  $1.5 \times 10^{-6} \mu\text{s}/(\text{kV m})$  [11]. In the given case study, a lightning surge of 13.6 MV (Simulated in ATPDraw shown in Figure 4.7) that occurs less than 342 m away from the cable terminations will not have substantial damping to reduce the impact of the surge on the cable terminations in the absence of a grounded surge arrester. Therefore, the cable terminations have a high likelihood of failure in the event a direct lightning strike occurring on the terminations or on the line within a 2 km radius.

In a properly grounded cable system, the SVL (sheath voltage limiter) ensures the sheath voltage is low at the GIS side of the cable. When however, the SVL at the GIS side of the cable is faulty there is a higher induced sheath voltage at the termination end. Furthermore, when the metallic interfaces in the cable termination fail due to corrosion or thermo-mechanic fatigue the fault current ground path is disrupted and the single point bonding of the cable system becomes open circuited.

In the case study data, the maximum recorded fault current was up to 10 kA as shown in *Figure 4.10*, while the corresponding conductor voltage dropped as shown in *Figure 4.11*. The compromised ground connection on the cable termination together with a non-grounded station surge arrester and SVL (due to cable theft) result in a relatively high sheath voltage.

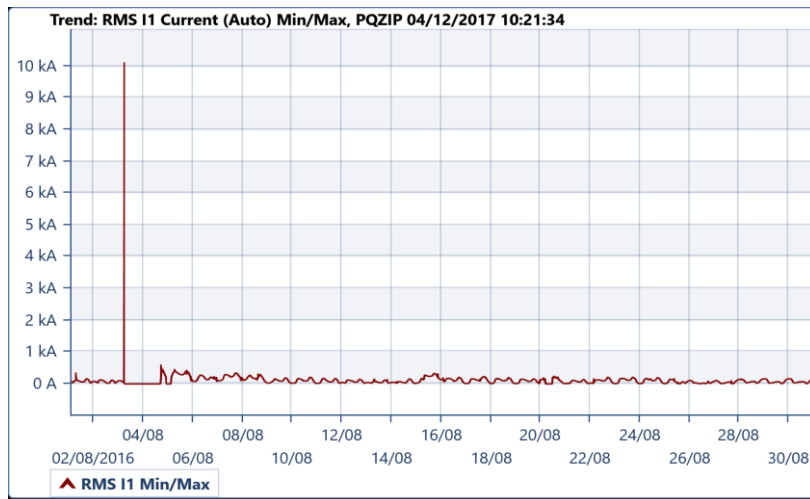


*Figure 4.10. Maximum recorded ground-to-earth fault current*

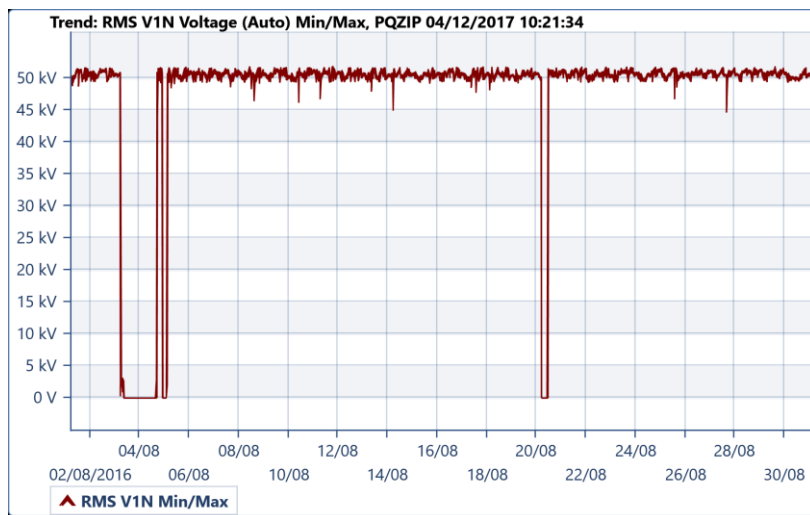


*Figure 4.11. Phase-to-ground fault voltage*

For a fault current of 10 kA the sheath voltage is calculated using *Equation 4.13* to increase to 15.6 kV instead of the design allowable level of 6-7 kV [12].

$$E_{sh} = 107 \cdot \left(\frac{S}{d}\right)^{0.369} \cdot l_c \cdot I_c \quad (4.13)$$

Where  $E_{sh}$  is the maximum induced sheath voltage at the non-grounded end.  $S$  is the centre to-centre cable spacing of 36.12 cm,  $d$  is the mean sheath diameter 98 mm,  $l_c$  is the cable length of 100 m and  $I_c$  is the conductor current. The changes in the sheath voltage in the presence and absence of SVL are illustrated in *Figure 4.12* (a) and (b) respectively.

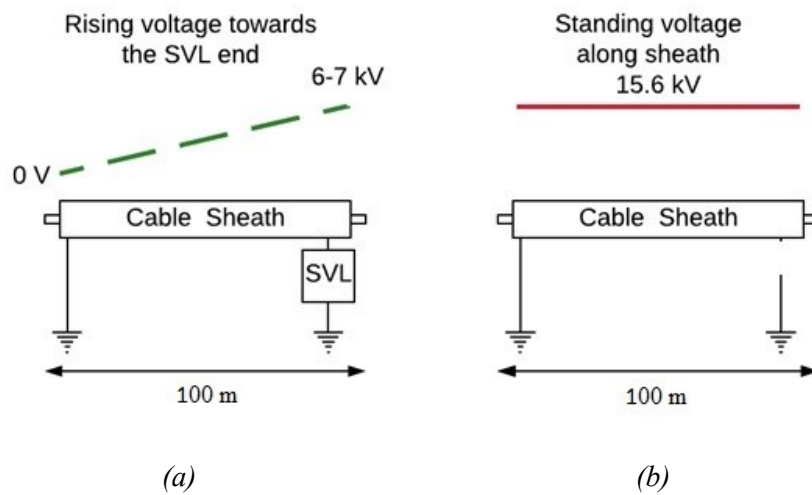


*Figure 4.12. Sheath voltage at maximum fault current (a) Sheath voltage when there is single point bonding (SVL is functional and copper braid is grounded at termination end). (b) Sheath voltage when termination end is not grounded and SVL is not functional*

### 4.3 The Thermal Degradation Mode

Current flow generates heat in the cables. The threshold condition for thermal degradation to occur is when the rate of heating far exceeds the rate of cooling. The charge flow of electrons in insulation is due to electron, ionic migration and the slow movement of dipoles [46]. The movement of the charge electrons results in hot spots and avalanches. When electrons collide with other molecules there is an increase in leakage current thus further sustaining thermal hotspots. By-products such as CO<sub>2</sub>, H<sub>2</sub>, CH<sub>4</sub> and other combinations of hydrocarbons further aid the thermal degradation process [46], [47]. At a specific critical electric field stress the insulation dipole alignment becomes irreversible resulting in permanent damage to the insulation [46]. *Equation 4.14* shows how the critical electric field strength for thermal

degradation is evaluated according to Kuffel et al [46]. This further confirms the synergism of thermal and electric degradation in insulation.

$$E_c = \left[ \frac{3C_v k T_0^2}{\sigma_0 u t_c} \right]^2 \exp\left(\frac{u}{2kT_0}\right) \quad (4.14) [46]$$

Where  $C_v$  is the thermal capacity of the insulation,  $\sigma_0$  is conductivity,  $k$  is thermal conductivity,  $t_c$  is the critical time,  $T_0$  is the ambient temperature and  $x$  is the surface length in the direction of heat flow.

The conductivity of the material is a function of the permittivity, where the permittivity varies with frequency. Therefore critical electric field intensity for thermal degradation to occur is a function of the critical time, and nature of the applied voltage [46]. According to Ross [48], thermal degradation of a material is dependent on the time constant of the applied voltage and the materials thermal capacity.

Various models have been used to quantify the remaining life under thermal degradation. Bessissa et al [49] used arithmetic sequences of cable tensile strength variation with temperature changes to estimate life. The arithmetic sequences are optimised by genetic algorithms This method relies on a comprehensive database where the tensile strength ranges are grouped and each group has a recommended maintenance decision [49]. The accuracy of this method is dependent on the database size and the algorithms. The method relies on the initial decisions made by the maintenance engineer. Another model that has been used to model the life under thermal stress is the Eyring model as presented in the next section.

### 4.3.1 The Eyring Model

Eyring model can be used to characterise thermal life of cable systems. Its first application was in quantum mechanics and is not commonly used to model thermal life in high voltage systems [11]. *Equation 4.15* shows the Eyring model

$$m = \frac{1}{T} \exp\{-[A - (B/T)]\} \quad (4.15)$$

Where  $m$  is the mean life,  $A$  and  $B$  are constant properties of the material and  $T$  is the temperature.

Although the Eyring model is valid for cable systems, it has not been often used as it does not use the design maximum temperature as a reference of quantifying the extent of degradation

with time. In the existing model by Mazzanti and Mazzinto [1], the Arrhenius law (See *Section 2.4*) is applied using the maximum possible temperature of the cable systems main insulation. Thermal life models that use the transient temperature due to load cycles are considered to give a more accurate projection of thermal life. These models demonstrated by Mazzanti [50]–[53] compute the thermal life of cable insulation under varying load cycles by using the cumulative damage law of Miner. In the present work a similar approach is used in thermal modelling.

### 4.3.2 The Miners Law

In Miners law the overall life is equal to the sum of life fractions lost with each load current step in the cable. Miners cumulative damage law is shown in *Equation 4.16* [10].

$$\sum_{i=1}^k \frac{n_i}{N_i} = C \quad (4.16)$$

Where  $n_i$  is the number of cycles accumulated at a specific stress,  $k$  is the number of different stress levels,  $N_i$  is the average number of cycles to failure and  $C$  is the total fraction of life which is equal to 1.

The drawback with Miners rule is that it assumes a linear relationship between stress and life and does not consider the probabilistic properties of stress. Furthermore, the degradation mechanism is not considered. To get a more accurate estimate of life under thermal stress, Miners law and the Arrhenius life law are combined. If a fraction of life is lost at each current step the transient temperatures due to load cycling is presented in the next subsection.

### 4.3.3 Transient Temperatures: Cigre Two Loop Network and Fourier Heat

#### Equation

To characterize the thermal stresses in the termination, load cycle profiles and general location temperatures are required as per Arrhenius Law. Due to the direct relationship between load current and temperature [50], the highest load variations are required to compute the thermal life factor. The load cycle profiles retrieved from the online data logging system show that in winter there is more current drawn due to increased demand. The typical annual average temperature changes on site (shown in *Figure 4.13*) during the winter season are compiled to obtain step-wise temperature changes in the critical layers of the cable termination using the Cigre Two Loop Network and Fourier's heat equation [54].

Operating load profiles over a year at the case study substation show that the worst load cycle profile occurs in winter as shown in *Figure 4.14*.

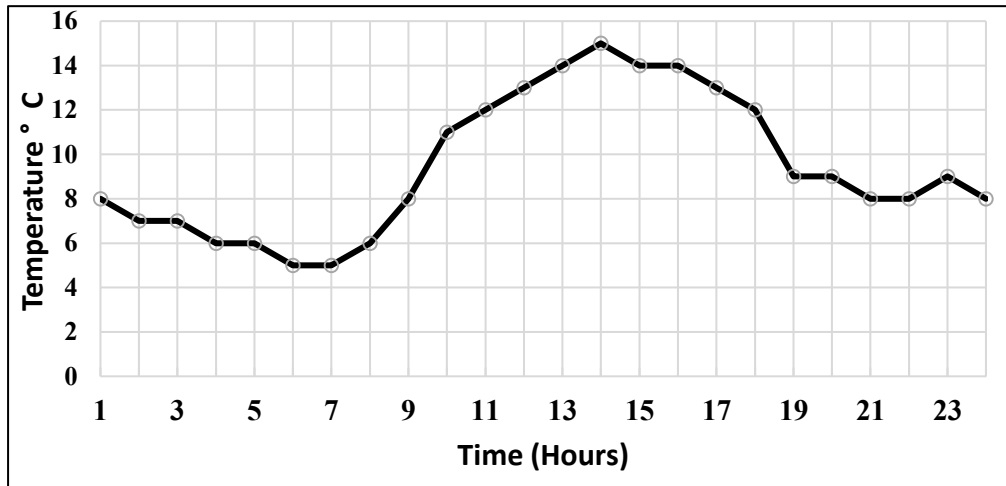


*Figure 4.13. Average daily winter temperatures*

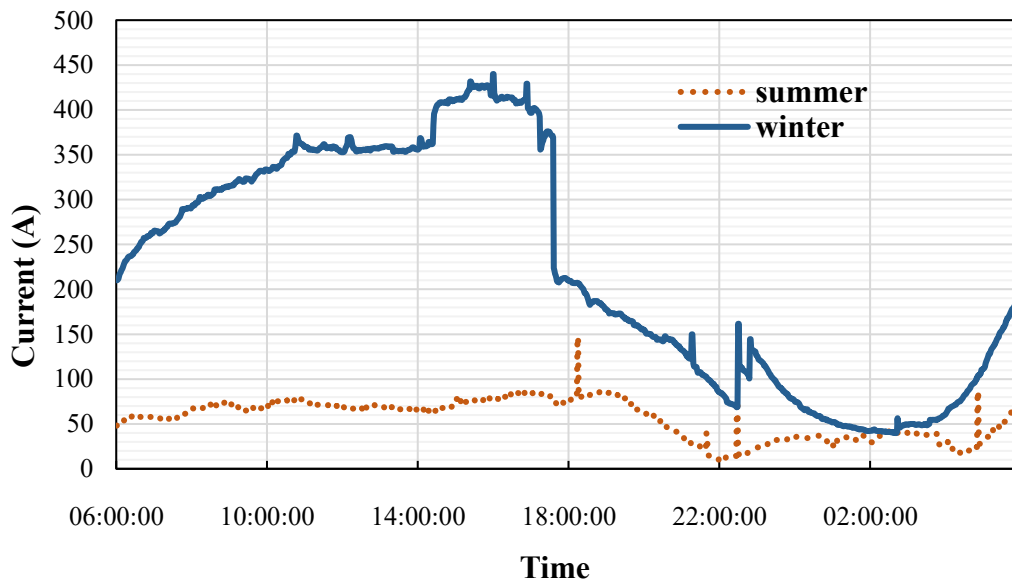


*Figure 4.14. Typical daily seasonal load cycle extracted from one year's operation data*

The transient temperatures at current step intervals on a selected day at the case study substation is computed using the Cigre two loop network method and Fourier's heat equation as shown in *Equations 4.17* and *4.18*.

$$T_{ci} = W_d [T_a(1 - e^{-at}) + T_b(1 - e^{-bt})] + \frac{T_a(1 - e^{-at}) + T_b(1 - e^{-bt})}{T_a + T_b} \cdot T_{Ei} \quad (4.17)$$

Where  $T_{ci}$  is the conductor temperature change above the surface temperature of the cable due to each current step change.  $W_d$  is the heat losses,  $T_a$  and  $T_b$  are the thermal resistances of the cable,  $a$  and  $b$  are the time constants of the first and second thermal network respectively and  $T_{Ei}$  is the hourly environmental daily average temperature during the winter season.

Assuming one directional heat flow, isotropic heat flow and a constant thermal conductivity for each material in the termination, the transient temperature changes in the XLPE insulation and subsequent layers of the cable were computed using the Fourier heat equation [55] shown in Equation 4.18. The thermal conductance, thickness as well as the distance away from the conductor heat source determines the temperature changes of each layer.

$$T_{n(i+1)} = T_{ni} + \frac{I^2 R \cdot \ln\left(\frac{r_{n(i+1)}}{r_i}\right)}{-K_i \cdot 2\pi L} \quad (4.18)$$

Where  $T_{n(i+1)}$  is the temperature change of layer  $n(i+1)^{th}$  due to the temperature change  $T_{ni}$  at the  $i^{th}$  layer,  $I$  is the cyclic load current,  $R$  is the conductor resistance,  $K_i$  is the thermal conductance,  $L$  is the cable length,  $r_{i+1}$  and  $r_i$  are the thicknesses of the interfacing layers. The simulated temperatures in the cable are shown in Figure 4.15.

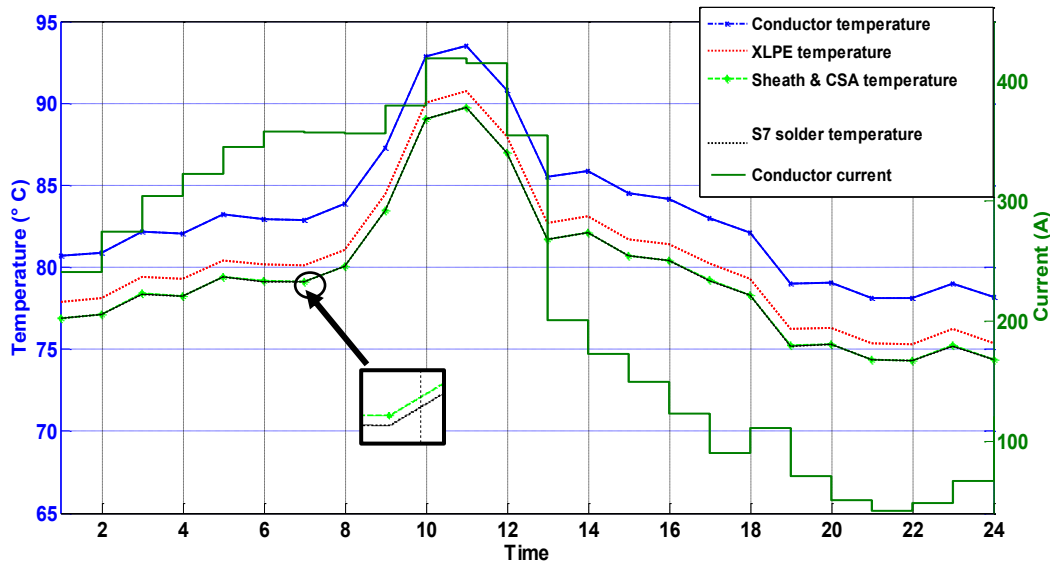


Figure 4.15. Temperature changes with worst case load current profile trend.

The cumulative degradation of XLPE insulation can be modelled using the worst-case daily temperature changes due to load cycles. The parameter used to quantify the extent to which thermal stress degrades XLPE insulation is the thermal stress life factor which is presented in the following subsection.

#### 4.3.4 Thermal stress factor $\alpha(t, T)$

The thermal life factor of the cable is computed using *Equations 4.19* and *4.20*. The computation uses Miners cumulative damage law [10], temperature transients calculated using the Two Loop Network and Fourier's Heat Equation as well as Arrhenius law of degradation.

$$\alpha_i(t, T) = \int_0^{\Delta t_i} \frac{dt}{\alpha(T_i(t))} \quad (4.19)$$

$$\alpha(t, T_i) = \sum_{i=1}^N \left\{ \int_0^{\Delta t_i} \frac{dt}{\exp\left(\frac{\Delta W}{k_B}\right) \cdot (1/T_o - 1/T_i)} \right\} \quad (4.20)$$

Where  $\alpha_i(t, T)$  is the thermal life factor as a function of temperature and time,  $T_i(t)$  is  $i^{th}$  transient temperature at time  $t$  which is computed in *Equation 4.18*. The thermal activation energy of XLPE is  $\Delta W$ ,  $k_B$  is Boltzmann's constant,  $\Delta t_i$  is the  $i^{th}$  time step and  $T_o$  is the maximum design temperature of the cable termination. This approach in obtaining a thermal reliability model is supported by various standards that include; IEEE 48-2009 and IEC 60853 [56].

The various parameter values determined in compiling the thermal life factor in the present case study are presented in *Table 4.5*. The resultant thermal life factor of 3.71 is in the last row of the table.

*Table 4.5. Thermal life model parameters for the case under study*

Description	Symbol	Value
XLPE thermal degradation activation energy [1] (Obtained from the termination ratio of activation energy to Boltzmann constant of 12937 by Mazzanti et al [1])	$\Delta W$	$1.7034 \times 10^{-19} \text{ J}$
Boltzmann's constant	$k_B$	$1.381 \times 10^{-23} \text{ J.K}^{-1}$
Maximum operating temperature	$T_o$	93.53 °C
Step operating temperatures	$T_i$	*See <i>Figure 4.15</i>
Temperature steps (Hourly)	$N$	24
Hourly average winter temperatures in degrees Celsius	$T_{Ei}$	8,7,7,6,6,5,5,6,8,11,12,13,14,15,14,14,13,12,9,9,8,8,9,8
<b>Thermal stress life factor (Calculated using <i>Equation 4.20</i>)</b>	<b><math>\alpha(t, T_i)</math></b>	<b>3.71</b>

In the Arrhenius model the maximum XLPE insulation temperature determines the rate of degradation with time. A maximum insulation temperature of 90.74 °C which is within the design temperature of 90 °C results in a life factor that is greater than one ( $\alpha(t, T_i) = 3.71$ ). This life factor depicts a high likelihood of the terminations exceeding their design life span under steady state thermal stresses. To obtain a more accurate transient temperature profile, a one hour current step period was used in comparison to the two hour step used by Mazzanti et al [50]. Typically, the earth to ground surge currents are below the design symmetrical fault rating of 92.5 kA (1s) and earth fault rating of 58.2 kA (1s) [57] when the line surge arrester is grounded. In this case study, fault current surges may take an altered high impedance path to ground and cause up to 800 kW heat which causes accelerated thermal degradation of the semi-conductor and XLPE insulation [20]. Since material aging due to thermal stress occurs in synergy with electrical stress induced aging the resultant reliability becomes an electro-thermal function as presented in the next section.

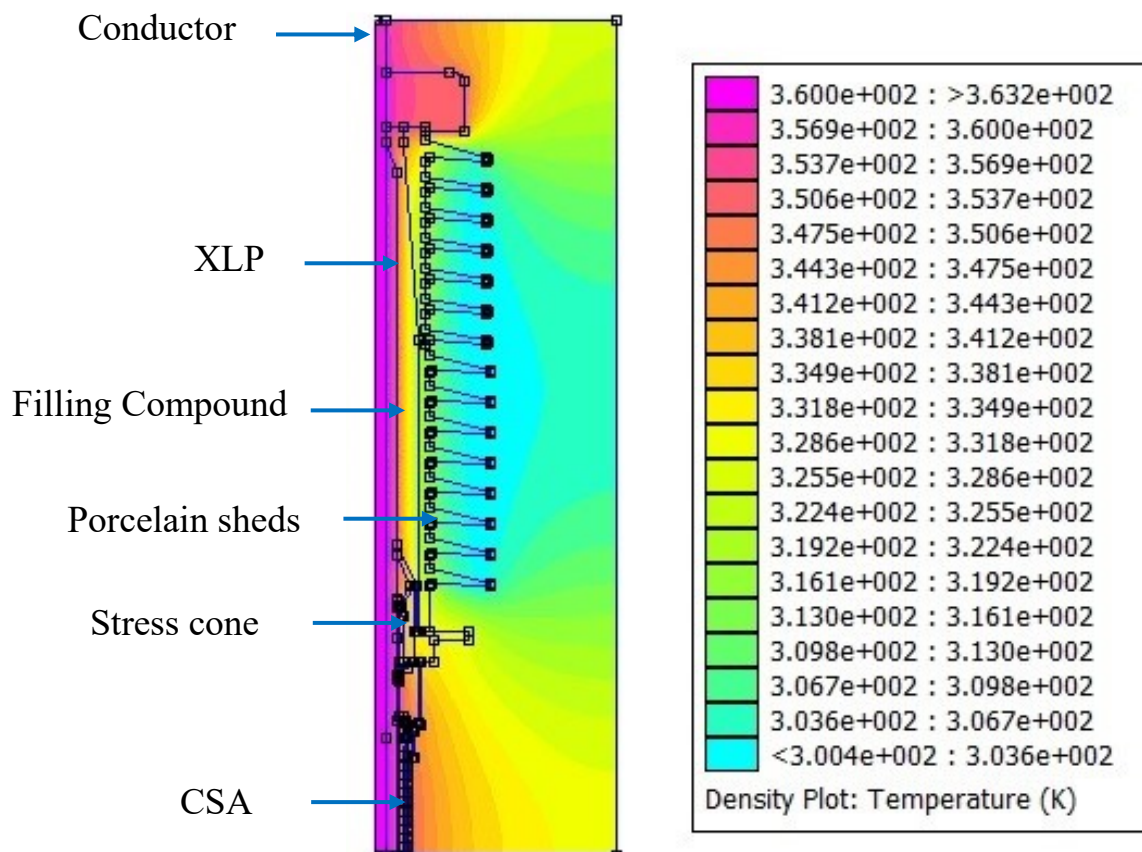
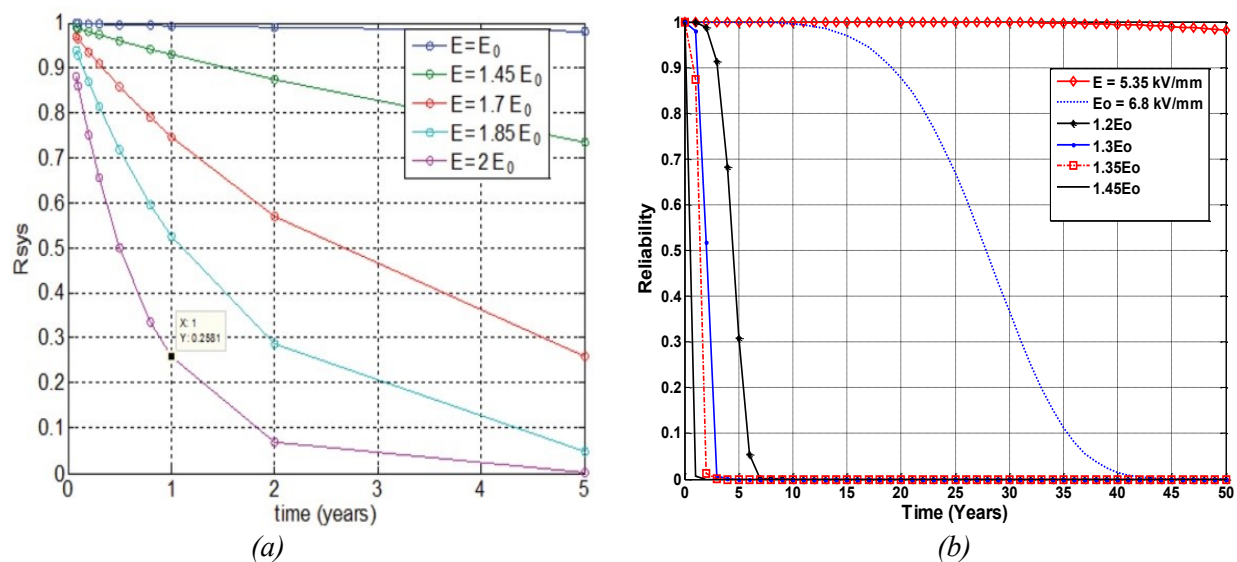


Figure 4.16. Temperature inside the termination at earth fault current

#### 4.4 The Electrothermal Reliability $R(E, T)$

Due to the synergistic relationship between the electric and thermal degradations the effect of the two failure modes can be combined. For comparison with similar results in the literature, the electrothermal life factor without the impulse stress component at the recorded maximum peak steady state voltage stress of 5.35 kV/mm is calculated as  $\alpha(E, T) = 40.82$  being the product of steady state electric stress life factor ( $\alpha_{sse}$ ) with the thermal life factor  $\alpha(t, T)$ . The thermo-electric life factor decreases with increase in steady state stress factor as shown in the resultant plots of electrothermal reliabilities presented in *Figure 4.17 (b)*. The plots compare reasonably well with those in literature shown in *Figure 4.17 (a)* from similar work by Mazzanti et al [1].



*Figure 4.17.(a) Existing electrothermal reliability ( $R_{sys}$ ) model for an HVDC 150 m cable system without joints (reproduced with permission from Mazzanti [1]) (b) Steady state electrothermal reliability of the case study cable*

The two models depict comparable trends showing reduced reliabilities with time at higher electric field stresses. The specific values are however different since the rate of life lost is a function of site and system specific conditions as manifested in the Weibull shape and scale parameters.

In the present case study, at a steady state operating electric field stress of 5.35 kV/mm and in the absence of switching and lightning surges, the electric stress factor is 11.00 which gives an electrothermal reliability of above 90% after 29 years and that would not be a major cause for concern. This shows that electrothermal degradation on its own is not the dominant degradation

stress within the termination and there are no installation or manufacturing defects. The model also shows that if maximum continuous electric field stress is increased beyond the design stress of 6.8 kV/mm, the lifespan reduces to below 40 years.

In the investigated cable termination, another identified degradation mechanism is of thermo-mechanic nature as presented in the next section.

## 4.5 Thermomechanic Fatigue and Fracture Mechanism Model

Fatigue is a material condition caused by localized concentrated progressive strain due to thermal mechanic cycles in metals which form fracture cracks [20], [59]. The simultaneous presence of plastic strain, cyclic and tensile stress is necessary to facilitate fatigue failure [60]. When a material is subjected to a tensile stress that exceeds its yield limit, small slip lines begin to form which gradually develop into micro-cracks. Plastic deformation is the first stage of fatigue failure followed by the formation of micro-cracks. Micro-cracks develop into macro-cracks until they are big enough to cause total failure [61].

It is inevitable that the metallic interfaces within the cable termination gradually degrade during its lifetime because of thermomechanic stresses caused by load cycles, fault currents, lightning or switching impulses and over voltages. Furthermore materials with differences such as relative thermal expansion and heat capacity are susceptible to fatigue after the designed number of life cycles is surpassed or if the extent of stress far exceeds its designed limit [62]. The fundamental law upon which the thermo-mechanic fatigue degradation can be modelled assuming uniaxial fatigue using the Coffin-Manson Model presented in the next subsection.

### 4.5.1 The Coffin-Manson Model for Fatigue Degradation

The Coffin-Manson's life strain model has been used to quantify the reliability of metal components under fatigue stress [63]. The relationship between the number of cycles to failure and strain amplitude is given in *Equation 4.21*.

$$\frac{\sigma_f'}{E} N^b + \epsilon_f' N^c = \epsilon_a \quad (4.21)$$

Where  $\sigma'_f$  is the fatigue strength coefficient, E is Young's modulus, N is the number of cycles to failure, b is fatigue strength exponent,  $\varepsilon'_f$  is the fatigue ductility coefficient, c is the fatigue ductility exponent and  $\varepsilon_a$  is the total strain amplitude.

Due to the probabilistic nature of stress and strain amplitude in most metallic systems the probability of failure can be computed as a function of the strain amplitude distribution. This likelihood of failure is computed below a set number of life cycles which is usually the design life cycles of the material. Bargmann et al [64] amongst other researches give a stochastic method of computing the probability of failure as given in *Equations 4.22 and 4.23*.

$$F_{\underline{N}}(N) = \int_{D_N}^{\infty} f_{\varepsilon_a \sigma'_f \varepsilon'_f}(\varepsilon_a, \sigma'_f, \varepsilon'_f) d\varepsilon_a d\sigma'_f d\varepsilon'_f \quad (4.22)$$

$$R(N) \equiv 1 - F_{\underline{N}}(N) \quad (4.23)$$

Where  $F_{\underline{N}}(N)$  is the probability of failure below a life value of N, The function  $f_{\varepsilon_a \sigma'_f \varepsilon'_f}(\varepsilon_a, \sigma'_f, \varepsilon'_f)$  is the probability density distribution due to strain  $\varepsilon_a$ , fatigue strength coefficient  $\sigma'_f$  and fatigue ductility coefficient  $\varepsilon'_f$  [64]. The reliability below N cycles is computed using *Equation 4.23*.

Coffin Mason's stochastic computation of reliability under thermo-mechanic fatigue is valid in conditions where the stress and strain can be measured. In the present case study, stress and strain occur where the S7 solder wiper a copper braid onto the copper bell housing. Measurement values of the stress and strain parameters on the interfacing metals are not readily available therefore the simple Coffin-Manson model cannot be applied in this research. However, a modified version of the Coffin-Manson model is presented in the next section for the case at hand.

#### 4.5.2 The Landzberg and Norris Model

In the absence of a stress or strain measurements the Coffin-Manson model can be modified to be dependent on the stress frequency and temperature range as implemented by Landzberg and Norris [24]. *Equation 4.24* shows the number of life cycles to fatigue crack initiation as a function of temperature cycles.

$$N = f^{-a} \cdot \Delta T^{-b} G(T_{max}) \quad (4.24)$$

Where  $N$  is the number of cycles to fail,  $a$  is a constant which is a function of material properties,  $f$  is the cycling frequency,  $a$  is the cycling exponent of 1/3.  $\Delta T$  is the approximate temperature change obtained from the thermal cyclic profile caused by load cycles,  $b$  is the temperature range exponent,  $G(T_{max})$  is Arrhenius term shown in *Equation 4.25* [65].

$$G(T_{max}) = \exp\left(\frac{A_E}{k_B} \cdot \frac{1}{T_{max}}\right) \quad (4.25)$$

Where  $A_E$  is the activation energy,  $k_B$  is the Boltzmann constant and  $T_{max}$  is the maximum temperature.

The Landzberg and Norris model gives an estimate number of cycles to failure without a reference point, it only looks at the worst-case scenarios and does not quantify them relative to the design conditions. The inclusion of baseline design parameters into the model allows the evaluation of remaining life as a function of the thermal mechanic fatigue stress as presented in the next section.

### 4.5.3 The Thermomechanic fatigue stress life factor, $\alpha(N)$

The life stress factor under thermo-mechanic degradation can be computed using a combination of Landzberg and Norris as well as Arrhenius and Coffin-Manson laws as shown in *Equation 4.26* [10].

$$\alpha(N) = \left(\frac{f_T}{f_{T0}}\right)^{-a} \cdot \left(\frac{\Delta T}{\Delta T_0}\right)^{-b} \cdot \exp\left(\frac{A_E}{k_B} \cdot (1/T_{max} - 1/T_{T0})\right) \quad (4.26)$$

Where  $N$  is the thermal mechanic fatigue life factor of the S7 solder. The ratio of operating temperature range,  $\Delta T$ , to the maximum design temperature range,  $\Delta T_0$ , as well as the ratio of design thermal frequency,  $f_{T0}$ , to operating thermal frequency,  $f_T$ , are critical in fatigue fracture. The Landzberg and Norris law combined with Coffin-Mansons law can be convenient in computing the life factor in the case study at hand since the parameters required for the computation can be determined from the properties of the termination as presented in *Table 4.6*.

Table 4.6. Thermo-mechanic parameters

Description	Symbol	Value
Design thermal cycle frequency (Based on the assumption that there are two thermal cycles per day)	$f_{T0}$	$2.314 \times 10^{-5}$ Hz
Thermal cycle frequency (Obtained from the thermal cycle frequency of Figure 5)	$f_T$	$1.157 \times 10^{-5}$ Hz
Solder operating temperature range (Obtained from Figure 5)	$\Delta T$	11.53 °C
S7 (35/65, Sn/Pb) temperature range [65]	$\Delta T_0$	223 °C
Temperature steps in a 24-hour day	$N$	24
S7 material constant [65], [66]	$a$	1/3
S7 material constant [65], [66]	$b$	1.9
S7 activation energy to reach fracture [66]	$A_E$	0.12 eV
Boltzmann constant	$k_B$	$8.617 \times 10^{-5}$ eV/K
Design maximum temperature [66] (Melting point of Sn35Pb65 solder)	$T_{T0}$	183 °C
S7 maximum operating temperature (Obtained from Figure 5)	$T_{max}$	89 °C
<b>Thermomechanic fatigue stress life factor (Calculated using Equation 4.26)</b>	<b><math>\alpha(N)</math></b>	<b>0.492</b>

#### 4.5.4 The Resultant Thermomechanic fatigue Reliability, R(N)

The thermo-mechanic fatigue fracture of the S7 solder that wipes the tinned copper braid onto the copper bell housing is a function of cyclic temperature variations caused by load cycling and external temperature variations. The temperature changes in the S7 solder obtained by Fourier's heat equation are obtained in Section 5.3.2 (See Figure 23). Using a typical winter load profile, the S7 solder has at least two thermal cycles per day, with two peak consumptions in the morning and evening.

The ratio of operating temperature range,  $\Delta T$ , to the maximum design temperature range,  $\Delta T_0$ , as well as the ratio of operating thermal frequency,  $f_T$ , to design thermal frequency,  $f_{T0}$ , are critical in fatigue fracture. Figure 4.18 and Figure 4.19 show the effect of temperature range and thermal cycle frequency on the reliability of the cable terminations. By holding the thermal cycle frequency constant at  $1.157 \times 10^{-5}$  Hz and varying the temperature from 5 to 20 °C, Figure 4.18 shows that the reliability changes marginally. If however the temperature range is held

constant at 11.53 °C and cycle frequencies varied from  $f = 1.157 \times 10^{-5}$  Hz to  $f = 4.629 \times 10^{-5}$ , the changes in reliability are relatively more significant as shown in *Figure 4.19*.

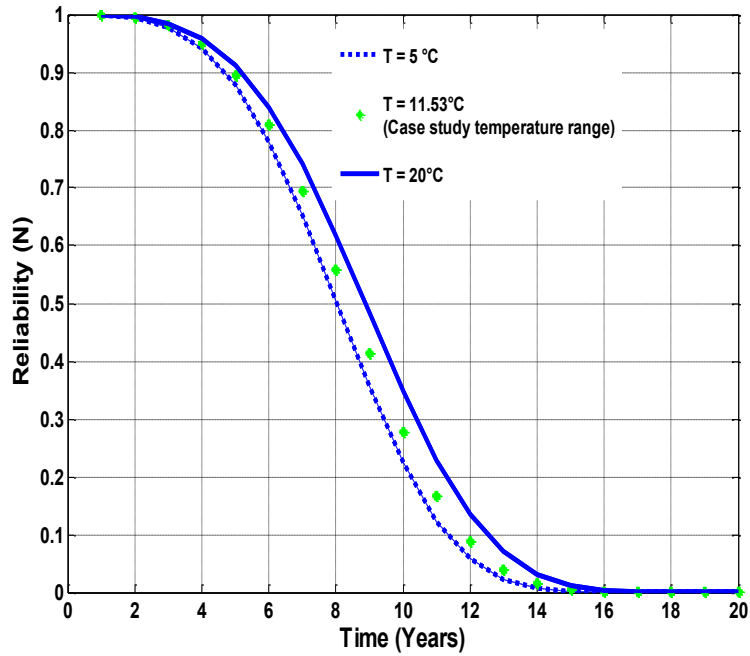


*Figure 4.18. Thermo-mechanic fatigue factor at changing thermal cycles and fixed temperature*

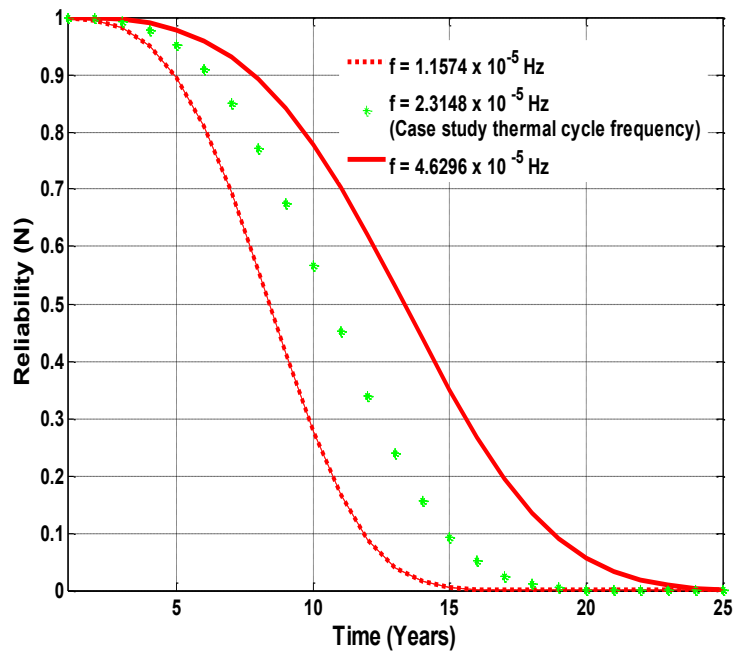


*Figure 4.19. Thermo-mechanic fatigue factor at changing temperature range and fixed thermal cycle frequency*

The model therefore shows that the S7 solder reliability is more sensitive to thermal cycle frequency in comparison to changes in temperature range. The inverse relationships between the thermo-mechanic reliability of the termination and the temperature range as well as the cycling frequency in this case study is attributed to the non-linear stress strain characteristic of tin-lead solders.

Using a Coffin-Manson based thermo-mechanic fatigue model, tin-lead solders tend to have a non-linear stress curve. Under high strains, tin-lead solder undergoes a mixed trans granular-intergranular (creep fatigue interaction), while under low strains the intergranular (creep) mechanism is dominant. This model does not explicitly account for the dwell time as well as the ramp time of the cycling temperatures. The principle degradation mechanism in the dwell time region is creep while during the ramping period fatigue occurs [67] [68]. A coupled creep-fatigue model by Chen et al [68] can achieve a more accurate estimation of reliability, however this approach would require online data logging measurement of the stress and strain parameters of the S7 solder.

Thermal properties of secondary materials/components in the termination system such as solders, conductive paint, PVC and semi-conductive tape under fault current conditions need to be characterised. The propagation of corrosion fatigue crack may occur inter-granularly or trans-granularly depending on the nature of the electrolyte (pH), temperature fluctuations and metal properties [69]. The other degradation mechanism identified in the termination was galvanic corrosion which is analysed in the next section.

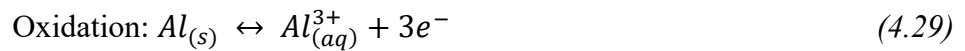
## **4.6 The Galvanic Corrosion Degradation Model**

Gradual chemical or electrochemical reactions within cable terminations introduce new substances that alter the electrical and mechanical properties of metallic joints. Visible evidence of corrosion occurs when there is pitting, surface etching or the presence of corrosion by-products [69]. Galvanic and crevice corrosion are the two main types of non-mutually exclusive forms of corrosion that may occur inside a cable termination. Galvanic corrosion occurs when two dissimilar metals are in contact in the presence of an electrolyte and one metal corrodes preferentially [70] while crevice corrosion occurs at dissimilar metal interfaces, crevices or where there is stagnant solutions on metal surfaces [23].

During corrosion, water goes through hydrogen evolution reaction depending on its pH. In an acidic electrolytic solution, the water half reaction is given in *Equation 4.27*. In a weak neutral or basic electrolyte solution the hydrogen evolution reaction is given in *Equation 4.28* [70].



The major redox reaction is that of copper and aluminium and it is shown in *Equations 4.29* and *4.30*



Hollingsworth and Raine [23] found that the corrosion of aluminium by AC electrolysis is aided by the presence of a standing voltage greater than 5 V. In the cable standing voltage at the sheath end is due to induced voltages from the conductor and a non-perfect path to ground. The induced voltage magnitude is dependent on the adopted bonding method. The corrosion redox potential difference as shown in *Equation 4.31* is dependent on the standard electro-potential differences of the metals and the thermodynamic flow of ions between the metals.

$$V_h = V^0 - \frac{RT}{F} \ln \frac{[Red]}{[Ox]} - \frac{m_p RT}{n_e F} \ln[H^+] \quad (4.31)$$

Where  $V_h$  is the redox potential,  $V^0$  is the standard potential difference of the metals,  $F$  is the Faraday constant,  $n_e$  is the number of transferred electrons,  $m_p$  is the number of exchanged protons,  $T$  is the temperature,  $R = 8.314 \text{ J/mol.K}$  is the universal gas constant,  $[H^+]$  concentration is a measure of pH and  $[Red]$  is the concentration of reduced component  $[Ox]$  is the concentration of oxidized component [71].

An increase in temperature, moisture content and  $H^+$  ion concentration (low/high pH) results in an acceleration of ion and electron migration from the anode to the cathode [72]. However, an optimum combination of pH and redox potential at a given temperature is required to ensure that corrosion occurs as illustrated in Pourbaix's [73] theory on thermodynamics of corrosion as schematically illustrated in *Figure 4.20*.

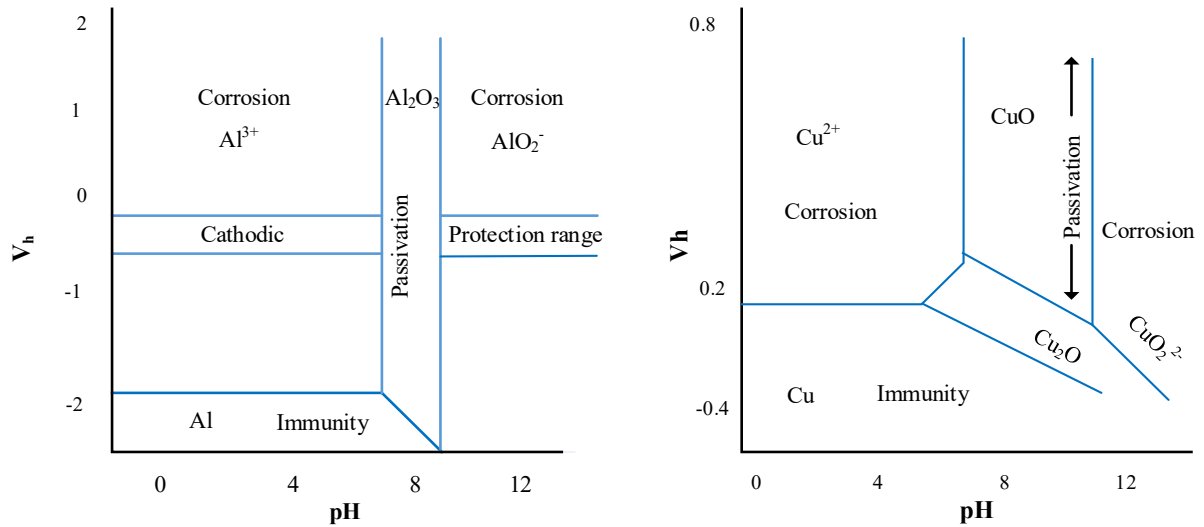


Figure 4.20. *V-pH diagram of Aluminium and copper at 25 °C. Adopted from [74]*

In the case study, factors that affect corrosion rate (voltage, temperature, ion concentration, current) must be determined and included in the model. A method in determining corrosion life is presented in the next section.

#### 4.6.1 The corrosion stress life factor, $\alpha(C)$

Feinberg characterised the life due to corrosion as a function of temperature and humidity. For corrosion to occur, a difference between anodic and cathodic current should be present. This difference is enabled when the magnitude of free energy is high enough to allow the release of electrons from the metals and causes corrosive current to flow. Gibbs free energy is defined by Equation 4.32.

$$\Delta G = -n \cdot H \cdot V \quad (4.32)$$

Where  $\Delta G$  is Gibbs free energy,  $n$  is the number of moles,  $H = 96483.038 \text{ J/mol} \cdot V$  Faradays constant and  $V$  is the corrosion cell potential between aluminium and copper is 2V (Al: 1.67 V, Cu: -0.34V) [73] [75].

A positive cell potential ensures that corrosion between the two metals occurs spontaneously as Gibbs free energy is negative [72]. The net current or rate of corrosion as a function of Gibbs free energy and temperature is therefore given by Equation 4.33.

$$i_{corr} = i_a - i_c = I_{0a} \exp\left(\frac{\Delta G_a}{RT}\right) - I_{0c} \exp\left(\frac{\Delta G_c}{RT}\right) \quad (4.33)$$

Where the dominant current is the anodic current. Gibbs free energy can be expressed as a function of the activation energy of corrosion as shown in *Equation 4.34*.

$$\frac{\Delta G}{R} = \frac{A_c}{k_B} \quad (4.34)$$

Skrovan et al [76] measured the activation energy of corrosion  $A_c$  of 0.8 eV which is used in the present case study. This activation energy results in a minimum of 0.39 moles transferred in the redox reaction of copper and aluminium in the absence of the oxide layer. In accordance with Pourbaix's diagrams shown in *Figure 35*, a combination of optimum voltage and electrolytic concentration is required to initiate corrosion. In metals, the reduction of water as expressed in *Equation 4.27* determines the rate of corrosion. In this regard, humidity is used as a corrosion rate determining parameter.

The effect of humidity on corrosion rate is modelled according to Pecks law [75]. Pecks humidity law, states that the rate of corrosion reaction is directly proportional to the power of the relative humidity [72]. A threshold amount of humidity/ion concentration is required to facilitate corrosion. The ratio of the actual humidity to the minimum humidity that the metals can withstand before corrosion commences is called the humidity acceleration factor [72] as shown in *Equation 4.35*. The temperature and activation energy-based acceleration factor is computed using Arrhenius Law as shown on *Equation 4.36*.

$$AF_H = \left(\frac{RH}{RH_0}\right)^M \quad (4.35)$$

$$AF_T = \exp\left\{\frac{A_c}{k_B}(1/T_o - 1/T)\right\} \quad (4.36)$$

Where  $RH$  is the percentage relative humidity,  $RH_0$  is the minimum relative humidity that will cause corrosion to occur in the metallic joint.  $M$  is a positive constant of 2.66 as the rate of corrosion increases with humidity in metals [72].

The overall damage caused by corrosion as a function of humidity and temperature in the electro-chemical reaction can be combined into a corrosion life factor using *Equations 4.37 and 4.38*.

$$\alpha(C) = AF_T AF_H \quad (4.37)$$

$$\alpha(C) = \left(\frac{RH}{RH_0}\right)^{-M} \cdot \exp\left\{\frac{A_c}{k_B}(1/T_{CO} - 1/T_{max})\right\} \quad (4.38)$$

#### 4.6.2 The Corrosion Reliability, $R(C)$

The Pecks law combined with the Arrhenius law compute the galvanic corrosion life factor as presented in *Section 5.4.1 Equation 5.37* [75]. A parametric approach was taken in establishing the threshold relative humidity  $RH_0$  required to initiate corrosion. The activation energy of aluminium corrosion was obtained from Skrovan's method [76], and the maximum temperature at the aluminium to CSA interface is obtained by using the Fouriers heat equation as presented in *Figure 4.15* in *Section 4.3.2*. The parameters used to compute the corrosion stress factor are listed in *Table 4.7* and the resultant corrosion stresss life factor is computed as 0.67.

*Table 4.7. Corrosion parameters*

Description	Symbol	Value
Maximum annual site humidity (Site average annual humidity)	$RH$	59 %
Critical threshold humidity	$RH_0$	40 %
Corrosion metal constant from Feinberg et al[77]	$M$	2.66
Aluminium galvanic corrosion energy [7], [78]	$A_c$	0.8 eV
Boltzmann constant	$k_B$	$8.617 \times 10^{-5}$ eV/K
Design maximum operating temperature	$T_{CO}$	90°C
Maximum temperature, Aluminium and Copper interface (From Figure 5)	$T_{max}$	89 °C
<b>Corrosion stress life factor (Computed in Equation 4.38)</b> Feinberg et al [77]	$\alpha(C)$	<b>0.67</b>

*Figure 4.21* shows the effects of corrosion on the termination reliability under different humidity and activation energy conditions. There is a direct relationship between the humidity and the corrosion reliability. When the relative humidity is less than 20% corrosion at the copper braid to CSA interface is low enough to allow the termination to exceed its design life span of 40 years.

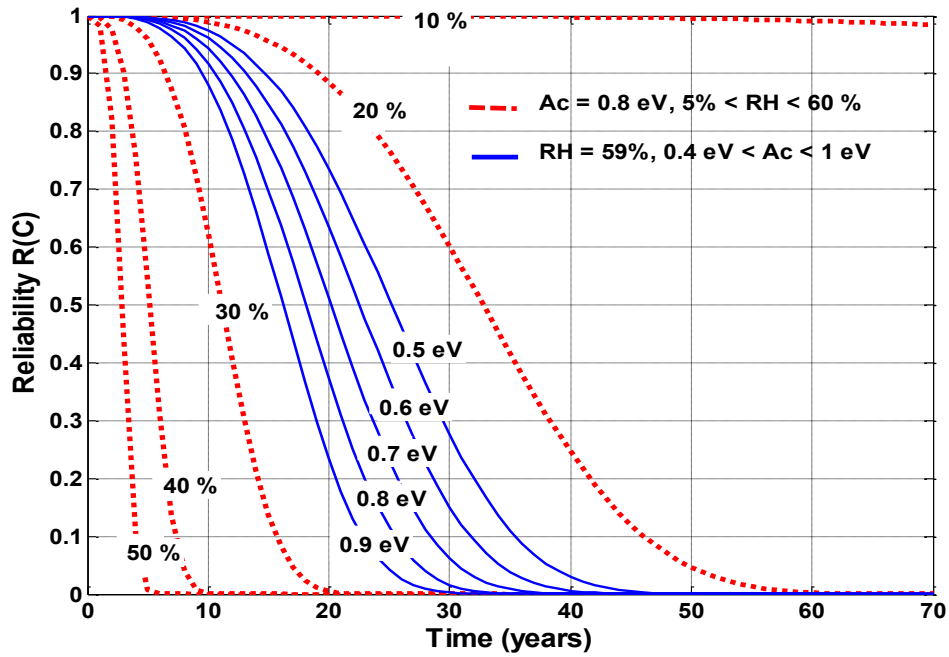


Figure 4.21. Reliability under corrosion at different humidity's and corrosion activation energy

There is an inverse relationship between the activation energy and corrosion reliability. The direct relationship between activation energy and cell potential is an indication of how the corrosion process is aided as the voltage gradient between the metals increases. A higher voltage difference increases the rate of current flow, where the rate of aluminium mass dissolving/aging is increased [75]. Van Deursen et al [79] have shown that in a copper to aluminium interface, under corrosion, the aluminium resistance increases substantially in comparison to the copper resistance. In this case study a Ductor contact resistance that exceeds  $30 \mu\Omega$  indicates a faulty copper braid to CSA interface [20].

Initially, galvanic corrosion does not occur as the S7 solder and other materials shield the interface from moisture ingress. A three parameter Weibull distribution which includes the location parameter that represents the time at which corrosion commences may be more suitable in this case study. The approach could however not be implemented because the exact time at which water reaches the copper braid to CSA is not known in this case study. Furthermore, the tin plating on the copper and the oxide layer on the aluminium temporarily protects the metals from corrosion. These protective layers are removed by crevice corrosion. Non-uniform oxygen and pressure concentration on the metal surface [23] result in a non-uniform oxide layer on the CSA. This exposes parts of the CSA to galvanic corrosion in the presence of moisture. Galvanic corrosion of aluminium occurs dis-continuously as the galvanic

cell conditions change with time. Temperature variations, accumulation of corrosion by-products (e.g Al(OH)<sub>3</sub>) and alternating currents will both intermittently aid and disallow the corrosion process [74]. In this regard the model overestimates the extent of corrosion. However, the inability to identify when moisture reaches the copper braid to CSA interface assumes the corrosion process to start when the termination is installed. This assumption compensates for the models over estimation, where it excludes the intermittent nature of corrosion. If the time at which corrosion is initiated is obtained by monitoring the contact resistance of the termination through Ductor test, a three parameter Weibull distribution can be used for the corrosion reliability as shown in *Equation 4.39* [25].

$$P_{wc}(t) = 1 - \exp \left[ - \left( \frac{t-\gamma}{\alpha} \right)^\beta \right] \quad (4.39)$$

Where  $P_{wc}(t)$  is the cumulative probability of galvanic corrosion failure,  $\gamma$  is the time at which galvanic corrosion commences,  $\alpha$  is the scale parameter and  $\beta$  is the shape parameter.

#### **4.7 Summary and Conclusion**

The physio-chemical mechanisms of the various degradation mechanisms terminations as identified in the present case study were presented. These mechanisms are electro-thermal, thermomechanic fatigue and galvanic corrosions. Thermo-mechanic fatigue and corrosion are the most prevalent degradation mechanisms with stress factors less than one, while electro-thermal degradation has a stress factor greater than one. Using the Weakest Link Principle, the overall reliability of the cable termination is computed by combining the statistically fitted Weibull distribution to the degradation life factors. The overall reliability for the case study cable terminations is presented in the next section.

## 5. THE OVERALL RELIABILITY MODEL FOR THE TERMINATION

---

In this section the overall reliability of the cable terminations is presented being a consolidation of the various attendant life stress factors identified in the previous chapter. The overall reliability is computed by using the Weakest Link Principle. The outcome of the model is discussed.

---

The product of individual functions representing reliabilities due to each degradation mechanism gives the overall reliability of the termination system in accordance with the Weakest Link Principle. Consequently, the most prevalent degradation mechanism has the biggest impact on the overall reliability of the termination. The failure of one component in the termination will result in the failure of the entire system.

In the previous chapter, the analytical expressions for the stress factors  $\alpha_x$  of each degradation stress was formulated. For convenience the expressions are listed below for each identified degradation mechanism in the termination.

- Electric stress life factor  $\alpha_E$
- Thermal stress factor  $\alpha_T$
- Thermomechanic fatigue  $\alpha_N$
- Galvanic corrosion  $\alpha_C$

The corresponding probability of failure under each degradation mechanism  $x$  can be evaluated using *Equation 5.1* and expanded as shown in *Equation 5.2*

$$R_x(t) = 1 - P(t, \alpha(x)) \quad (5.1)$$

$$R_x(t) = 1 - \left[ 1 - \exp\left[-(t/(\alpha_x \alpha))^\beta\right] \right] \quad (5.2)$$

Where  $R_x(t)$  is the life fraction left due to degradation mechanism  $x$  after operation time  $t$  and  $P(t, \alpha_x)$  is the cumulative probability of failure with time under degradation mechanism  $x$ . The probability of failure due to each forensically identified failure mechanism is computed using the Weibull distribution and depicted in *Figure 5.1*.

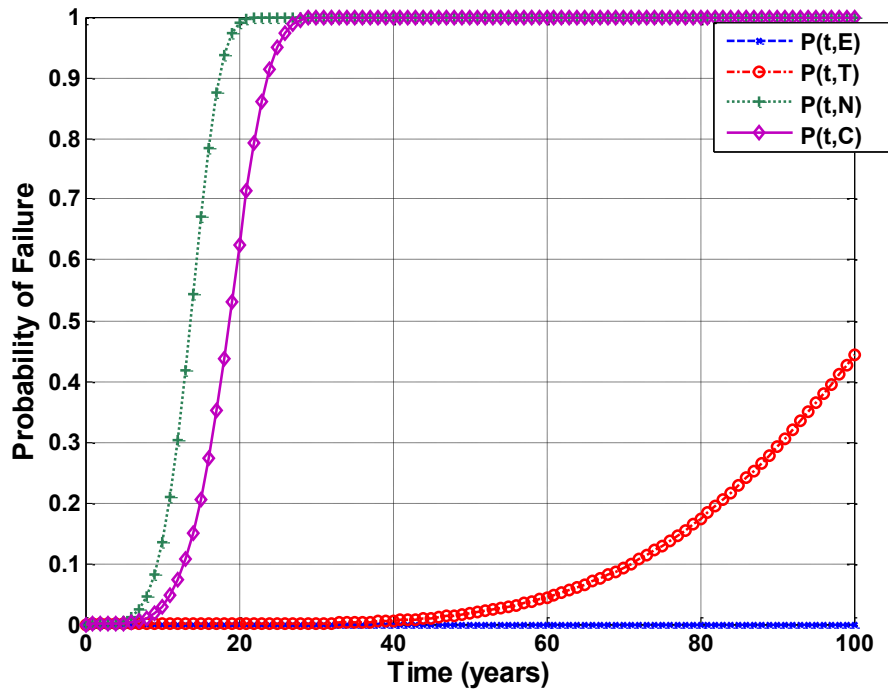


Figure 5.1. Weibull Cumulative probability of failure with time at 29 years in operation due to all degradation mechanisms

It is evident that thermomechanic and galvanic corrosion are more likely to cause complete termination failure. Figure 5.2 shows that after 29 years in operation the terminations are 100 % susceptible to failure due to both corrosion and thermomechanic fatigue. Electric and thermal degradation are the least prevalent degradation mechanisms with less than 10% probability of failure after 40 years in operation.

With the knowledge of individual reliabilities due to individual degradation mechanisms, the overall reliability of the cable termination can be determined as a product of the individual reliabilities as expressed in Equation 5.3, that can be expanded into Equations 5.4 and 5.5

$$R_{E,T,N,C}(t) = R_E(t) \cdot R_T(t) \cdot R_N(t) \cdot R_C(t) \quad (5.3)$$

$$\begin{aligned}
R_{E,T,N,C}(t) = & [1 - (1 - \exp(-(t/(\alpha_{ET} \cdot \alpha))^{\beta}))] \times \\
& [1 - (1 - \exp(-(t/(\alpha_N \cdot \alpha))^{\beta}))] \times \\
& [1 - (1 - \exp(-(t/(\alpha_C \cdot \alpha))^{\beta}))] \quad (5.4)
\end{aligned}$$

$$\begin{aligned}
R_{E,T,N,C}(t) = & \left[ \exp(-(t/(\alpha_E \cdot \alpha))^{\beta}) \right] \times \\
& \left[ \exp(-(t/(\alpha_T \cdot \alpha))^{\beta}) \right] \times \\
& \left[ \exp(-(t/(\alpha_N \cdot \alpha))^{\beta}) \right] \times \\
& \left[ \exp(-(t/(\alpha_C \cdot \alpha))^{\beta}) \right]
\end{aligned} \tag{5.5}$$

Where  $\alpha_E$  is the electric stress factor,  $\alpha_T$  is the thermal stress factor,  $\alpha_N$  is the thermo-mechanic stress factor and  $\alpha_C$  is the corrosion stress factor. The scale  $\alpha$  and shape  $\beta$  parameter are as calculated in *section 4.1*.

A plot of *Equation 5.5* using parameters in *Tables 4.3,4.5,4.6 and 4.7* is presented in *Figure 5.2* and is the overall reliability of the termination at the time of the study. In the same *Figure 5.2*, plots of individual reliabilities corresponding to electrothermal, thermomechanical and galvanic life factors are shown. The results indicate that electrothermal stress hardly reduces the reliability of the termination from the time of installation to 40 years in service. However, thermomechanical stress causes a reliability of less than 10% after 18 years and galvanic degradation reduces the termination reliability to less than 10% after 24 years in operation.

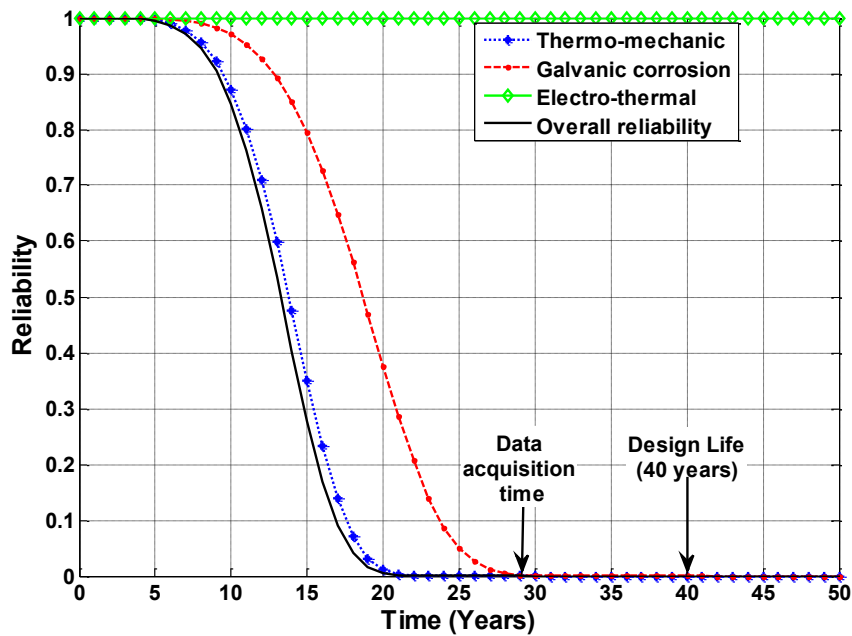


*Figure 5.2. Overall reliability after 29 years in operation.*

The cable terminations in the case study substation have metallic interfaces that are exposed to prevalent thermomechanic fatigue and corrosion. Elimination of galvanic corrosion by ensuring a water tight termination and using low or lead-free solder may improve the reliability of the metallic interfaces. Sn60Pb40 solder has a higher operating temperature range in comparison to Sn35Pb64 solder which marginally improves the thermal-mechanic strength of the copper braid to bell housing joint as shown in *Figure 5.3*. However, when water is restricted from entering the cable termination, the corrosion reliability is significantly improved with a higher probability of the cable termination being able to exceed the design life. Design modifications that make the cable termination to be water-proof have higher impact on the extension of the cable termination reliability.

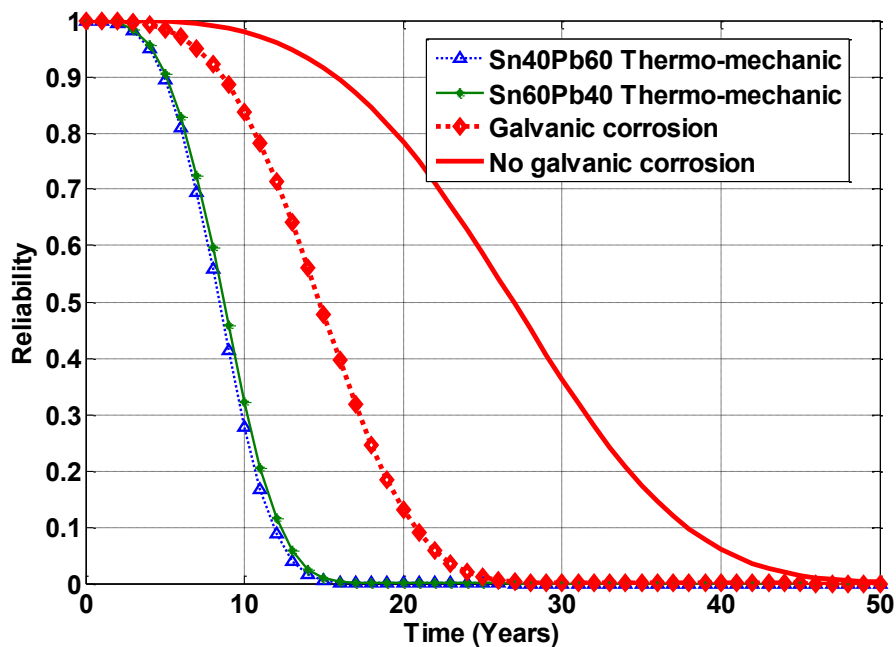


*Figure 5.3. Effect of Sn60Pb40 solder and absence of galvanic corrosion on reliability of the termination*

The results obtained in this case study give a projection on the likelihood of the terminations reaching their design life when evaluated after 29 years in operation. The trends shown are subject to change with time as 3 terminations in the case study were still operational and their time of failure would change the scale and shape parameters of the Weibull distribution, thus giving a different reliability projection with time. This model is therefore valid for specific designs where possible degradation mechanisms are known. A generic version of the model is presented in the next subsection

## 5.1 The Generic Model Philosophy

A generic reliability model can be used for customizing into specific designs and site-specific conditions. The generic reliability model can be computed using the stress factors relating to identified degradation mechanisms, a suitable distribution to fit the statistical time-to-failure data and the Weakest Link Principle. This generic model is given in *Equation 5.5* for a system of  $\alpha_n$  life factors.

$$R_x(t) = R_{x_1}(t) \cdot R_{x_2}(t) \cdot R_{x_3}(t) \cdot R_{x_4}(t) \cdot R_{x_n}(t) \cdot \quad (5.5)$$

Where  $R_x$  is the overall reliability,  $R_{x_1}$  is the reliability as a function of degradation mechanism  $x_1$ .  $R_{x_2}$  is reliability due to life factor  $x_2$  etc. up to life factor  $x_n$ .

Site specific parameters are obtained from online data logging systems while material specific parameters and possible degradation mechanisms are obtained from laboratory tests (In literature) conducted on the termination before installation. The procedure in developing design specific reliability models for terminations is as follows.

- Identify the population of the terminations of similar designs and installed during the same period.
- At a chosen time during the life period of the terminations, take a record of the time of failure of terminations and the number of healthy terminations. Compute the Weibull distribution analysis of the data to determine the corresponding shape and scale parameters.
- Determine the reliability (the probability that the termination will live up to the design life) as a function of each degradation mechanism life factor. Each life factor is modelled as an analytical expression being a function of the various factors that influence the specific degradation processes.
- The overall reliability at any given time, is a product of all the constituent reliabilities in accordance with the Weakest Link Principle.

## **5.2 Summary Conclusion**

The overall reliability of the case study cable terminations show that metallic interfaces exposed to thermomechanic fatigue and corrosion cause the most damage. The developed reliability model exhibits sensitivity to design changes and is only valid at the time the case study data was collected. A methodology in producing a model specific to design and operating parameters was highlighted. The conclusion on the outcomes of this research are presented in the next section

## 6. CONCLUSION

---

In this section the overall outcomes of this research work are presented in line with the research problem and objectives presented in sections 1.5 and 1.7.

---

Using a municipal case study, a reliability model for cable terminations has been developed. Although it has been developed from a specific case study, the model is generic in the sense that it can be customised for different termination designs for specific conditions. In the case study, systematic post-mortem analysis of the terminations resulted in the identification of degradation mechanisms which are modelled by the physics of failure. Site specific parameters are obtained from an online data logging system and material specific parameters are obtained from literature where laboratory tests were conducted. The cumulative nature of the model gives a continuous projection of remaining life as well as provides a possible cause of failure through the shape and scale parameters of the Weibull distribution. The reliabilities due to the identified degradation models are presented.

### 6.1 Thermomechanic Reliability

The thermomechanic fatigue reliability is function of cyclic temperature changes caused by load cycles and fault currents. In this case study thermomechanic fatigue is the most prevalent mode of failure, this does not suggest that load cycle currents are responsible for this outcome as they are within the substations' capacity. It is the copper to aluminium interfacing combination, coupled with the solders used that are susceptible to thermomechanic fatigue. For future designs copper to aluminium interfaces are discouraged while solders with better thermomechanic properties are recommended. This however does not guarantee high thermomechanic reliability as it is still a function of operating parameters, cable system condition and installation skills.

## **6.2 Corrosion Reliability**

In this case study moisture ingress into the termination results in prevalent galvanic corrosion at the copper to aluminium interface. Design adjustments that include the use of materials with improved waterproof properties will drastically improve the corrosion reliability. However, interfaces between dissimilar metals are not recommended as they are susceptible to crevice corrosion.

## **6.3 Electrothermal Reliability**

Electrothermal stress caused by the operating steady state electric field stress, transient electric field stresses and cyclic current load cycles does not cause detrimental damage to the cable terminations in the present case study. However, the model shows sensitivity to increased impulse voltage occurrence and magnitudes. Furthermore, the presence of system irregularities may result in higher induced thermal and electric stresses.

## **6.4 Conclusion Summary**

If all constituent modes of failure are identified, mathematical models of failure due to each degradation mechanism can be developed. In this case study, corrosion and fatigue fracture were identified as the most prevalent degradation mechanisms, while electrothermal degradation is a function of load cycles and overall system integrity.

The accuracy limitations of the model are in some of the model parameters that are not always precisely fixed. The model can also be used in evaluating termination design improvements provided all relevant material parameters are known. It can also be useful to process the online cable system condition monitoring data to obtain a real time computation of the cable accessory reliability and therefore aid in making more informed asset management decisions. A summary of the key findings of this research work are shown in *Table 6.1*.

Table 6.1 Conclusions drawn from the case study

Failure Mechanism	Applied laws	Model parameters
Electric degradation $\alpha(E, Ei)$	Inverse power law	<ul style="list-style-type: none"> <li>• Maximum steady state electric stress</li> <li>• Maximum design steady state stress</li> </ul>
Thermal degradation $\alpha_i(t, T)$	<ul style="list-style-type: none"> <li>• Arrhenius law</li> <li>• Cigre two loop network method</li> <li>• Fouriers heat equation</li> <li>• Miners law</li> </ul>	<ul style="list-style-type: none"> <li>• Maximum cyclic temperature</li> <li>• External annual temperature variations</li> </ul>
Thermomechanic fatigue $\alpha(N)$	<ul style="list-style-type: none"> <li>• Coffin-Manson Law</li> <li>• Landzberg and Norris Law</li> </ul>	<ul style="list-style-type: none"> <li>• Cyclic temperature range and frequency</li> </ul>
Corrosion $\alpha(C)$	<ul style="list-style-type: none"> <li>• Pecks Law</li> <li>• Gibbs free energy</li> <li>• Arrhenius Law</li> </ul>	<ul style="list-style-type: none"> <li>• Maximum operating relative humidity and threshold humidity</li> <li>• Maximum design relative humidity</li> <li>• Corrosion activation energy</li> <li>• Maximum temperature</li> </ul>
Overall reliability $R_{E,T,N,C}(t) = R_E(t) \cdot R_T(t) \cdot R_N(t) \cdot R_C(t)$	<ul style="list-style-type: none"> <li>• Stress factors due to all identified degradation mechanisms.</li> <li>• Weakest link principle</li> </ul>	<ul style="list-style-type: none"> <li>• Stress factors due to each degradation mechanism</li> </ul>

## REFERENCES

- [1] G. Mazzanti and M. Marzinotto, ‘Advanced Electro-Thermal Life and Reliability Model for High Voltage Cable Systems Including Accessories’, *DEIS*, vol. 33, no. 3, pp. 17–25, May/June.
- [2] B. S. Bernstein and W. Thue, ‘Historical Perspective of Electrical Cables’, in *Electrical Power Cable Engineering*, Marcel Dekker, Inc, 1999, pp. 3–14.
- [3] W. Thue, ‘Cable Performance’, in *Electrical Power Cable Engineering*, Marcel Dekker, Inc, 1999, pp. 257–264.
- [4] IEC60060, ‘High Voltage Test Techniques’, IEC, 1989.
- [5] W. Reder and D. Flaten, ‘Reliability Centered Maintenance for Distribution Underground Systems’, in *2000 Power Engineering Society Summer Meeting (Cat. No.00CH37134)*, 2000, vol. 1, pp. 551–556 vol. 1.
- [6] B. Florkowska, ‘Analysis of partial discharge mechanisms and their patterns for diagnosis of insulation systems’, in *Proceedings of 5th International Conference on Properties and Applications of Dielectric Materials*, 1997, vol. 1, pp. 279–282 vol.1.
- [7] IEC 60071-2, ‘Insulation Co-ordination Application Guide’, IEC, IEC 60071-2:1996, Dec. 1996.
- [8] G. Qiang, G. Weichun, W. Chenggang, G. Baohong, and J. Xiuchen, ‘High voltage equipment online monitoring system of smart substation’, in *IEEE PES Innovative Smart Grid Technologies*, 2012, pp. 1–5.
- [9] ‘IEC 61850 standard | IEC61850 Substation Automation - Substation Automation Systems & Solutions | Power System Substations | ABB’. [Online]. Available: <https://new.abb.com/substation-automation/systems/iec-61850>. [Accessed: 03-Mar-2019].
- [10] W. Nelson, *Accelerated Testing Statistical Models, Test Plans and Data Analysis*. New Jersey: John Wiley & Sons, 1990.

- [11] D. Kececioglu and J. A. Jacks, 'The Arrhenius, Eyring, inverse power law and combination models in accelerated life testing', *Reliab. Eng.*, vol. 8, no. 1, pp. 1–9, Jan. 1984.
- [12] G. Mazzanti, 'Analysis of the Combined Effects of Load Cycling, Thermal Transients, and Electro-thermal Stress on Life Expectancy of High-Voltage AC Cables', *IEEE Trans. Power Deliv.*, vol. 22, no. 4, pp. 2000–2009, Oct. 2007.
- [13] G. Mazzanti and G. Passarelli, 'A probabilistic life model for reliability analysis of power cables feeding electric traction systems', in *International Symposium on Power Electronics, Electrical Drives, Automation and Motion, 2006. SPEEDAM 2006.*, 2006, pp. 834–839.
- [14] M. Marzinotto, C. Mazzetti, M. Pompili, and P. Schiaffino, 'EPR lifetime under impulsive voltage stress', in *CEIDP '05. 2005 Annual Report Conference on Electrical Insulation and Dielectric Phenomena, 2005.*, 2005, pp. 26–29.
- [15] G. C. Montanari and G. Mazzanti, 'From thermodynamic to phenomenological multi-stress models for insulating materials without or with evidence of threshold (XLPE cables)', *J. Phys. Appl. Phys.*, vol. 27, no. 8, p. 1691, 1994.
- [16] M. Marzinotto and G. Mazzanti, 'Merging the electro-thermal life model for power cables with the statistical volume enlargement law', in *2014 IEEE Conference on Electrical Insulation and Dielectric Phenomena (CEIDP)*, 2014, pp. 502–505.
- [17] G. C. Montanari, G. Mazzanti, and L. Simoni, 'Progress in electro-thermal life modelling of electrical insulation during the last decades', *IEEE Trans. Dielectr. Electr. Insul.*, vol. 9, no. 5, pp. 730–745, Oct. 2002.
- [18] Elspec, 'Multi-Vendor Power Quality Management software.', *Elspec*, 26-Apr-2016. .
- [19] 'MapInfo Pro - Desktop GIS'. [Online]. Available: <https://www.pitneybowes.com/ca/en/location-intelligence/geographic-information-systems/mapinfo-pro.html>. [Accessed: 26-Mar-2019].
- [20] P. O'Holloran, 'Case Study Site Maintenance Engineer', 2017.

- [21] W.-B. Lee, K.-S. Bang, and S.-B. Jung, 'Effects of intermetallic compound on the electrical and mechanical properties of friction welded Cu/Al bimetallic joints during annealing', *J. Alloys Compd.*, vol. 390, no. 1–2, pp. 212–219, Mar. 2005.
- [22] H. Teng, H. Zhang, H. Yang, M. Zhou, and A. Tsui, 'Effect of Moisture and Temperature on Al-Cu Interfacial Strength', presented at the International Conference of Electronic Packaging Technology & High Density Packaging, 2008.
- [23] P. Hollingsworth and P. Raine, 'Aluminium Sheathed Cables', no. 1638, pp. 603–620.
- [24] P. Tobias and D. Trindade, *Applied Reliability*, 3rd ed. Chapman & Hall, 2012.
- [25] IEC62539, 'Guide for the statistical analysis of electrical insulation breakdown data', IEEE, 2007.
- [26] J. S. White, 'The Moments of Log-Weibull Order Statistics', *Technometrics*, vol. 11, no. 2, pp. 373–386, 1969.
- [27] R. Ross, 'Graphical methods for plotting and evaluating Weibull distributed data', in *Proceedings of 1994 4th International Conference on Properties and Applications of Dielectric Materials (ICPADM)*, 1994, vol. 1, pp. 250–253 vol.1.
- [28] G. Bahder, M. Sosnowski, C. Katz, T. Garrity, and R. Eaton, 'Physical Model of Electric Aging and Breakdown of Extruded Polymeric Insulated Power Cables', *IEEE Power Eng. Rev.*, vol. PER-2, no. 6, pp. 28–29, Jun. 1982.
- [29] X. G. Chen, L. Gu, X. R. He, and H. Y. Liao, 'Tracking failure process of XLPE-silicon rubber interface under impulse voltage', in *2012 International Conference on High Voltage Engineering and Application*, 2012, pp. 51–54.
- [30] M. Knenicky and R. Prochazka, 'Test site for nonstandard combined accelerated aging of medium voltage insulation systems', in *2016 IEEE International Conference on High Voltage Engineering and Application (ICHVE)*, 2016, pp. 1–4.
- [31] A. Cavallini, D. Fabiani, G. Mazzanti, G. C. Montanari, and A. Contin, 'Voltage endurance of electrical components supplied by distorted voltage waveforms', in *Conference Record of the 2000 IEEE International Symposium on Electrical Insulation (Cat. No.00CH37075)*, 2000, pp. 73–76.

- [32] G. Bahder, M. Sosnowski, C. Katz, R. Eaton, and K. Klein, 'Electrical Breakdown Characteristics and Testing of High Voltage XLPE and EPR Insulated Cables', *IEEE Power Eng. Rev.*, vol. PER-3, no. 7, pp. 41–42, Jul. 1983.
- [33] M. Cacciari, G. C. Montanari, L. Simoni, A. Cavallini, and A. Motori, 'Long-term electrical performance and life model fitting of XLPE and EPR insulated cables', *IEEE Trans. Power Deliv.*, vol. 7, no. 2, pp. 634–641, Apr. 1992.
- [34] Elspec, 'Multi-Vendor Power Quality Management software.', *Elspec*, 26-Apr-2016. .
- [35] CIGRE, 'Recommendations for Testing DC Extruded Cable Systems for Power Transmission at a Rated Voltage up to 500 kV'. Brochure CIGRE 496, Apr-2012.
- [36] L. Ying, B. Hui, S. Yu, and C. Xiaolong, 'The measurement of voltage endurance coefficient by electrical treeing test for XLPE cable insulation', in *2013 IEEE International Conference on Solid Dielectrics (ICSD)*, 2013, pp. 808–811.
- [37] L. Simoni, 'General Equation of the Decline in the Electric Strength for Combined Thermal and Electrical Stresses', *IEEE Trans. Electr. Insul.*, vol. EI-19, no. 1, pp. 45–52, Feb. 1984.
- [38] G. C. Montanari, D. Fabiani, and F. Ciani, 'Partial discharge and aging of AC cable systems under repetitive voltage transient supply', in *2016 IEEE Electrical Insulation Conference (EIC)*, 2016, pp. 379–382.
- [39] A. Cavallini, D. Fabiani, G. Mazzanti, G. C. Montanari, and A. Contin, 'Voltage endurance of electrical components supplied by distorted voltage waveforms', in *Conference Record of the 2000 IEEE International Symposium on Electrical Insulation (Cat. No.00CH37075)*, 2000, pp. 73–76.
- [40] L. Ying, B. Hui, S. Yu, and C. Xiaolong, 'The measurement of voltage endurance coefficient by electrical treeing test for XLPE cable insulation', in *2013 IEEE International Conference on Solid Dielectrics (ICSD)*, 2013, pp. 808–811.
- [41] IEC 60071-2, 'Insulation Co-ordination Application Guide', IEC, IEC 60071-2:1996, Dec. 1996.

- [42] E. Kuffel, W. Zaengl, and J. Kuffel, *High Voltage Engineering Fundamentals*, 2nd ed. Butterworth-Heinemann, 2000.
- [43] M. Stosur, M. Szewczyk, W. Piasecki, M. Florkowski, and M. Fulczyk, ‘GIS disconnecter switching operation #x2014; VFTO study’, in *2010 Modern Electric Power Systems*, 2010, pp. 1–5.
- [44] J. P. Crine, ‘Cable life predictions from breakdown and accelerated aging tests: influence of frequency and high fields’, in *2009 IEEE Electrical Insulation Conference*, 2009, pp. 435–438.
- [45] ‘IEEE Guide for Bonding Shields and Sheaths of Single-Conductor Power Cables Rated 5 kV through 500 kV’, *IEEE Std 575-2014 Revis. IEEE Std 575-1988*, pp. 1–83, Sep. 2014.
- [46] E. Kuffel, W. Zaengl, and J. Kuffel, *High Voltage Engineering Fundamentals*, 2nd ed. Butterworth-Heinemann, 2000.
- [47] F. Rizk and G. Trinh, *High Voltage Engineering*. Tylor & Francis Group, 2014.
- [48] R. Ross, ‘Dealing with Interface Problems in Polymer Cable Terminations’, *Electr. Insul. Mag.*, vol. 15, no. 4, 1999.
- [49] L. Bessissa, L. Boukezzi, D. Mahi, and A. Boubakeur, ‘Lifetime estimation and diagnosis of XLPE used in HV insulation cables under thermal ageing: arithmetic sequences optimised by genetic algorithms approach’, *Transm. Distrib. IET Gener.*, vol. 11, no. 10, pp. 2429–2437, 2017.
- [50] G. Mazzanti, ‘Analysis of the Combined Effects of Load Cycling, Thermal Transients, and Electro-thermal Stress on Life Expectancy of High-Voltage AC Cables’, *IEEE Trans. Power Deliv.*, vol. 22, no. 4, pp. 2000–2009, Oct. 2007.
- [51] G. Mazzanti, ‘Life Estimation of HVDC Cables Under the Time-Varying Electrothermal Stress Associated With Load Cycles’, *IEEE Trans. Power Deliv.*, vol. 30, no. 2, pp. 931–939, Apr. 2015.

- [52] M. Marzinotto and G. Mazzanti, ‘Merging the electro-thermal life model for power cables with the statistical volume enlargement law’, in *2014 IEEE Conference on Electrical Insulation and Dielectric Phenomena (CEIDP)*, 2014, pp. 502–505.
- [53] G. Mazzanti, ‘The combination of electro-thermal stress, load cycling and thermal transients and its effects on the life of high voltage ac cables’, *IEEE Trans. Dielectr. Electr. Insul.*, vol. 16, no. 4, pp. 1168–1179, Aug. 2009.
- [54] J. Coulson, J. Richardson, and J. Backhurst, *Fluid Flow Heat Transfer and Mass Transfer*, 6th ed., vol. 1. 1999.
- [55] J. Coulson, J. Richardson, and J. Backhurst, *Fluid Flow Heat Transfer and Mass Transfer*, 6th ed., vol. 1. 1999.
- [56] ‘IEC 60853-1 Ed. 1.0... | SAI Global’. [Online]. Available: <https://infostore.saiglobal.com/en-gb/Standards/IEC-60853-1-Ed-1-0-629981/>. [Accessed: 17-Oct-2017].
- [57] Datasheet, ‘Large Conductor HV XLPE Cable Data Sheet’. CBI Electric African Cables.
- [58] H.-S. Choi, W.-S. Seo, and D.-K. Choi, ‘Prediction of reliability on thermoelectric module through accelerated life test and Physics-of-failure’, *Electron. Mater. Lett.*, vol. 7, no. 3, p. 271, Sep. 2011.
- [59] R. Shenoj and J. Xiong, *Fatigue and Fracture Reliability Engineering*. London: Springer-Verlag, 2011.
- [60] M. Fine, Y. Chung, and R. . McCormick, ‘Fatigue Failure in Metals’, in *ASM Handbook: Fatigue and Fracture*, vol. 19, ASM International.
- [61] K. S. Ravi Chandran, ‘New approach for the correlation of fatigue crack growth in metals on the basis of the change in net-section strain energy’, *Acta Mater.*, vol. 129, pp. 439–449, May 2017.
- [62] T. Anzawa, Q. Yu, M. Yamagiwa, T. Shibutani, and M. Shiratori, ‘Power cycle fatigue reliability evaluation for power device using coupled electrical-thermal-mechanical

- analysis’, in *2008 11th Intersociety Conference on Thermal and Thermomechanical Phenomena in Electronic Systems*, 2008, pp. 815–821.
- [63] H. Bargmann, I. Rüstenberg, and J. Devlukia, ‘Reliability of Metal Components in Fatigue: A Simple Algorithm for the Exact Solution’, *Fatigue Fract. Eng. Mater. Struct.*, vol. 17, no. 12, pp. 1445–1457, Dec. 1994.
- [64] H. Bargmann, I. Rüstenberg, and J. Devlukia, ‘Reliability of Metal Components in Fatigue: A Simple Algorithm for the Exact Solution’, *Fatigue Fract. Eng. Mater. Struct.*, vol. 17, no. 12, pp. 1445–1457, Dec. 1994.
- [65] H. Cui, ‘Accelerated Temperature Cycle Test and Coffin-Manson Model for Electronic Packaging’, in *Annual Reliability and Maintainability Symposium, 2005. Proceedings*, 2005, pp. 556–560.
- [66] C. Basaran and J. Jiang, ‘Measuring intrinsic elastic modulus of Pb/Sn solder alloys’, *Elsevier*, vol. 34, pp. 349–362, Apr. 2002.
- [67] J. Pulido, ‘Reliability Analysis for Components under Thermal Mechanical Loadings’, *Reliab. Maintainab. Symp.*, 2012.
- [68] Y. Chen and R. Kang, ‘Coupling Damage and Reliability Modelling for Creep and Fatigue of Solder Joint’, *Microelectron. Reliab.*, vol. 75, pp. 233–238, 2017.
- [69] A. Cheng and N. Chen, ‘Corrosion fatigue crack growth modelling for subsea pipeline steels’, *Elsevier Ocean Eng.*, vol. 142, no. 10–19, 2017.
- [70] N. A. Jaffrey and S. Hettiwatte, ‘Corrosion detection in steel reinforced aluminium conductor cables’, in *2014 Australasian Universities Power Engineering Conference (AUPEC)*, 2014, pp. 1–6.
- [71] J. . Velazquez, J. . Cruz-Ramirez, A. Valor, V. Venegas, F. Caleyó, and J. . Hallen, ‘Modeling localized corrosion of pipeline steels in oilfield produced water environments’, *Elsevier Eng. Fail. Anal.*, vol. 79, pp. 216–231.
- [72] ‘On thermodynamic reliability engineering - IEEE Xplore Document’. [Online]. Available: <http://ieeexplore.ieee.org/document/877330/>. [Accessed: 15-Aug-2017].

- [73] R. Baboian and S. Begum, 'Corrosion, Galvanic', in *Reference Module in Materials Science and Materials Engineering*, Elsevier, 2016.
- [74] 'Aluminum E-pH (Pourbaix) diagram'. [Online]. Available: <http://corrosion-doctors.org/Corrosion-Thermodynamics/Potential-pH-diagram-aluminum.htm>. [Accessed: 19-Aug-2017].
- [75] A. Feinberg and A. Widom, 'On thermodynamic reliability engineering', *IEEE Trans. Reliab.*, vol. 49, no. 2, pp. 136–146, Jun. 2000.
- [76] J. Skrovan, 'Activation Energy for the Corrosion of Aluminum Powders in Water', *ECS Trans.*, vol. 41, no. 25, pp. 143–154, May 2012.
- [77] A. Feinberg and A. Widom, 'On thermodynamic reliability engineering', *IEEE Trans. Reliab.*, vol. 49, no. 2, pp. 136–146, Jun. 2000.
- [78] J. Skrovan, 'Activation Energy for the Corrosion of Aluminum Powders in Water', *ECS Trans.*, vol. 41, no. 25, pp. 143–154, May 2012.
- [79] A. van Deursen, B. Kruizinga, P. A. A. F. Wouters, and E. F. Steennis, 'Impact of corrosion on the reliability of low voltage cables with aluminium conductors', in *2017 52nd International Universities Power Engineering Conference (UPEC)*, 2017, pp. 1–6.

## A. APPENDIX

### A.1 Electric transients

ATP draw was used to simulate switching and lightning transients in the cable termination in the absence of a grounded surge arrester. The termination is modelled with a characteristic impedance of  $30 \Omega$ . A simple circuit using characteristic impedances is shown in *Figure A.1*. Pi model parameters of the 100 m cable are listed in *Table A.1*.

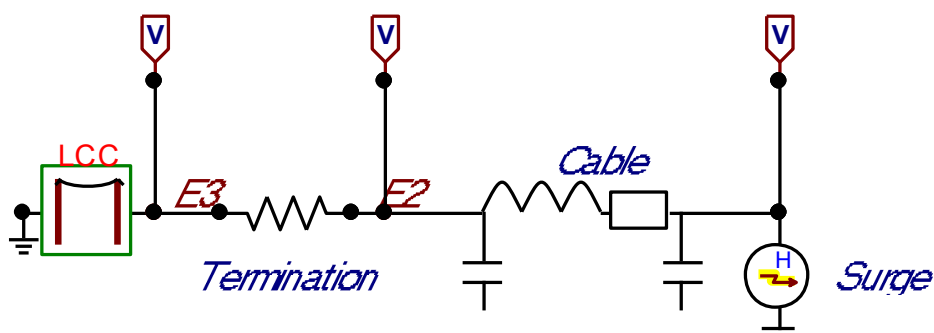


*Figure A.1. A simplified simulation circuit of switching surge in ATPDraw*

*Table A.1.. Cable model used in ATPDraw*

RLC Pi model, 100 m XLPE CSA Cable	
Resistance	0.0010679 $\Omega$ /m
Inductance	0 mH/m
Capacitance	0.00024 $\mu$ F/m

The transmission line is modelled using a Jmarti model. The parameters used in this model are presented in *Figure A.2* and *Figure A.3*.

	Ph.no.	Rin	Rout	Resis	Horiz	Vtower	Vmid	Separ	Alpha	NB
#		[cm]	[cm]	[ohm/km DC]	[m]	[m]	[m]	[cm]	[deg]	
1	1	0.55	1.55	0.0585	-17.5	27.9	13	60	45	1

Figure A.2. Transmission line parameters

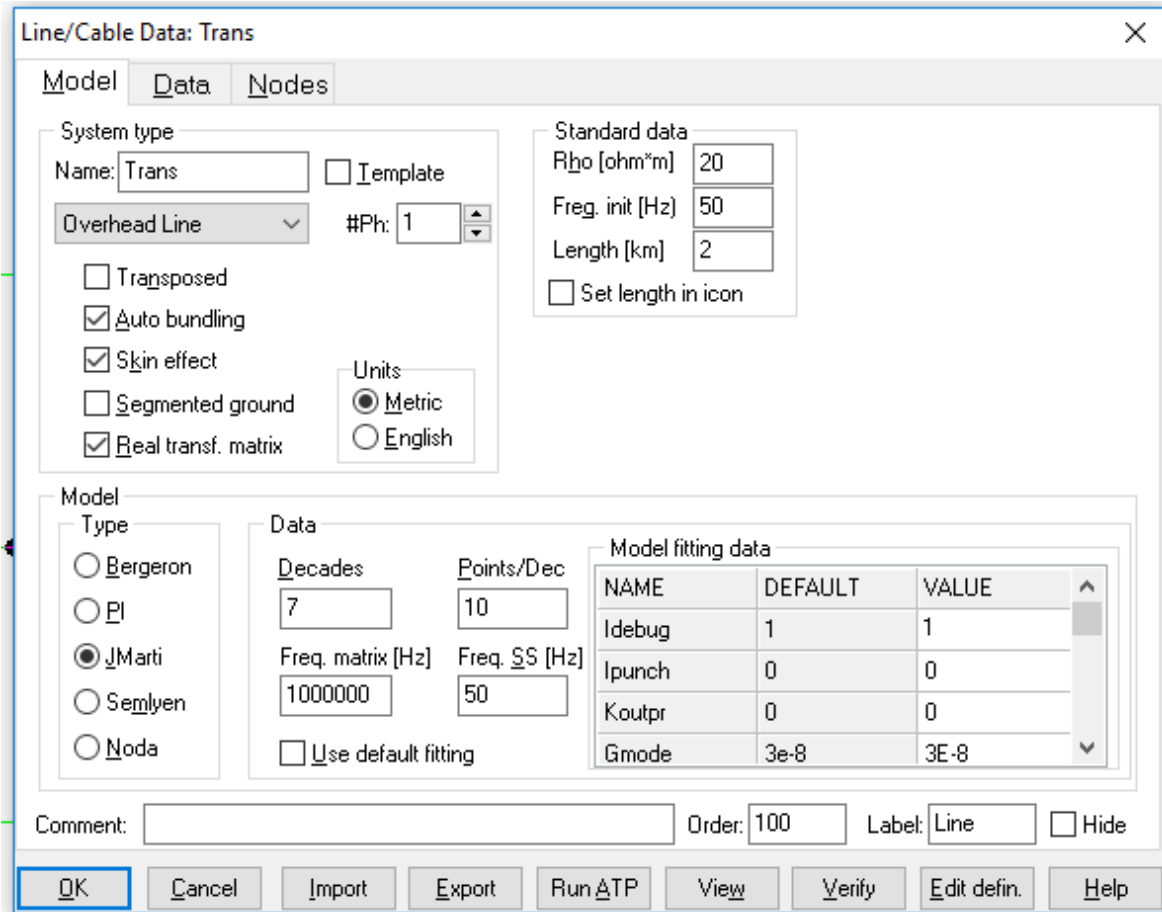


Figure A.3. JMarti 2 km transmission line parameter values ATPDraw

## A.2 Electric Field Simulations

Electric field simulations were conducted in FEMM software package. These simulations show the electric field intensity within the termination at a specific core and sheath voltage as presented in Figure 4.8 and 4.9. The parameters used to in the FEMM model are listed in Table A.2 below.

Table A.2. The dielectric spectroscopy of main insulators used in 88kV XLPE cable termination

Material	Permittivity at 50 Hz
ACP (Aluminium composite plastic) tape	3.1
PVC (polyvinyl chloride) tape	2.8
XLPE	2.5
Epoxy	3.6
SiR (silicon rubber)	4.0

### A.3 Thermal Simulations

Thermal simulations were conducted using the FEMM software package. These were conducted at specific conductor and sheath currents as shown in *Figure 4.16*

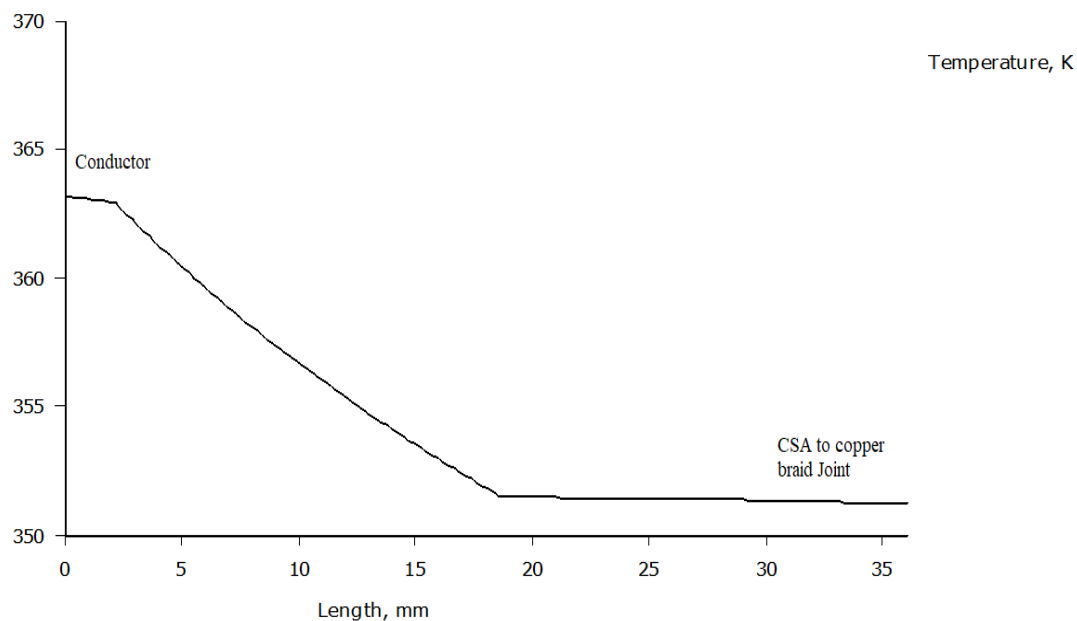


Figure A.4. Temperature from conductor (363.15 K) to wiped joint

### A.4 Supplementary Data

A copper and aluminium interface are susceptible to mechanical failure due to differences in mechanical properties. These different mechanical properties used to model the thermomechanic fatigue reliability in Section 4.3 are listed in *Table A.3*.

Table A.3 solder content according to ASM International [85]

	Pb	As	Bi	Cu	Fe	Sb	Sn
<b>SABS 24 S7(PbSn35)</b>	balance	0.03	0.25	0.08	0.02	0.3	34-36

Furthermore, some material specific parameters used in the thermomechanic fatigue model are listed in Table A4 and Table A5.

Table A4. Termination material properties

Material	Thermal conductivity ( $W \cdot m^{-1} \cdot K^{-1}$ )	Young's Modulus ( $10^9 N/m^2$ )	Relative density ( $kg/m^3$ )	Heat capacity ( $J/kg \cdot K$ )	Coefficient of Thermal Expansion
Aluminium	237	69	2700	921.109	(21 -24 x $10^{-6}$ m/mK)
Copper	401	117	8960	376.812	
90/10 tin-lead	50	47			
35/0.3/64.7 Sn/Sb/Pb	57	45			
XLPE	0.1-0.3		930	2350	
Silicon	0.165		1100	2010	
Rubber					
Epoxy	0.03		1.11 – $1.4 \times 10^3$		

Table A5. Material Property Differences between Aluminium foil sheath (T.1B and copper braid)

Properties	T.1 B Aluminium Sheath	Copper braid
Coefficient of thermal linear expansion (0-100 °C)	$24 \times 10^{-6}$	$17 \times 10^{-6}$
Thermal conductivity (0-100 °C)	0.54 cal/sec/cm/°C	401 W/(mK)
Resistivity at 20 °C	$2.85 \times 10^{-6} \Omega\text{cm}$	$1.68 \times 10^{-8} \Omega\text{m}$
Ultimate tensile strength at 20 °C	5.5 – 7.0 tons/inch <sup>2</sup>	200 MPa
Elastic modulus	$10 \times 10^6 \text{ lb./inch}^2$	
Fatigue endurance limit	$\pm 3.1 \text{ tons/in}^2$	



## B AUTHOR'S JOURNAL PUBLICATION

# *A Reliability Assessment Model for an Outdoor 88 kV XLPE Cable Termination*

**Key words:** Reliability model, Arrhenius, Inverse power law, Pecks law, Reliability, Weibull, XLPE Cable Termination

**Samantha Chimunda, Cuthbert Nyamupangedengu**

*University of the Witwatersrand, Johannesburg  
School of Electrical and Information Engineering  
Private Bag, 3  
Wits 2050  
Johannesburg, South Africa*

### **Abstract**

A metropolitan power utility has been experiencing systematic and premature failures of a particular type of XLPE cable terminations operating at 88 kV (rms). The utility therefore desired to understand the modes of failure in order to evaluate the risk with the terminations still in service. Failed terminations were forensically analysed. The dominant modes of degradation were identified as electro-thermal, galvanic corrosion and thermomechanic fatigue. Based on the weakest link principle, a reliability model was developed using the life factor models corresponding to the identified modes of degradation. Galvanic corrosion and thermomechanic fatigue life factors were found to have the predominant influence on the overall reliability of the termination as they reduced the cable termination life by more than 10 years. The model can be used to track the probability of the remaining life of the terminations as well as evaluating the effectiveness of alternative designs and/or in-situ repairs.

### **1. Introduction**

In the literature, there has been sustained research efforts in the development and application of power cable reliability assessment models [1-6]. In that regard, contributions by the likes of Mazzanti and Marzinotto [1] are notable. Some models take into account the synergistic nature of electro-thermal stresses. The present work modifies an existing reliability model in the literature by considering the additional modes of degradation in the cable terminations that were identified

through forensic analyses in the case study. The rest of this article is structured as follows: Firstly, an overview of the power system portion containing the terminations is presented. The detailed design structure of the termination is explained including the forensic evidence of the dominant degradation mechanisms. Using the weakest link principle, a reliability model of the termination that incorporates the degradation modes; electro-thermal, corrosion and thermomechanic fatigue stress factors is then developed and discussed. The sensitivity of the model is tested, and the model is used to evaluate the modified termination designs.

## 2 An overview of the 88 kV XLPE cable termination system

The power cables in the present study link up outdoor equipment (transformers and overhead lines) with the indoor switchgear equipment as schematically illustrated in Figure 1(a). Each phase has two parallel connected single core cables. Typical cable length in the link is in the order of 100 m. One of the important conclusions drawn out in the literature on power cable systems reliability modelling thus far is that reliability is inversely proportional to the increasing number of accessories as well as cable length [1]. In the present study with a relatively short cable length of 100 m, the reliability of the cable system is therefore assumed to be mainly dependant on that of the two cable terminations.

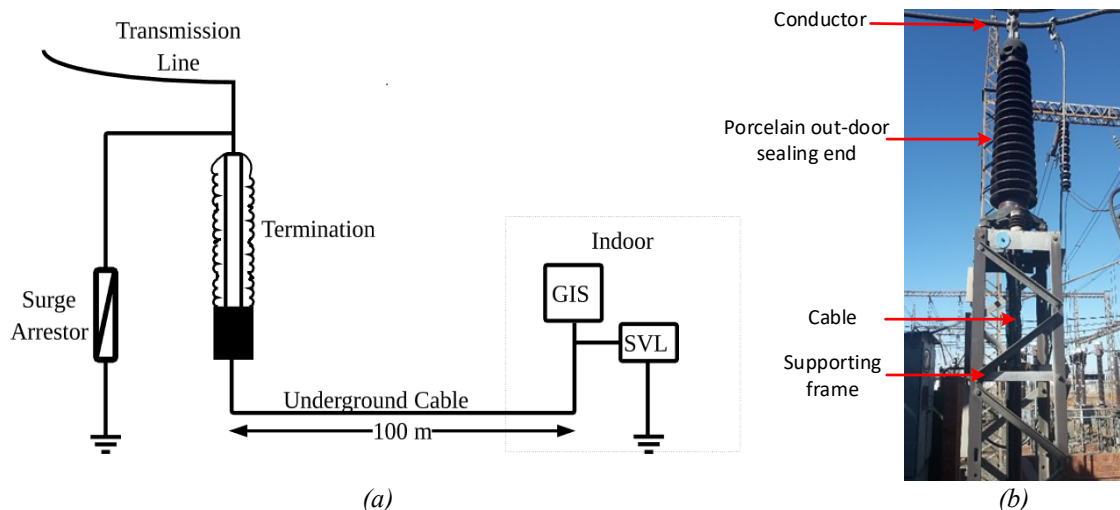


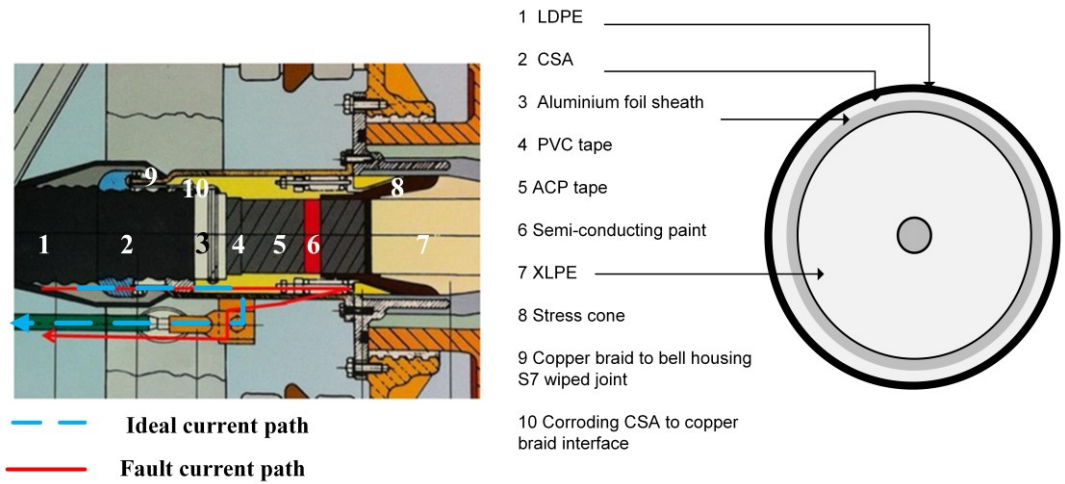
Figure 5. (a) Substation system where there are 88 kV XLPE cable terminations (b) An image of an 88 kV cable termination in the case study substation

The 88 kV cable termination on the outdoor end (as shown in Figure 1(b)) of the cable link is connected to a metal oxide surge arrester. The power cable is aluminium single core XLPE insulated and with a sheath made of corrugated seamless aluminium (CSA). The voltage rating is

76/132 kV but operated at a normal ac voltage of 50.8/88 kV. The indoor end of the cable terminates into an SF<sub>6</sub> gas insulated switchgear indoor board. The system is solidly bonded at the outdoor termination end. The indoor end is ungrounded but with a Sheath Voltage Limiter (SVL). It is important to note that due to the prevalent copper theft problems, there are system irregularities that have unfortunately become the norm and these include the missing ground connections on the outdoor surge arrester as well as the SVL. Such irregularities have a direct impact on the ageing stresses of the termination as is discussed later in this article. The substations are equipped with onsite 'black box' data measurement and acquisition system that uses Sapphire Elspec™ software to continuously log the millisecond power quality parameters such as power frequency current and voltage as well as transients [7].

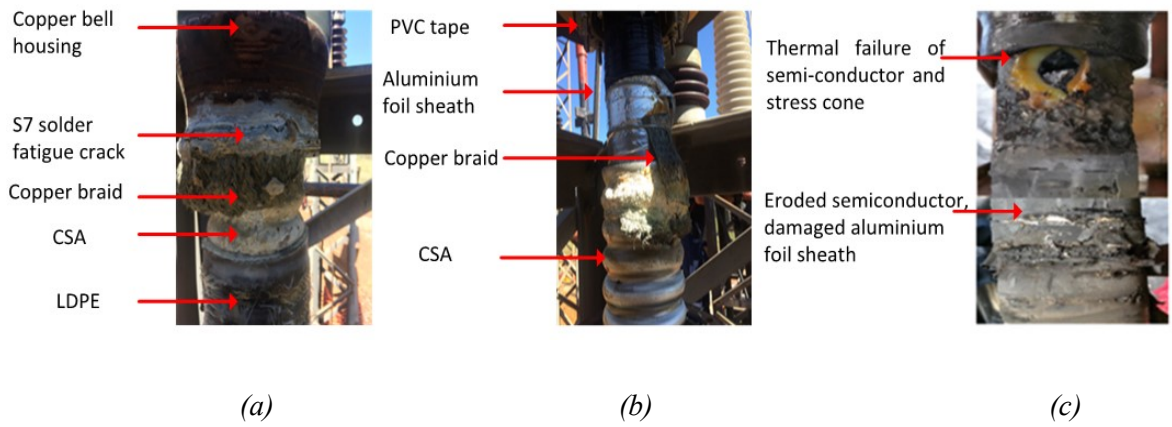
### **3 The termination structure and forensic evidence of the degradation modes**

After 29 years in operation with no significant problems, the cable terminations began failing prematurely and yet the expected service life was at least 40 years. Within less than a year, 9 terminations out of a random set of 12 terminations had failed and this caused major unusual blackouts. Forensic analyses of the failed terminations revealed the presence of three categories of degradations that caused the premature failure of the cable terminations [8]. The cable structure and termination details are illustrated in Figures 2(a) and (b) respectively. In the figure, sections 9 and 10 are subjected to thermomechanic fatigue and corrosion respectively. The failure of metal interfaces results in diversion of the fault current to undesired areas of the termination. In Figure 3, images of some typical evidence of failure degradations in the cable terminations are presented. In addition to the inherent electro-thermal degradation of the insulation, there is evidence of thermomechanic fatigue cracks and galvanic corrosion degradation of the metallic interfaces in the termination. With reference to the termination structure depicted in Figure 2(a), the soldered interface, comprising of S7 (35% tin 65% lead solder) between tinned copper braid and the copper bell housing makes up the path of the fault current to ground.



(a) Figure 2. Cross-sectional views of (a) the lower section of the termination and (b) the XLPE power cable.

This wiped metallic interface suffers mechanical fatigue fracture that is caused by the cyclic temperature changes within the plastic range of the solder resulting in cracks as can be seen in the image of the dissected failed termination in Figure 3(a). When the fatigue fracture crack occurs on the S7 solder, moisture ingress occurs that causes galvanic corrosion at the interface of tinned copper braid and the CSA as shown in Figure 3(b). Excessive degradation through fatigue and corrosion diverts the fault current path from the normal route (illustrated as a blue dashed line in Figure 2(a) as a blue dashed line) to an undesired path (indicated as red solid line). Consequently, the outer semiconducting layer is exposed to excessive thermo-electric stresses. The already electro-thermally aged insulation is eventually further degraded to complete failure of the termination with catastrophic effects. The above outlined degradation mechanism is not necessarily sequential as some processes can occur simultaneously and synergistically.



(b) Figure 3. (a) Fatigue fracture at Sn35Pb65 solder joint between copper braid and copper bell housing, (b) Galvanic corrosion of CSA and copper braid interface, (c) Electro-thermal degradation and erosion of semiconductor

The thermomechanic fatigue stress and the galvanic corrosion stress herein identified as part of the failure modes of the termination are used to expand the existing model by Mazzanti and Marzinotto [1] using the Weakest Link Principle as presented in the next sections.

#### 4 The reliability model formulation

The time-to-failure data of a randomly selected set of terminations were fitted into a Weibull distribution [9]. The data sample comprised of 12 terminations where 3 were still fully functional and 9 had failed. Due to the small sample size, the Whites method [9] was used to improve the error margin of the statistical analysis. In the present study, failure is defined as either when there is high partial discharge activity being a symptom of imminent failure or when the termination catastrophically failed. The Weibull distribution in accordance with the IEC 62539 standard [9] and computed using Equation 1 was used to fit the right censored data; data that includes failed and operational terminations at the time of data collection [9].

$$P_W(t) = 1 - \exp\left(-\left(\frac{t}{\alpha_0 \cdot \alpha}\right)^\beta\right) \quad (1)$$

Where  $P_W(t)$  is the probability of failure at any given time,  $\alpha$  is the degradation mechanism acceleration factor,  $\alpha_0$  is the statistical distribution scale parameter which represents the 63.2<sup>th</sup> percentile time of failure,  $\beta$  is the shape parameter which is the gradient of the distribution and  $t$  is time [9]. The shape and scale parameter values give an indication of the possible cause of failure. When the shape parameter is less than one, the terminations fail prematurely due to either manufacturing or installation flaws. A shape parameter equal to one shows failure due to random causes. A shape parameter greater than one depicts failure due to ageing [10]. In the present case study, the shape parameter is 5.01 and the scale parameter is 29.98 years. The shape parameter being greater than one confirms that the failure of the accessories is due to ageing. Assuming no manufacturing or installation flaws the reliability of the termination can be obtained from subtracting the probability of failure from 100 % reliability as shown in Equation 2. This reliability estimates the likelihood of the terminations still in operation to exceed the designed life (at the time the data was collected).

$$R(t) = 1 - P_W(t) \quad (2)$$

The overall reliability is then obtained by substituting the Weibull distribution function given in Equation 1 into Equation 2 as shown in Equation 3.

$$R(t) = 1 - \left[ 1 - \exp\left(-\left(\frac{t}{\alpha_0 \cdot \alpha}\right)^\beta\right) \right] \quad \text{or} \quad R(t) = \exp\left(-\left(\frac{t}{\alpha_0 \cdot \alpha}\right)^\beta\right) \quad (3)$$

Where  $R(t)$  is the reliability at any given time under the influence of a degradation mechanism characterised by the life factor,  $\alpha$ . In the case of the cable terminations under study, the forensically identified degradations comprise of three mechanisms; electrothermal, thermomechanic and galvanic corrosion. The resultant reliability model using the Weakest Link Principle (WLP) can therefore be presented in the form of Equation 4 [1], [10].

$$R_{E,T,N,C}(t) = R_E(t) \cdot R_T(t) \cdot R_N(t) \cdot R_C(t) \quad (4)$$

Where  $R_E$  and  $R_T$  are the reliabilities under the influence of electric and thermal stresses respectively,  $R_N$  is thermomechanic fatigue reliability and  $R_C$  is corrosion reliability. In the following sections the analytical reliability model for each degradation mechanism is formulated after which the overall reliability model of the termination is constructed.

## 5 The degradation stresses and corresponding life factors

### 5.1 Electric stress life factor, $\alpha(E, E_i)$

While in some electrothermal life models only the effect of the steady state electric stress is considered [11], Montanari et al [12] have included the effect of impulse stress and impulse count on the electric stress life of cable insulation. The resultant electric life due to both steady state and impulse stresses can be expressed using the Inverse Power Law [10] as shown in Equation 5.

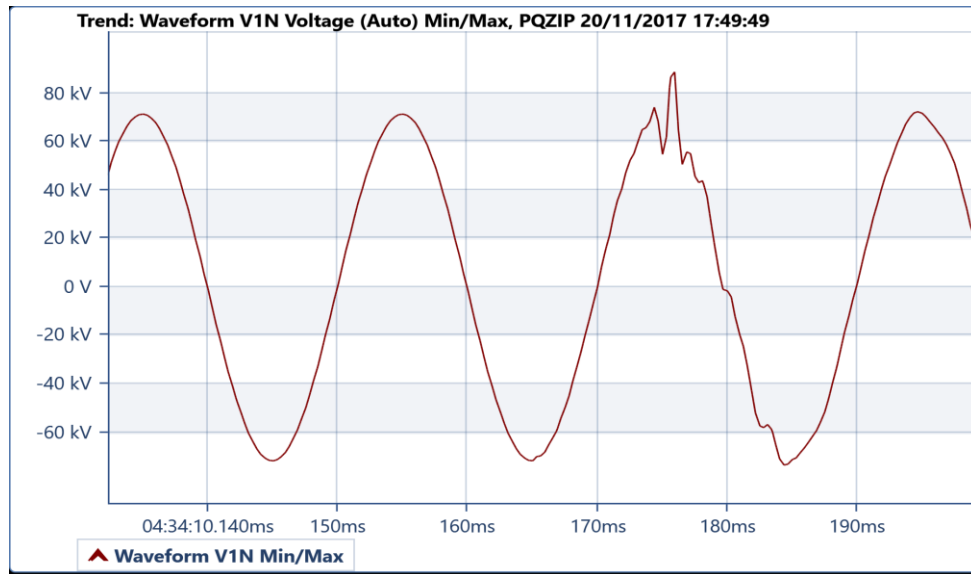
$$\alpha(E, E_i) = \left[ \left(\frac{E}{E_0}\right)^{-n} \cdot \left(\frac{E_i}{E_{i0}}\right)^{-n_i} \cdot \frac{f_0}{f_i} \right] \quad (5)$$

The symbols and corresponding values used in the case study electric life model are listed in Table 1. In the case at hand there was no evidence of lightning strikes, therefore the maximum impulse stress  $E_i$  used in Equation 5 is that associated with switching and fault current induced voltage surges. The switching surges include circuit breaker operations of the SF6 GIS (Gas Insulated Switchgear). Up to 56 switching surges per month were identified in the records. An example of a switching event is shown in Figure 4. The switching frequency of occurrence,  $f_i$ ,

translates to  $2.13 \times 10^{-5}$  Hz being the inverse of the time interval (seconds) between switching events. The switching occurrence frequency is very low in comparison to the steady state voltage frequency (50 Hz) resulting in a corresponding overall high electric field stress factor.

(c) Table 2. Electric stress model life parameters

Description	Symbol	Value
Maximum continuous stress (Obtained through FEMM simulations at maximum operating peak voltage)	$E$	5.35 kV/mm
Design stress (76/132 kV XLPE Al core CSA cable)	$E_o$	6.8 kV/mm
Maximum impulse stress (Switching impulse stress at maximum switching voltage as recorded by data logging system (See figure 4) *switching has been used because there were no direct lightning strikes observed in one year's operating data*)	$E_i$	6.85 kV/mm
BIL stress ( Derived from the BIL of 325 kV for 88 kV system [13],[14])	$E_{io}$	24.73 kV/mm
Impulse voltage endurance coefficient [1], [12]	$n_i$	7
Steady state voltage endurance coefficient [1], [12], [15]	$n$	10
Power frequency	$f_o$	50 Hz
Frequency of impulses (impulse count obtained from the data measurement system)	$f_i$	$2.13 \times 10^{-5}$ Hz
<b>Electric stress life factor (obtained using Equation 5)</b>	<b><math>\alpha(E,E_i)</math></b>	<b><math>2.23 \times 10^{11}</math></b>



(d) Figure 4. Switching transients recorded in the substation black box system (Sapphire Elspec™). Peak voltage = 90 kV

In one year's operating data the maximum recorded phase-to-ground fault current was 9 kA. The resultant sheath overvoltage as calculated using Equation 6 for the metallic sheath [16], is 15.6 kV.

$$E_{sh} = 107 \cdot \left(\frac{s}{d}\right)^{0.369} \cdot l_c \cdot I_c \quad (6)$$

Where  $E_{sh}$  is the maximum induced sheath voltage at the non-grounded end.  $S$  is the centre to-centre cable spacing of 36.12 cm,  $d$  is the mean sheath diameter 98 mm,  $l_c$  is the cable length of 100 m and  $I_c$  is the conductor current. When the SVL (sheath voltage limiter) at the GIS side of the cable is faulty there is a higher induced sheath voltage at the termination end. Furthermore, when the metallic interfaces in the cable termination fail due to corrosion or thermal-mechanic fatigue, the fault current path to ground is disrupted. The compromised ground connection on the cable termination together with a non-grounded station surge arrester and SVL (due to cable theft) result in a relatively high sheath voltage of up to 15.6 kV under fault current conditions instead of the maximum allowable value of 6-7 kV [12].

## 5.2 Thermal stress degradation life factor, $\alpha(t, T)$

In the present case study, the material with the least thermal strength in the termination is the XLPE insulation [14]. The rate of thermal degradation of the termination depends on the maximum temperature, the temperature duration as well as the activation energy that is required to initiate thermal degradation in XLPE insulation. Cyclic load profiles, fluctuating ambient temperatures and the thermal capacities of interfacing materials affect the overall temperature changes in the termination [18]. The thermal stress life is modelled using the Arrhenius law [19]. The summation of life fractions lost at each temperature step are modelled using Miners rule [10]. The combination of Miner and Arrhenius laws give an estimate of thermal stress life as shown in Equation 7. The parameters used in Equation 7 for the termination in the case study are defined in Table 2.

$$\alpha(t, T_i) = \sum_{i=1}^N \left\{ \int_0^{\Delta t_i} \frac{dt}{\exp\left[\left(\frac{\Delta W}{k_B}\right) \cdot (1/T_o - 1/T_i)\right]} \right\} \quad (7)$$

(e) Table 3. Thermal life model parameters for the case under study

Description	Symbol	Value
XLPE thermal degradation activation energy [1] (Obtained from the termination ratio of activation energy to Boltzmann constant of 12937 by Mazzanti et al [1])	$\Delta W$	$1.7034 \times 10^{-19} \text{ J}$
Boltzmann's constant	$k_B$	$1.381 \times 10^{-23} \text{ J.K}^{-1}$
Maximum operating temperature	$T_o$	93.53 °C
Step operating temperatures	$T_i$	*See figure 5
Temperature steps (Hourly)	$N$	24
Hourly average winter temperatures in degrees Celsius	$T_{Ei}$	8,7,7,6,6,5,5,6,8,11,12,13,14,15,14,14,13,12,9,9,8,8,9,8
<b>Thermal stress life factor (Calculated using Equation 7)</b>	<b><math>\alpha(t, T_i)</math></b>	<b>3.71</b>

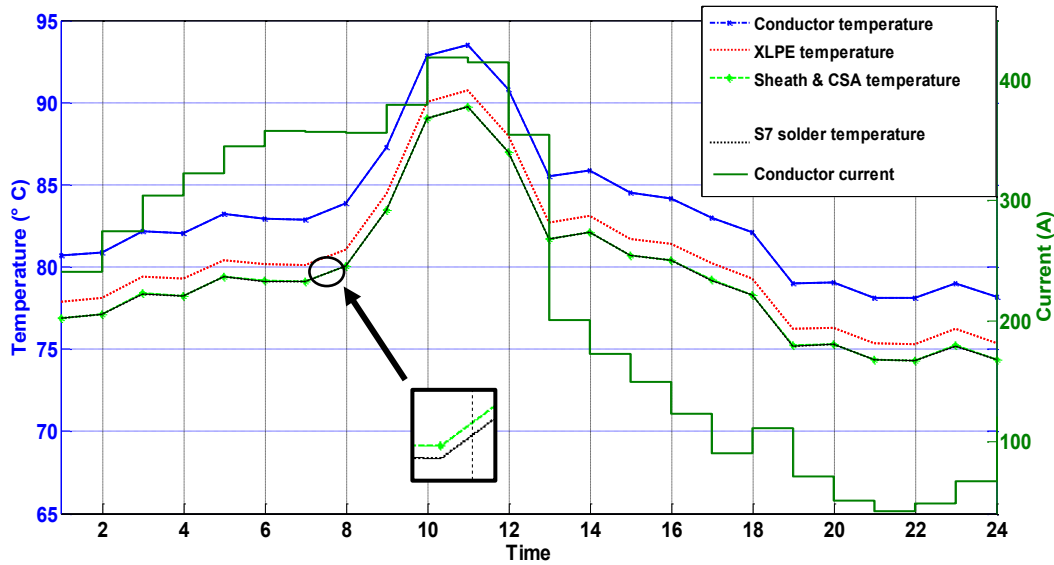
In the case study, the highest load current was recorded during the winter seasons. A typical winter day hourly current step profile obtained from the data measurement system combined with the hourly winter external temperatures are used to calculate the transient temperatures in the critical layers of the cable termination. Using the IEC 60853-2 standard [17] and the Cigré two loop network [20], the transient temperature changes of the conductor corresponding to each step current are calculated using Equation 8.

$$T_{ci} = W_d [T_a(1 - e^{-at}) + T_b(1 - e^{-bt})] + \frac{T_a(1 - e^{-at}) + T_b(1 - e^{-bt})}{T_a + T_b} \cdot T_{Ei} \quad (8)$$

Where  $T_{ci}$  is the conductor temperature change above the surface temperature of the cable due to each current step change.  $W_d$  is the heat losses,  $T_a$  and  $T_b$  are the thermal resistances of the cable,  $a$  and  $b$  are the time constants of the first and second thermal network respectively and  $T_{Ei}$  is the hourly environmental daily average temperature during the winter season. Assuming one directional heat flow, isotropic heat flow and a constant thermal conductivity for each material in the termination, the transient temperature changes in the XLPE insulation and subsequent layers of the cable were computed using the Fourier heat equation [21] shown in Equation 9. The thermal conductance, thickness as well as the distance away from the conductor heat source determines the temperature changes of each layer.

$$T_{n(i+1)} = T_{ni} + \frac{I^2 R \cdot \ln\left(\frac{r_{n(i+1)}}{r_i}\right)}{-K_i \cdot 2\pi L} \quad (9)$$

Where  $T_{n(i+1)}$  is the temperature change of layer  $n(i+1)^{th}$  due to the temperature change  $T_{ni}$ , at the  $i^{th}$  layer,  $I$  is the cyclic load current,  $R$  is the conductor resistance,  $K_i$  is the thermal conductance,  $L$  is the cable length,  $r_{i+1}$  and  $r_i$  are the thicknesses of the interfacing layers. Operating load profiles over a year obtained from the substation data measurement system show that the worst load cycle profile occurs in winter. Using Equation 8 and 9 the calculated changes in the main layers of the cable due to cyclic current on a typical winter day are plotted in Figure 5.



(f) Figure 5. Temperature changes with worst case load current profile trend.

### 5.3 Steady State Electrothermal Reliability, $R(E,T)$

An alternating electric field causes dipole relaxation within the insulation and this results in gradual expansions of the air pockets within the insulation thereby degrading the insulation. At a critical electric field stress when the heat generated by dipole relaxation exceeds the heat dissipated from the insulation, there is permanent damage [9]. Due to a synergistic relationship between electric and thermal degradation the effect of the two failure modes can be combined. For comparison with similar results in the literature such as that by Mazzanti et al [1], the electrothermal life factor without the impulse stress component at the recorded maximum peak steady state voltage stress of 5.35 kV/mm is calculated as  $\alpha(E, T) = 40.82$ , being the product of steady state electric stress life factor with the thermal life factor. The thermo-electric life factor decreases with increase in steady state stress factor as shown in the resultant plots of

electrothermal reliabilities presented in Figure 6(a). The plots compare reasonably well with those in Figure 6(b) from similar work by Mazzanti et al [1].

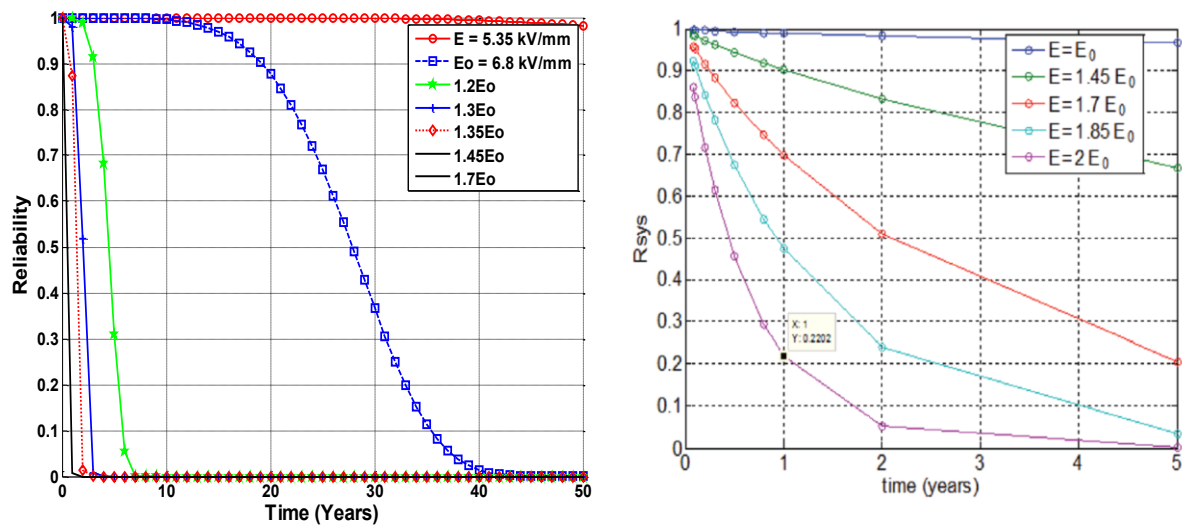


Figure 6. (a) Steady state electrothermal reliability of case study cable terminations at XLPE temperature (min  $\approx 75$  °C, max  $\approx 91$  °C). (b) Existing electrothermal reliability ( $R_{sys}$ ) model for an HVDC 150 m cable system without joints,  $E_0 = 16.5$  kV/mm

The two models depict comparable trends showing reduced reliabilities with time at higher electric field stresses. The specific values are however different since the rate of life lost is a function of site and system specific conditions as manifested in the specific Weibull shape and scale parameters. In the present case study, at a steady state operating electric field stress of 5.35 kV/mm and in the absence of switching and lightning surges, the electric stress factor is 11.0 which gives an electrothermal reliability of above 90% after 29 years and that would not be a cause for concern. This shows that electrothermal degradation on its own is not the dominant degradation stress within the termination and there are no installation or manufacturing defects. The model also shows that if maximum continuous electric field stress is increased beyond the design stress of 6.8 kV/mm, the lifespan reduces to below 40 years. Switching and lightning impulses are therefore expected to lower the reliability substantially in the absence of a grounded station surge arrester and SVL.

In the present study a switching frequency of occurrence of  $2.13 \times 10^{-5}$  Hz in the absence of a station surge arrester or SVL produced comparable results to those obtained under steady state conditions. However, in GIS substations, VFT (Very Fast Transients) that are caused by the switchgear operations introduce high resultant stress conditions especially due to the travelling

wave voltage reflection phenomena [22]. Assuming the VFT frequency of occurrence of  $2.13 \times 10^{-5}$  Hz, the termination reliability would drop to 50 % after 29 years in operation if the corresponding VFT induced stress in the termination reaches 105.5 kV/mm as shown in Figure 7.

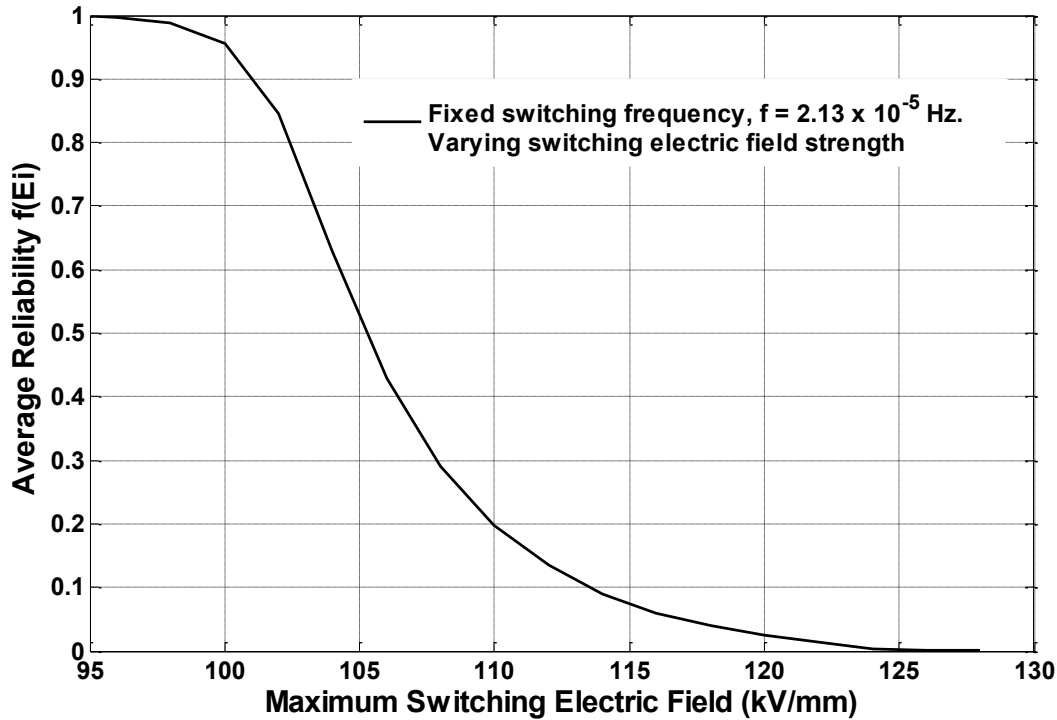


Figure 7. Effect of varying switching electric field strength and impulse count on reliability for terminations in the case study substation after 29 years in operation.

#### 5.4 Thermomechanic fatigue life factor, $\alpha(N)$

Forensic evidence shows the presence of thermomechanic fatigue induced cracking on the S7 wiped interface of the tin-plated copper braid and the copper bell housing [7]. Fatigue fracture occurs in the presence of plastic strain, cyclic and tensile stress. Cyclic load cycle temperature range and frequency affect the rate of fatigue fracture growth. Equation 10 presents the fatigue stress life acceleration factor evaluated using Landzberg and Norris model [23] that is based on Arrhenius and Coffin-Manson laws [10]. The resultant thermomechanic fatigue stress life factor is presented in Table 3 as well as the various symbols and assigned values.

$$\alpha(N) = \left(\frac{f_T}{f_{T0}}\right)^{-a} \cdot \left(\frac{\Delta T}{\Delta T_0}\right)^{-b} \cdot \exp\left(\frac{A_E}{k_B} \cdot (1/T_{max} - 1/T_{T0})\right) \quad (10)$$

Table 4. Thermomechanic parameters

Description	Symbol	Value
Design thermal cycle frequency (Based on the assumption that there are two thermal cycles per day)	$f_{T0}$	$2.314 \times 10^{-5}$ Hz
Thermal cycle frequency (Obtained from the thermal cycle frequency of Figure 5)	$f_T$	$1.157 \times 10^{-5}$ Hz
Solder operating temperature range (Obtained from Figure 5)	$\Delta T$	11.53 °C
S7 (35/65, Sn/Pb) temperature range [24]	$\Delta T_o$	223 °C
Temperature steps in a 24-hour day	$N$	24
S7 material constant [24], [25]	$a$	1/3
S7 material constant [24], [25]	$b$	1.9
S7 activation energy to reach fracture [25]	$A_E$	0.12 eV
Boltzmann constant	$k_B$	$8.617 \times 10^{-5}$ eV/K
Design maximum temperature [25] (Melting point of Sn35Pb65 solder)	$T_{T0}$	183 °C
S7 maximum operating temperature (Obtained from Figure 5)	$T_{max}$	89 °C
<b>Thermomechanic fatigue stress life factor (Calculated using equation 10)</b>	<b><math>\alpha(N)</math></b>	<b>0.492</b>

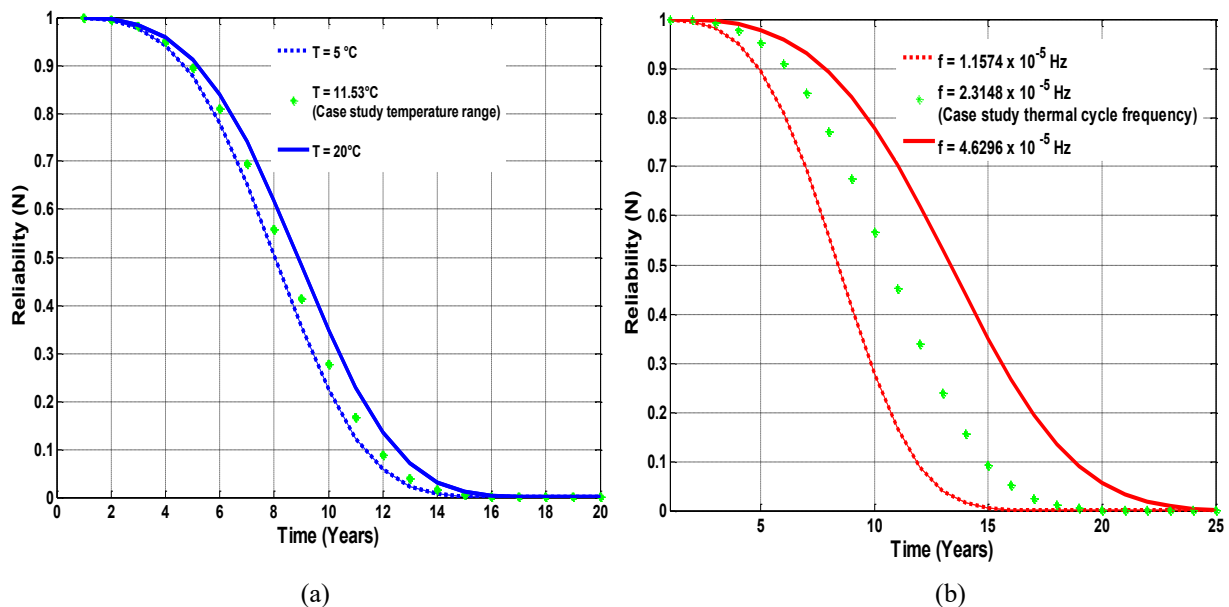
The ratio of the operating temperature range,  $\Delta T$ , to the maximum design temperature range,  $\Delta T_o$ , as well as the ratio of design thermal frequency,  $f_{T0}$ , to operating thermal frequency,  $f_T$ , are critical in fatigue fracture. The design thermal cycle frequency is assumed to be at least 2 cycles per day for a 40-year life span. This assumption is taken from the winter load cycle trends where peak power consumption occurs twice a day during the morning and evenings.

### 5.5 Thermomechanic fatigue reliability, $R(N)$

The comparative sensitivity of the S7 solder reliability to changes in the thermal cycle frequency and temperature range are shown in Figure 8. By holding the thermal cycle frequency constant at  $1.157 \times 10^{-5}$  Hz and varying the temperature range from 5 °C to 20 °C, Figure 8(a) shows that the reliability changes marginally. If, however the temperature is held constant at 11.53 °C and cycle frequencies varied from  $f = 1.157 \times 10^{-5}$  Hz to  $f = 4.629 \times 10^{-5}$  Hz, the changes in reliability are relatively more significant as shown in Figure 8(b). The model therefore shows that the S7 solder reliability is more sensitive to thermal cycle frequency in comparison to changes in temperature range. However, the thermomechanic fatigue model underestimates the rate of crack formation and growth in the S7 solder because it does not take into account the effect of rate of temperature variation (ramp time) and the durations (dwell time) of the maximum and minimum temperature [24]. Ramp and dwell time can introduce creep simultaneously with fracture. The effects of creep are indirectly observed from the trend shown in Figure 8, where an increase in thermal cycle frequency and temperature range gives

a lower likelihood of failure with time and this is because at lower frequencies the termination may be exposed to high temperatures for a longer period which causes more synergy between creep and fatigue.

The effect of IMC (Intermetallic Compound Growth) has been omitted in the present analysis as it is only prevalent at non-cyclic temperatures above 150° C [26]. It is evident that in the design of the termination, the thermal cycling strengths of materials used may not have been considered. Thermal tests on cables are usually concerned with the primary components of the cable, while the secondary materials added on during accessories installation such as solders, PVC and ACP tape may need to be adequately tested to ensure full functionality under operating conditions. Such an anomaly needs to be corrected in modern designs.



(g) Figure 8. Thermomechanical fatigue at (a)  $f = 1.157 \times 10^{-5}$  Hz (1 cycle per day) and different temperature range.  
 (b)  $\Delta T = 11.53$  °C and different thermal cycles

### 5.6 Galvanic corrosion life factor, $\alpha(C)$

When overlaying materials are weakened by thermal expansion and contraction, fissures develop through which moisture ingress may occur. In the terminations under study, the funnel shape of the copper bell housing together with the gradual roll-back of the protective materials create conducive conditions for channelling water flow through fissures into the cable termination. The electron affinity difference between the tinned copper braid and CSA interface in the presence of moisture results in galvanic corrosion [27]. Pourbaix’s theory on

the thermodynamics of corrosion states that an optimum hydrogen concentration and voltage facilitate corrosion [28]. A combination of Pecks and Arrhenius laws can be used to model the corrosion stress life in the form of Equation 11. The symbols and assigned values are presented in Table 4 together with the calculated corrosion stress life factor.

$$\alpha(C) = \left(\frac{RH}{RH_0}\right)^{-M} \cdot \exp\left\{\frac{A_c}{k_B}(1/T_{CO} - 1/T_{max})\right\} \quad (11)$$

(h) Table 5. Corrosion model parameters

Description	Symbol	Value
Maximum annual site humidity (Site average annual humidity)	$RH$	59 %
Critical threshold humidity	$RH_0$	40 %
Corrosion metal constant from Feinberg et al[27]	$M$	2.66
Aluminium galvanic corrosion energy [7], [29]	$A_c$	0.8 eV
Boltzmann constant	$k_B$	8.617 x 10 <sup>-5</sup> eV/K
Design maximum operating temperature	$T_{CO}$	90°C
Maximum temperature, Aluminium and Copper interface (From Figure 5)	$T_{max}$	89 °C
<b>Corrosion stress life factor (Computed in Equation 11) Feinberg et al [27]</b>	$\alpha(C)$	<b>0.67</b>

The activation energy of corrosion, also known as Gibbs free energy, is a function of the applied voltage, Faradays constant and the available number of electrons in the electrochemical cell [27]. When the free energy is negative, corrosion occurs spontaneously and when it is positive the process occurs provided there is a sufficient temperature increase in the galvanic cell. The galvanic action results in the significant increase of the resistance of the aluminium sheath and CSA in comparison to that of copper [30]. Alternating voltage and current at the sheath surface results in intermittent corrosion, where in either the positive or negative half cycle (depending on the galvanic cell polarity) corrosion is aided or hindered.

The complex thermodynamic nature of corrosion is a non-continues process where the galvanic cell changes with alternating sheath voltage and changing ionic concentration. The process is therefore alternately active and inactive, however, its by-products drastically increase the contact resistance between the CSA and tinned copper braid and gradually destroys the critical fault current path [30]. The physical position of the metals (aluminium and copper) relative to each other is important. If copper (cathode) is placed above the aluminium (anode) and the water flows down from the copper to the aluminium, it will result in weak copper salts dropping onto the aluminium, thus drastically reducing the aluminium with time. If the aluminium is placed above the copper then the corrosion rate is much slower, as the natural flow of water opposes that of the electrical connection between copper and aluminium. The electrolytic

concentration is not known and may vary with time, therefore there will be a varying activation energy of corrosion. In the presence of acidic or chloride ions the activation energy is much reduced [31]. The optimum humidity for corrosion to occur also varies with temperature and electrolyte concentration. It is therefore difficult to evaluate the sensitivity or optimism of the corrosion model.

In the present work model, only galvanic action is considered, however it is likely that other forms of corrosion are present such as pitting and crevice corrosion [32]. Galvanic action is only considered as there are two metals with different affinities in contact and forensic evidence shows the presence of galvanic action by-products.

### 5.7 Corrosion reliability, $R(C)$

The effect of humidity and the corrosion activation energy on reliability under corrosion is depicted in Figure 9. The activation energy of corrosion is a function of the potential difference between the interfacing materials, Faraday's constant and the number of free electrons in the cell [27]. Figure 9 shows that humidity has a greater effect on the rate of galvanic corrosion in comparison to the activation energy. From Figure 9, in order for the termination to withstand corrosion beyond its design lifespan, not more than 20% humidity should reach the copper braid and CSA interface.

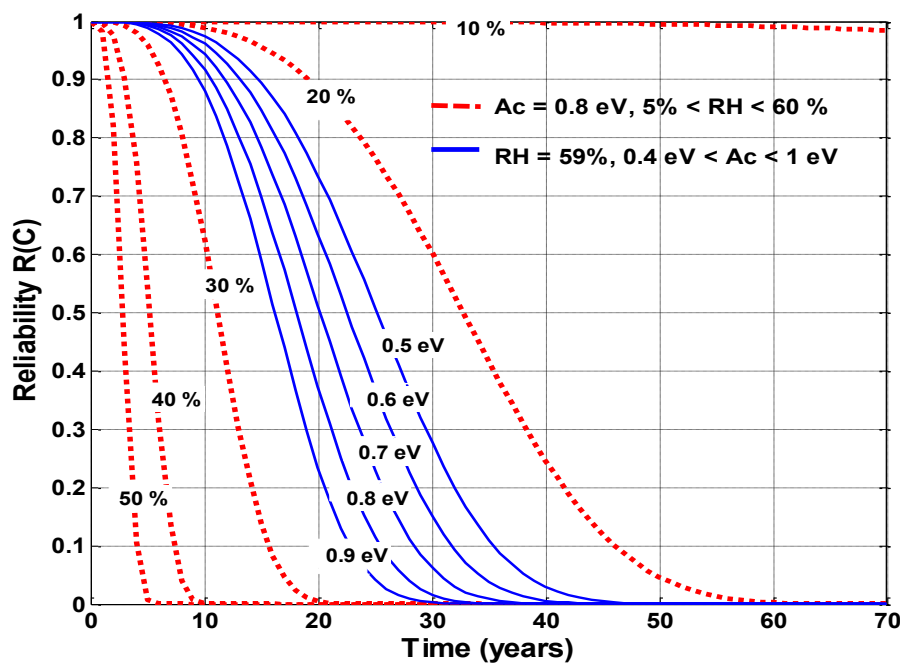


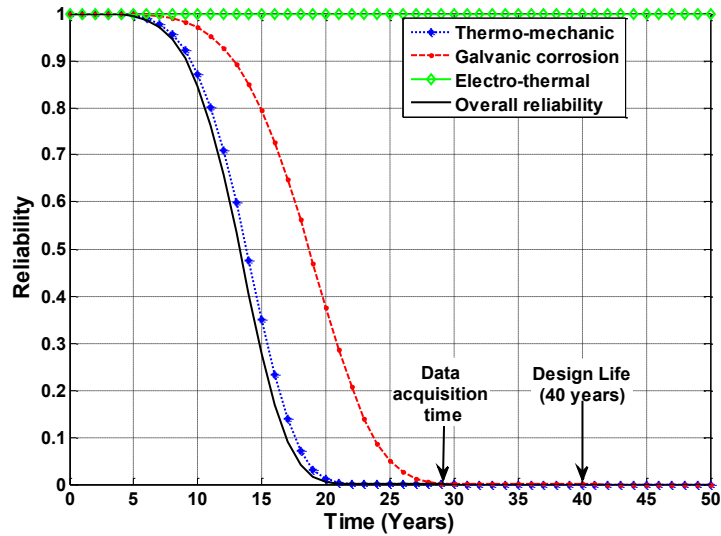
Figure 9. Effect of corrosion humidity and activation energy on reliability

## 6 Overall reliability

In the preceding sections, the reliability models as a function of individual degradation stresses have been presented. The sensitivities of each model to changes in the influencing parameters were evaluated. For a system made up of various components such as a cable termination, each with its own life model, the overall reliability of the termination system is the product of reliabilities due to each degradation mechanism. This ensures that the most prevalent degradation mechanism determines the overall reliability of the system. Mazzanti and Marzinotto [1] developed an electrothermal reliability model for a power cable system where the overall reliability is a product of reliabilities of each component in the system in accordance with the Weakest Link Principle [1]. In the present work the same principle is adopted where the overall reliability is obtained by substituting the acceleration factor of each degradation mechanism as shown in Equation 12 [10].

$$R_{E,T,N,C}(t) = \exp\left[-\left(\frac{t}{\alpha_0 \cdot \alpha_E}\right)^\beta\right] \cdot \exp\left[-\left(\frac{t}{\alpha_0 \cdot \alpha_T}\right)^\beta\right] \cdot \exp\left[-\left(\frac{t}{\alpha_0 \cdot \alpha_N}\right)^\beta\right] \cdot \exp\left[-\left(\frac{t}{\alpha_0 \cdot \alpha_C}\right)^\beta\right] \quad (12)$$

Where  $\alpha_E$  is the Electric stress life factor,  $\alpha_T$  is the Thermal stress life factor,  $\alpha_N$  is the Thermomechanical life factor and  $\alpha_C$  is the corrosion life factor. A plot of Equation 12 is presented in Figure 10 and is the overall reliability of the termination at the time of the study. In the same Figure 10, plots of individual reliabilities corresponding to electrothermal, thermomechanical and galvanic life factors are shown. Due to the synergistic nature of electric and thermal degradation the product of electric and thermal reliabilities (electro-thermal reliability) are combined and illustrated in Figure 10. The results indicate that electrothermal stress hardly reduces the reliability of the termination from the time of installation to 40 years in service. However, thermomechanical stress causes a reliability of less than 10% after 18 years and galvanic degradation reduces the termination reliability to less than 10% after 24 years in operation. The percentage reliabilities as a function of each degradation mode are summarized in Table 5.



(i) Figure 10. Reliability under thermomechanic, electrothermal, galvanic corrosion and overall reliability for case study substation

Thermomechanic fatigue and corrosion are therefore the predominant modes of failure. Corrosion increases the resistance of the fault current path while fatigue fracture disconnects the fault current path. When the fault current flows through an alternative path across the semiconductor towards the stress cone, it further enhances the electrothermal stresses. Consequently, as shown in Figure 10, the overall life of the cable system is reduced to below 30 years as galvanic corrosion and thermomechanic stress become the life determining factors. The use of maximum stress magnitudes in the model and omission of stress durations provides a balanced sensitivity. Some stresses occur alternately while others, such as corrosion, are complex and change with the pH levels and voltages resulting in the reversal of electron flow between the copper braid and CSA.

(j) Table 6. Percentage reliabilities as a function of service time under each degradation mechanism

Service time (years)	10	20	30	40
Electro-thermal reliability: $R(T, E)$	100	100	100	100
Thermal mechanic reliability: $R(N)$	87.13	1.16	0	0
Corrosion reliability: $R(C)$	97.02	37.60	0	0

## 7 Reliability evaluation of the improved termination design

The cable terminations in the case study substation have metallic interfaces that are exposed to prevalent thermomechanic fatigue and corrosion. Elimination of galvanic corrosion by ensuring a watertight termination and using low or lead-free solder may improve the reliability

of the metallic interfaces. If a Sn60Pb40 solder is used there will be a minor improvement in reliability as shown in Figure 11 below. However, when water is restricted from entering the cable termination, the corrosion reliability is significantly improved with a higher probability of the cable termination being able to exceed the design life. Design modifications that make the cable termination to be more water-proof have higher impact on the extension of the cable termination reliability.

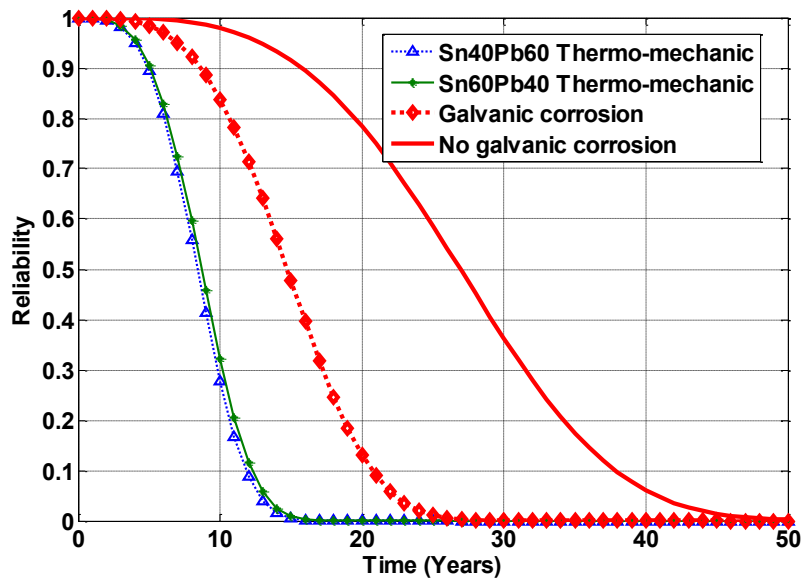


Figure 11. Effect of Sn60Pb40 solder and absence of galvanic corrosion on reliability of the termination

The results obtained in this case study give a projection on the likelihood of the terminations reaching their design life when evaluated after 29 years in operation. The trends shown are subject to change with time as 3 terminations in the case study were still operational and their time of failure would change the scale and shape parameters of the Weibull distribution, thus giving a different reliability projection with time. This model is therefore valid for specific designs where possible degradation mechanisms are known. For newly formulated termination designs, laboratory accelerated aging test results are necessary to provide the preliminary parameters that can be combined with online monitoring systems data to obtain a real-time computation of the cable accessory reliability with time.

## 8 Conclusion

Power cable terminations are designed to live for a minimum specific life period. The terminations however may fail before the expected end of life either because of installation faults or premature ageing. This work has shown that the reliability of a complex structure such

as a cable termination is a function of reliabilities of the individual components in the structure. Where there are metal interfaces in the termination, corrosion and thermomechanic life factors become the weakest link in the reliability model.

In order to determine the reliabilities of newly formulated termination designs it is therefore necessary to consider laboratory based accelerated life tests from which reliability model parameters can be deduced. The latter can then be combined with online monitoring data to obtain a real time computation of the cable accessory reliability. The accuracy limitations of the model are in some of the model parameters that are not always precisely fixed. The procedure for the life modelling can be summarised as follows;

- Identify the population of the terminations of similar designs and installed during the same period.
- At a chosen time during the life period of the terminations, take a record of the time of failure of terminations and the number of healthy terminations. Compute the Weibull distribution analysis of the data to determine the corresponding shape and scale parameters.
- Determine the reliability (the probability that the termination will live up to the design life) as a function of each degradation mechanism life factor. Each life factor is modelled as an analytical expression being a function of the various factors that influence the specific degradation processes.
- The overall reliability at any given time, is a product of all the constituent reliabilities.

## **Acknowledgement**

The authors would like to express gratitude to Mr Patrick O'Halloran for access to the data used in this study and also useful technical insights. Givemore Chitungo is also thanked for technical support on the provision lightning data. Furthermore, the authors would like to thank Hylton Dettmer for his assistance with the PQSCADA Sapphire Elspec™ software.

## References

- [1] G. Mazzanti and M. Marzinotto, 'Advanced Electro-Thermal Life and Reliability Model for High Voltage Cable Systems Including Accessories', *DEIS*, vol. 33, no. 3, pp. 17–25, May/June.
- [2] M. Marzinotto and G. Mazzanti, 'Merging the electro-thermal life model for power cables with the statistical volume enlargement law', in *2014 IEEE Conference on Electrical Insulation and Dielectric Phenomena (CEIDP)*, 2014, pp. 502–505.
- [3] G. C. Montanari, G. Mazzanti, and L. Simoni, 'Progress in electro-thermal life modelling of electrical insulation during the last decades', *IEEE Trans. Dielectr. Electr. Insul.*, vol. 9, no. 5, pp. 730–745, Oct. 2002.
- [4] G. Mazzanti, 'The combination of electro-thermal stress, load cycling and thermal transients and its effects on the life of high voltage ac cables', *IEEE Trans. Dielectr. Electr. Insul.*, vol. 16, no. 4, pp. 1168–1179, Aug. 2009.
- [5] M. Cacciari, G. C. Montanari, L. Simoni, A. Cavallini, and A. Motori, 'Long-term electrical performance and life model fitting of XLPE and EPR insulated cables', in *Proceedings of the 1991 IEEE Power Engineering Society Transmission and Distribution Conference*, 1991, pp. 135–142.
- [6] G. C. Montanari, G. Pattini, and L. Simoni, 'Long - Term Behaviour of XLPE Insulated Cable Models', *IEEE Trans. Power Deliv.*, vol. 2, no. 3, pp. 596–602, Jul. 1987.
- [7] Elspec, 'Multi-Vendor Power Quality Management software.', *Elspec*, 26-Apr-2016. .
- [8] P. O'Holloran, 'Site Visit, In Conversation', 2017.
- [9] IEC62539, 'Guide for the statistical analysis of electrical insulation breakdown data', IEEE, 2007.
- [10] W. Nelson, *Accelerated Testing Statistical Models, Test Plans and Data Analysis*. New Jersey: John Wiley & Sons, 1990.
- [11] G. Mazzanti, 'Analysis of the Combined Effects of Load Cycling, Thermal Transients, and Electro-thermal Stress on Life Expectancy of High-Voltage AC Cables', *IEEE Trans. Power Deliv.*, vol. 22, no. 4, pp. 2000–2009, Oct. 2007.
- [12] G. C. Montanari, D. Fabiani, and F. Ciani, 'Partial discharge and aging of AC cable systems under repetitive voltage transient supply', in *2016 IEEE Electrical Insulation Conference (EIC)*, 2016, pp. 379–382.
- [13] IEC 60071-2, 'Insulation Co-ordination Application Guide', IEC, IEC 60071-2:1996, Dec. 1996.
- [14] E. Kuffel, W. Zaengl, and J. Kuffel, *High Voltage Engineering Fundamentals*, 2nd ed. Butterworth-Heinemann, 2000.

- [15] CIGRE, ‘Recommendations for Testing DC Extruded Cable Systems for Power Transmission at a Rated Voltage up to 500 kV’. Brochure CIGRE 496, Apr-2012.
- [16] ‘IEEE Guide for Bonding Shields and Sheaths of Single-Conductor Power Cables Rated 5 kV through 500 kV’, *IEEE Std 575-2014 Revis. IEEE Std 575-1988*, pp. 1–83, Sep. 2014.
- [17] IEC standard 60853-3, ‘Calculation of the cyclic and emergency current rating of cables - Part 3: Cyclic rating factor for cables of all voltages, with partial drying of the soil’, IEC, Feb. 2002.
- [18] Z. Zhang, P. Dieu Seul Assala, and L. Wu, ‘Residual life assessment of 110 kV XLPE cable’, *Electr. Power Syst. Res.*, vol. 7796, no. 0378, p. 9, 2018.
- [19] D. Kececioglu and J. A. Jacks, ‘The Arrhenius, Eyring, inverse power law and combination models in accelerated life testing’, *Reliab. Eng.*, vol. 8, no. 1, pp. 1–9, Jan. 1984.
- [20] S. B. Liu, ‘Calculation of the Steady-State and Transient Temperature Rises of Round Cable Bundles’, *IEEE Trans. Power Deliv.*, vol. 25, no. 3, pp. 1229–1235, Jul. 2010.
- [21] J. Coulson, J. Richardson, and J. Backhurst, *Fluid Flow Heat Transfer and Mass Transfer*, 6th ed., vol. 1. 1999.
- [22] M. Stosur, M. Szewczyk, W. Piasecki, M. Florkowski, and M. Fulczyk, ‘GIS disconnector switching operation #x2014; VFTO study’, in *2010 Modern Electric Power Systems*, 2010, pp. 1–5.
- [23] K. C. Norris and A. H. Landzberg, ‘Reliability of Controlled Collapse Interconnections’, *IBM J. Res. Dev.*, vol. 13, no. 3, pp. 266–271, May 1969.
- [24] H. Cui, ‘Accelerated Temperature Cycle Test and Coffin-Manson Model for Electronic Packaging’, in *Annual Reliability and Maintainability Symposium, 2005. Proceedings, 2005*, pp. 556–560.
- [25] C. Basaran and J. Jiang, ‘Measuring intrinsic elastic modulus of Pb/Sn solder alloys’, *Elsevier*, vol. 34, pp. 349–362, Apr. 2002.
- [26] J. Pang, K. Prakash, and T. Low, ‘Isothermal and Thermal Cycling Aging on IMC Growth rate in Pb-free and Pb-based Solder interfaces’, presented at the Inter Society Conference on Thermal Phenomena, 2004.
- [27] A. Feinberg and A. Widom, ‘On thermodynamic reliability engineering’, *IEEE Trans. Reliab.*, vol. 49, no. 2, pp. 136–146, Jun. 2000.
- [28] R. Baboian and S. Begum, ‘Corrosion, Galvanic’, in *Reference Module in Materials Science and Materials Engineering*, Elsevier, 2016.
- [29] J. Skrovan, ‘Activation Energy for the Corrosion of Aluminum Powders in Water’, *ECS Trans.*, vol. 41, no. 25, pp. 143–154, May 2012.

- [30] A. van Deursen, B. Kruizinga, P. Wouters, and E. Steennis, 'Impact of corrosion on the reliability of low voltage cables with aluminium conductors', presented at the UPEC Universities Power Engineering Conference, 2017, vol. 52.
- [31] H. B. Peacock, R. L. Sindelar, and P. S. Lam, 'Temperature and humidity effects on the corrosion of aluminium-base reactor fuel cladding materials during dry storage', 2004.
- [32] 'A Study of Corrosion Factors and the Electrochemical Theory', *Ind. Eng. Chem.*, vol. 17, no. 4, pp. 339–346, Apr. 1925.